
PHOTOVOLTAIC ARRAY SPACE POWER PLUS DIAGNOSTICS (PASP Plus) EXPERIMENT

D. A. Guidice, V. A. Davis, H. B. Curtis,
D. C. Ferguson, D. E. Hastings, F. L. Knight,
D. C. Marvin, K. P. Ray, P. S. Severance,
J. D. Soldi, M. Van Riet

March 1997

Final Report

19971202 017

APPROVED FOR PUBLIC RELEASE; DISTRIBUTION IS UNLIMITED.



PHILLIPS LABORATORY
Space Technology Directorate
AIR FORCE MATERIEL COMMAND
KIRTLAND AIR FORCE BASE, NM 87117-5776

DTIC QUALITY INSPECTED 3

PL-TR-97-1013

Using Government drawings, specifications, or other data included in this document for any purpose other than Government procurement does not in any way obligate the U.S. Government. The fact that the Government formulated or supplied the drawings, specifications, or other data, does not license the holder or any other person or corporation; or convey any rights or permission to manufacture, use, or sell any patented invention that may relate to them.

This report has been reviewed by the Public Affairs Office and is releasable to the National Technical Information Service (NTIS). At NTIS, it will be available to the general public, including foreign nationals.

If you change your address, wish to be removed from this mailing list, or your organization no longer employs the addressee, please notify PL/VTV, 3550 Aberdeen Ave SE, Kirtland AFB, NM 87117-5776.

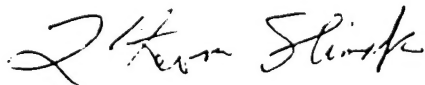
Do not return copies of this report unless contractual obligations or notice on a specific document requires its return.

This report has been approved for publication.



RALPH JAMES
Project Manager

FOR THE COMMANDER



L. KEVIN SLIMAK, GM-15
Chief, Space Vehicle Technologies
Division



BRUCE A. THIEMAN, COL, USAF
Deputy Director, Space Technology

| REPORT DOCUMENTATION PAGE | | | Form Approved OMB No. 0704-0188 | |
|---|---|--|---|--|
| Public reporting burden for this collection of information is estimated to average 1 hour per response, including the time for reviewing instructions, searching existing data sources, gathering and maintaining the data needed, and completing and reviewing the collection of information. Send comments regarding this burden estimate or any other aspect of this collection of information, including suggestions for reducing this burden to Washington Headquarters Services, Directorate for Information Operations and Reports, 1215 Jefferson Davis Highway, Suite 1204, Arlington, VA 22202-4302, and to the Office of Management and Budget, Paperwork Reduction Project (0704-0188), Washington, DC 20503. | | | | |
| 1. AGENCY USE ONLY (Leave blank) | | 2. REPORT DATE March 1997 | | 3. REPORT TYPE AND DATES COVERED Final; 10/90 to 6/96 |
| 4. TITLE AND SUBTITLE Photovoltaic Array Space Power Plus Diagnostics (PASP Plus) Experiment | | 5. FUNDING NUMBERS PE: 63401F PR: 682J TA: TG WU: 03 | | |
| 6. AUTHOR(S) D. A. Guidice, V. A. Davis*, H. B. Curtis**, D. C. Ferguson**, D. E. Hastings***, F. L. Knight***, D. C. Marvin***, K. P. Ray, P. S. Severance, J. D. Soldi***, M. Van Riet***** | | | | |
| 7. PERFORMING ORGANIZATION NAME(S) AND ADDRESS(ES) Phillips Laboratory 3550 Aberdeen Ave. SE Kirtland AFB, NM 87117-5776 | | 8. PERFORMING ORGANIZATION REPORT NUMBER PL-TR-97-1013 | | |
| 9. SPONSORING/MONITORING AGENCY NAME(S) AND ADDRESS(ES) | | 10. SPONSORING/MONITORING AGENCY REPORT NUMBER | | |
| 11. SUPPLEMENTARY NOTES Supported by *Maxwell Federal Division, Inc., 8888 Balboa Ave., San Diego, CA 92123-1506; **NASA/LeRC, 21000 Brookpark Rd., Cleveland, OH 44135; ***MIT, Cambridge, MA 02139; ****Aerospace Corp., P.O. Box 9045, Albuquerque, NM 87122; *****Space Test Program | | | | |
| 12a. DISTRIBUTION/AVAILABILITY STATEMENT Approved for Public Release; Distribution is Unlimited | | | 12b. DISTRIBUTION CODE | |
| 13. ABSTRACT (Maximum 200 Words) The Photovoltaic Array Space Power Plus Diagnostics (PASP Plus) experiment flew on the Advanced Photovoltaic and Electronics Experiments (APEX) spacecraft and operated from August 1994 to June 1996. It collected information on parasitic current collection at high positive bias, negative potential arcing at high negative bias, and long-term radiation damage on 12 different solar cell technologies. This report summarizes the results from this experiment. | | | | |
| 14. SUBJECT TERMS Photovoltaic Array Space Power PLUS Diagnostics, PASP Plus, APEX, parasitic current collection, negative potential arcing, long-term radiation damage, solar cells, radiation belts, SAMPIE, CRRES | | | 15. NUMBER OF PAGES 160 | |
| | | | 16. PRICE CODE | |
| 17. SECURITY CLASSIFICATION OF REPORT Unclassified | 18. SECURITY CLASSIFICATION OF THIS PAGE Unclassified | 19. SECURITY CLASSIFICATION OF ABSTRACT Unclassified | 20. LIMITATION OF ABSTRACT Unlimited | |

Contents

| Section | Page |
|---|------|
| 1 Introduction | 1-1 |
| 2 APEX Satellite and PASP Plus Operation | 2-1 |
| 2.1 Spacecraft Development | 2-6 |
| 2.2 Launch, Operations, and Problems | 2-11 |
| 2.3 PASP Plus Operations and Problems | 2-17 |
| 2.4 Results for the Other Experiments | 2-21 |
| 3 Instrumentation | 3-1 |
| 3.1 Test Arrays | 3-1 |
| 3.2 Experiment Control Instrumentation | 3-5 |
| 3.3 Interactions Measuring Instrumentation | 3-6 |
| 4 Photovoltaics Results | 4-1 |
| 4.1 Experiment Results | 4-3 |
| 4.2 Conclusions | 4-17 |
| 5 Arc Rate Predictions and Flight Data Analysis for the PASP Plus Experiment | 5-1 |
| 5.1 Arcing Onset Model | 5-1 |
| 5.2 Experiment Simulation and Data Analysis | 5-5 |
| 5.3 Conclusions | 5-13 |
| 6 Parasitic Current Collection by PASP Plus | 6-1 |
| 6.1 Langmuir Probe Measurements and Models | 6-1 |
| 6.2 Current Collection as a Function of Bias and Plasma Density | 6-9 |
| 6.3 Variation within a Measurement | 6-15 |
| 6.4 APEX Current Collection Characteristics and Floating Potential | 6-20 |
| 6.5 Scatter in Flight Data | 6-30 |
| 6.6 Current Collection Under Negative Bias | 6-45 |
| 6.7 The APSA Array Module | 6-48 |

Contents (Concluded)

| Section | | Page |
|---------|---|------|
| 7 | Comparison of Electron Current Collection by Space Station Solar Arrays as Measured by SAMPIE and PASP Plus | 7-1 |
| 7.1 | Background | 7-1 |
| 7.2 | SAMPIE | 7-3 |
| 7.3 | Comparison with PASP Plus Results | 7-7 |
| 7.4 | Comparisons with SAMPIE Modified ISS Cells | 7-8 |
| 7.5 | Conclusions | 7-10 |
| 8 | Dosimeter Results | 8-1 |

Figures

| Figure | | Page |
|--------|--|------|
| 2-1 | APEX deployed configuration. | 2-3 |
| 2-2 | PASP Plus instrument and test array layout. | 2-5 |
| 2-3 | APEX MEM structure. | 2-7 |
| 2-4 | APEX deployment testing. | 2-9 |
| 2-5 | APEX EMC test setup. | 2-10 |
| 2-6 | APEX integrated with Pegasus launch vehicle. | 2-12 |
| 2-7 | APEX and Pegasus mated with B-52. | 2-13 |
| 3-1 | Mini-Dome concentrator array with GaAs//GaSb multi-junction solar cells. | 3-4 |
| 3-2 | PASP Plus dosimeter with four shield thickness' (one thin disk and three thicker domes) used for measuring flux and dose of energetic electrons and protons in four energy ranges. | 3-9 |
| 4-1 | Location of solar cell modules on APEX spacecraft using module numbers. | 4-2 |
| 4-2 | Ratio of initial on-orbit power to ground-measured power for each functioning module. | 4-4 |
| 4-3 | Power degradation in Modules 0,1, and 2, showing much less degradation than expected. | 4-5 |
| 4-4 | Power degradation for Module 3 comprised of Space Station cells, showing significantly less degradation than predicted. | 4-7 |
| 4-5 | Module 5 containing APSA blanket shows less degradation than predicted | 4-8 |
| 4-6 | Module 4 and 6 data on gallium arsenide solar cells with 3.5 mil germanium substrates. | 4-9 |
| 4-7 | Module 8 GaAs/Ge solar cells have wrap-through contacts and Module 11 cells have conventional contacts. | 4-9 |
| 4-8 | Power degradation of tandem AlGaAs/GaAs cell circuit. | 4-10 |
| 4-9 | Power degradation for two voltage matched GaAs/CIS circuits, showing better than predicted radiation tolerance. | 4-11 |
| 4-10 | Power degradation of indium phosphide module. | 4-12 |
| 4-11 | Amorphous silicon array power performance compared with pre-flight prediction based on light-induced degradation losses only. | 4-13 |
| 4-12 | Power degradation of GaAs/GaSb concentrator array significantly exceeds prediction. | 4-14 |
| 4-13 | Schematic of Module 15 minidome optical assembly. | 4-14 |
| 4-15 | Current and voltage degradation of GaAs/GaSb concentrator array. | 4-15 |
| 4-15 | Clear view data and five-day average data for silicon Module 0. | 4-16 |
| 4-16 | Clear view data and five-day average data for GaAs Module 4. | 4-16 |
| 4-17 | Clear view and five-day average data for concentrator Module 15. | 4-17 |

Figures (Continued)

| Figure | | Page |
|--------|---|------|
| 5-1 | Solar cell module system. | 5-1 |
| 5-2 | Arc initiation process. | 5-3 |
| 5-3 | PASP Plus conventional geometry cell temperatures. | 5-6 |
| 5-4 | Standard silicon array Module 1 arc rate variation with voltage. | 5-7 |
| 5-5 | Standard silicon array Module 2 arc rate variation with voltage. | 5-7 |
| 5-6 | Hastings/Cho model fit to standard silicon array Module 2. | 5-8 |
| 5-7 | Theoretical ion charging time: silicon array Module 2. | 5-9 |
| 5-8 | Standard silicon array Module 2 arc rate variation with ion flux at -300 V. | 5-9 |
| 5-9 | Standard silicon array Module 2 arc rate variation with ion flux at -330 V. | 5-10 |
| 5-10 | APSA array Module 5 arc rate variation with cell temperature at -300 V. | 5-11 |
| 5-11 | Simulated APSA array Module 5 arc rate variation with cell temperature at -300 V. | 5-11 |
| 5-12 | APSA array Module 5 arc rate variation with voltage. | 5-12 |
| 6-1 | Altitude of the APEX spacecraft on August 8, 1994. | 6-2 |
| 6-2 | Attitude of the APEX spacecraft on August 8, 1994. | 6-2 |
| 6-3 | Plasma density at the APEX spacecraft on August 8, 1994. | 6-3 |
| 6-4 | Plasma temperature at the APEX spacecraft on August 8, 1994. | 6-4 |
| 6-5 | APEX floating potential on August 8, 1994. | 6-5 |
| 6-6 | Altitude of the APEX spacecraft on February 12, 1995. | 6-6 |
| 6-7 | Attitude of the APEX spacecraft on February 12, 1995. | 6-6 |
| 6-8 | Plasma density at the APEX spacecraft on February 12, 1995. | 6-7 |
| 6-9 | Plasma temperature at the APEX spacecraft on February 12, 1995. | 6-7 |
| 6-10 | APEX floating potential on February 12, 1995. | 6-8 |
| 6-11 | Probe potential with respect to plasma ground as a function of the probe bias. | 6-9 |
| 6-12 | Collected current as a function of the probe bias. | 6-10 |
| 6-13 | Collecting area as a function of cell bias and plasma density. | 6-12 |
| 6-14 | Differential charging across solar cell cover glass. | 6-16 |
| 6-15 | Time to decay from 100 V for Module 4 cover glass. | 6-17 |
| 6-16 | Average time variation of Module 4 leakage current for various plasma densities. | 6-18 |
| 6-17 | Maximal time variation of Module 4 leakage current for various plasma densities. | 6-19 |
| 6-18 | Time variation of Module 4 leakage current between $5.62 \times 10^{10} \text{ m}^{-3}$ and $1.78 \times 10^{10} \text{ m}^{-3}$ for the ten sequences with the highest value of ratio at the second point. | 6-19 |

Figures (Continued)

| Figure | | Page |
|--------|---|------|
| 6-19 | Time variation of Module 4 leakage current between $5.62 \times 10^{11} \text{ m}^{-3}$ and $1.78 \times 10^{11} \text{ m}^{-3}$ for the ten sequences with the highest value of ratio at the second point. | 6-20 |
| 6-20 | Count rate as a function of calibration beam and fits for ESA similar to the one on APEX. | 6-21 |
| 6-21 | Estimated potential as a function of true potential. | 6-23 |
| 6-22 | Ion collecting area as a function of potential as estimated from leakage current and ESA measurements. | 6-23 |
| 6-23 | Ion collecting area as a function of potential as estimated from leakage current (separated by module) and ESA measurements. | 6-24 |
| 6-24 | Estimated current to APEX compared with the measured current collected by a biased module. | 6-25 |
| 6-25 | Estimated spacecraft ground potential compared with the ESA measurements. | 6-26 |
| 6-26 | Ion collecting area as a function of potential as estimated from leakage current and ESA measurements. | 6-27 |
| 6-27 | Estimated spacecraft ground potential compared with the ESA measurement assuming spherical current collection. | 6-28 |
| 6-28 | Collecting area as a function of bias minus the value of the floating potential as determined from the ESA measurement for Module 2. | 6-29 |
| 6-29 | Collecting area as a function of bias minus the value of the floating potential as determined from the current, density, and temperature measurements and spherical current collection for Module 2. | 6-29 |
| 6-30 | Collecting area as a function of density for 4 specific applied bias values for Modules 3, 4, 5, and 11. | 6-31 |
| 6-31 | Collected current as a function of density for 4 specific applied bias values for Modules 3, 4, 5, and 11. | 6-32 |
| 6-32 | Collecting area as a function of density for 4 specific applied bias values for Module 4 from day 120 to day 129 of 1995. | 6-33 |
| 6-33 | Collecting area as a function of applied bias for Module 4 from day 120 to day 129 of 1995. | 6-33 |
| 6-34 | Collecting area as a function of density for specific values of bias minus the value of the floating potential as determined from the ESA measurement for Module 4. | 6-41 |
| 6-35 | Collecting area as a function of density for specific values of bias minus the value of the floating potential as determined from the current, density, and temperature measurements and spherical current collection for Module 4. | 6-41 |
| 6-36 | Current sweeps for Case 1. | 6-43 |

Figures (Continued)

| Figure | | Page |
|--------|--|------|
| 6-37 | Calculated current as a function of applied bias for three different first crossover values. | 6-44 |
| 6-38 | Collected current as a function of applied bias for negative bias for days 94291 to 94294. | 6-45 |
| 6-39 | Collected current as a function of applied bias for negative bias for days 95080 to 95089. | 6-46 |
| 6-40 | Collected current as a function of applied bias for negative bias for days 95190 to 95196. | 6-46 |
| 6-41 | Effective circuit for collection of current by Module 5. | 6-49 |
| 6-42 | Current divided by applied bias for Module 5 during positive biasing when the measured plasma density is under $2 \times 10^9 \text{ m}^{-3}$ and the array modules are in the wake for the entire mission. | 6-50 |
| 6-43 | Collecting area as a function of bias for Module 5, accounting for internal resistance. | 6-50 |
| 7-1 | SAMPIE's position on Shuttle Columbia's MPES carrier. | 7-4 |
| 7-2 | SAMPIE 4-cell Space Station solar array. | 7-5 |
| 7-3 | Plasma electron current collected by Space Station 4 cell array. | 7-6 |
| 7-4 | Effective electron current collection areas (cm^2) for Space Station 4-cell array, corrected for plasma densities and temperatures. | 7-7 |
| 7-5 | Predictions of electron collection area (cm^2) of SAMPIE experiment 20 array, from EWB and the Tiger Team. | 7-8 |
| 7-6 | Effective collection area (cm^2) of the PASP Plus Space Station 4 cell array, compared to that of SAMPIE experiment 20. | 7-9 |
| 7-7 | Electron currents at 100 V by the SAMPIE modified Space Station cells, normalized to a 4-cell edge length and a plasma density of $2.8 \times 10^{11} \text{ cm}^{-3}$ vs. coverslide overhangs. | 7-10 |
| 7-8 | Electron currents collected at 100 V by modified Space Station cells, Figure 7-8 normalized to 4-cell edge length and a plasma density of $2.8 \times 10^{11} \text{ cm}^{-3}$, for different values of the length of cell edge adhesive removed. | 7-11 |
| 7-9 | Expected 4-cell effective electron collection area for Space Station cells, based on a hypothesis for enhanced edge collection. | 7-12 |

Figures (Concluded)

| Figure | | Page |
|--------|--|------|
| 8-1 | APEX orbits superimposed on results from CRRES dosimeter combined HILET and LOLET dome 2 (232.5 mils Al) binned from CRESS orbits 4 to 1067 (27 July 1990 to 12 October 1991). | 8-3 |
| 8-2 | HILET delta dose (protons > 35 MeV). | 8-4 |
| 8-3 | LOLET total dose. | 8-5 |
| 8-4 | HILET total dose. | 8-5 |
| 8-5 | HILET dose per day. | 8-6 |
| 8-6 | HILET dose per day (expanded scale). | 8-7 |
| 8-7 | LOLET dose per day. | 8-7 |
| 8-8 | Single event upsets. | 8-8 |
| 8-9 | APEX SEU data. | 8-9 |
| 8-10 | APEX SEU-dosimeter correlation. | 8-9 |

Tables

| Table | | Page |
|-------|---|------|
| 2-1 | APEX Experiment Complement | 2-2 |
| 2-2 | APEX Spacecraft Requirements | 2-4 |
| 2-3 | Data Collection Periods for Positive Biasing | 2-19 |
| 2-4 | Data Collection Periods for Negative Biasing | 2-20 |
| 3-1 | PASP Plus Solar Arrays | 3-2 |
| 3-2 | Dome Thickness and Electron and Proton Energy Ranges for the PASP Plus Dosimeter | 3-9 |
| 4-1 | Summary Description of PASP Plus Modules | 4-6 |
| 4-2 | Comparison of Module 0 Cell Performance with Two Types of BSFR Cells | 4-7 |
| 5-1 | Experimental Arcing Probability | 5-12 |
| 5-2 | Simulated and Experimental Arcing Onset Voltages | 5-13 |
| 6-1 | Solar-Cell and Module Panel Areas for the PASP Plus Planar Arrays | 6-14 |
| 6-2 | Collecting Area in Square Meters at Minimum Leakage Current | 6-15 |
| 6-3 | Details of parameters for a bias value of 148 V and a density between 8×10^9 and $9.9 \times 10^9 \text{ m}^{-3}$ | 6-35 |
| 6-4 | Details of parameters for a bias value of 238 V and a density between 1.6×10^{10} and $1.99 \times 10^{10} \text{ m}^{-3}$ | 6-38 |
| 6-5 | Current Voltage Linear Characteristic Days 94291 to 94294 | 6-47 |
| 6-6 | Current Voltage Linear Characteristic Days 95080 to 95089 | 6-47 |
| 6-7 | Current Voltage Linear Characteristic Day 95290 to 95296 | 6-47 |
| 8-1 | APEX Dosimeter Characteristics | 8-2 |
| 8-2 | Correlation Coefficients | 8-10 |

Executive Summary

D. A. Guidice, Phillips Laboratory, Hanscom AFB

In providing electrical power to post-2000 space systems, photovoltaic subsystems may be required to operate at higher voltage levels (to reduce cable weight and/or I^2R losses) and to use higher-efficiency solar-cell materials less susceptible to space-radiation degradation. Before advanced photovoltaic technologies are routinely used on operational spacecraft, various environmental interactions questions need to be answered by detailed investigations in the actual space environment. The Photovoltaic Array Space Power Plus Diagnostics (PASP Plus) experiment, developed by Phillips Laboratory (funded by PL's PE 63410F) with support from NASA's Lewis Research Center, was flown for this purpose.

PASP Plus's objectives were to measure: (a) the plasma leakage (or "parasitic") current when arrays were biased to high positive voltage levels (up to +500 V), (b) the arcing parameters when arrays were biased to high negative voltage levels (up to -500 V), and (c) the power output degradation under measured radiation exposure, for arrays having different mechanical configurations and solar-cell materials.

On 3 August 1994, the APEX spacecraft, containing the PASP Plus experiment as its prime payload, was successfully launched into a 70° inclination, 363 km by 2552 km elliptical orbit by a standard Pegasus booster. During its first year in orbit, PASP Plus collected eight months of solar-array ionospheric-plasma interaction data and a year of radiation-induced degradation data.

On 11 August 1995, the PASP Plus Controller ceased to operate properly and the array environmental-interactions data collecting could not be continued. An additional eight months of dosimeter data was obtained before the 2 June 1996 complete failure of the APEX satellite.

PASP Plus obtained an order of magnitude more flight data on solar-array performance under high-voltage operation and space radiation conditions than all previous space-borne photovoltaic experiments combined. Its results are detailed in this report.

Chapter 1

Introduction

D. A. Guidice, Phillips Laboratory, Hanscom AFB
V. A. Davis, Maxwell Federal Division, Inc.

With the need for higher power levels, longer lifetimes, and operations in higher radiation environments, space systems of the 1990s and beyond require more efficient space-power sources. In supplying electrical power for these new systems, consideration must be given to operating photovoltaic subsystems at higher voltage levels to reduce cable weight and/or minimize I^2R losses. New solar-cell materials are being developed for higher efficiency and less susceptibility (reduced solar cell degradation) to space radiation. Before using these new technology space-power subsystems on operational spacecraft, various environmental interactions questions must be answered by investigations in the actual space environment. The Photovoltaic Array Space Power Plus Diagnostics (PASP Plus) experiment was developed and flown for this purpose.

Starting in late 1985, the Air Force Geophysics Laboratory (AFGL, now part of Phillips Laboratory, PL), with the support of the Aero-Propulsion & Power Laboratory (now part of Wright Laboratory, WL), put together an experiment to measure space environment effects on solar-array performance. All funding for the experiment has come from AFGL's PE63410F. The original objectives of the PASP Plus experiment were limited to the effects of space-plasma interactions on high-voltage solar array operation at low altitudes. The Jet Propulsion Laboratory (JPL) developed a brassboard instrument (aimed at a Shuttle flight), capable of biasing up to six arrays in eleven fixed voltage steps within the limits of -500 V and $+500$ V (Ref. 1-1 and 1-2). However, in early 1990, the Air Force Space Test Program (STP) offered the PASP Plus experiment a flight on a satellite put into orbit by a Pegasus launch vehicle. PASP Plus was to be part of the APEX (Advanced Photovoltaic and Electronics Experiments) mission set up to fly it and two small "radiation effects on electronics" experiments, CRUX/CREDO and FERRO. The Spaceflight Plan for APEX was approved by Hq USAF on 3 October 1990. Because of the enhanced opportunity provided by APEX, an elliptical (originally 350 km by 1950 km), near-polar (inclination of 70°) orbit with a 1 to 3 year lifetime, Phillips Laboratory decided to

broaden the scope of the PASP Plus experiment to include investigation of the effects of space radiation dose on long-term solar-array performance (Ref. 1-3). When the availability of a ride for PASP Plus became known to the photovoltaic development community, additional new technology arrays were offered to PASP Plus, and the number of arrays to be flown on PASP Plus was increased (eventually) to twelve.

To make PASP Plus suitable for APEX, a new controller with greatly increased functional capability and drastically reduced weight was developed by Amptek, Inc. of Bedford, MA. With the help of NASA Lewis Research Center personnel, the twelve test arrays were mounted to the payload shelf and one of the deployed panels of the APEX satellite. Diagnostics sensors (Langmuir probe, transient pulse monitor, dosimeter, etc.) were incorporated into the experiment. PASP Plus successfully completed all functional and environmental testing, including "one-sun simulated" thermal-vacuum tests at the Boeing facility at Kent, WA to give us preflight "array performance vs. temperature" characteristics for later comparison with flight data (Ref. 1-4). The PASP Plus experiment was delivered to Orbital Sciences Corporation for integration into APEX on 9 July 92.

The objectives of the PASP Plus experiment are:

- a. To measure the plasma "leakage" current for different kinds of arrays subjected to positive biasing levels up to +500 V, simulating array operation at high positive voltages.
- b. To measure the arcing parameters for different kinds of arrays subjected to negative biasing levels up to -500 V, simulating array operation at high negative voltages.
- c. To measure the long-term degradation in the output power of arrays having different mechanical configurations and solar-cell materials when exposed to space radiation.
- d. To establish cause-and-effect relationships between array performances (interactions and output-power degradation) and environmental conditions (Ref. 1-3).

On 3 August 1994, the APEX spacecraft was successfully launched on a standard Pegasus booster, released from a NASA B-52 over the Western Test Range off the coast of California.

The booster placed APEX into a 70° inclination, 363 x 2552 km orbit. PASP Plus collected solar array test data for a total of 8 months during the first year in orbit. On 11 August 1995, the PASP Plus Controller ceased to operate and the solar array experiments could not be continued. After this, an additional 8 months of dosimeter data was obtained before the 2 June 1996 satellite catastrophic failure. PASP Plus provides an order of magnitude more flight data on solar array operation under both normal conditions and high voltage conditions than all previous experiments combined.

This document describes the PASP Plus experiment and its results. Chapter 2 describes the development and operations of the APEX spacecraft and the PASP Plus experiment. Chapter 3 describes the PASP Plus instrumentation. Chapters 4, 5, and 6 describe the results of the solar array experiments. Chapter 7 compares the results from PASP Plus with those from a similar, shorter-term, shuttle experiment, SAMPIE. Chapter 8 describes the additional information gained from the dosimeter.

References for Chapter 1

- 1-1. Guidice, D.A., "Photovoltaic Array Space Power Plus Diagnostics Experiment," *Third Annual Workshop on Space Operations, Automation and Robotics (SOAR '89)*, NASA Conf. Publ. 3059, pp. 515-519, March 1990.
- 1-2. Guidice, D.A., Severance, P.S., and Reinhardt, K.C., "Measurement of High-Voltage and Radiation-Damage Limitations to Advanced Solar Array Performance," *Space Photovoltaic Research and Technology 1991*, NASA Conf. Publ. 3121, pp. 33-1 to 33-10, August 1991.
- 1-3. Guidice, D.A., "PASP Plus: An Experiment To Measure Space-Environment Effects on Photovoltaic Power Subsystems," *Fifth Annual Workshop on Space Operations, Applications and Research (SOAR '91)*, NASA Conf. Publ. 3127, pp. 662- 668, February 1992.
- 1-4. Curtis, H., Guidice, D., Severance, P., and Piszczor, M., "Results of Thermal Vacuum Tests for the PASP Plus Flight Modules," *Proc. of XII Space Photovoltaic Research and Technology Conf.*, NASA Conf. Publ. 3210, pp. 289-297, May 1993.

Chapter 2

APEX Satellite and PASP Plus Operation

M. Van Riet, Space Test Program
D.A. Guidice, Phillips Laboratory, Hanscom AFB
F. L. Knight, Aerospace Corporation

The Space Test Program (STP) Advanced Photovoltaic and Electronics Experiments (APEX) mission carried three Department of Defense experiment payloads as shown in Table 2-1. The primary experiment on APEX was the Photovoltaic Array Space Power Plus Diagnostics (PASP Plus) experiment. PASP Plus was developed by the Geophysics Directorate of the Air Force Phillips Laboratory (PL) to provide a space test and demonstration of 12 advanced photovoltaic arrays. A variety of diagnostic instruments were used to quantify the arrays' performance. Also, a dosimeter was flown to measure the natural radiation that damages solar cells and causes decreased array performance.

Two secondary experiments were also flown. The Cosmic Ray Upset Experiment (CRUX/CREDO) was sponsored by the Air Force's Space Systems Division (now Space and Missile Systems Center) and developed by the Goddard Space Flight Center (GSFC). The purpose of CRUX/CREDO was to develop data to validate and update modeling techniques that are used to predict upset rates in microcircuit memory devices when highly energetic cosmic rays (heavy ions and protons) pass through them. It carried a variety of state-of-the-art memory "devices under test" that were programmed to a known state and then interrogated a short time later to determine if high energy particles had caused a change in state.

The Thin-film Ferroelectric Experiment (FERRO) was developed by the Naval Postgraduate School (NPS). FERRO provided a flight test for the integral component of thin-film ferroelectric memories—ferroelectric capacitors. Various tests simulating typical uses of these capacitors were performed as they were exposed to the ionizing radiation of space.

Table 2-1. APEX Experiment Complement

| Experiment Description | | | | | | |
|-------------------------|---|------------------------|------------------|---|---------------|------------|
| Designator | Experiment | | | | | |
| AFGL-803 | PASP Plus —Photovoltaic Array Space Power Plus Diagnostics Determine operating voltage and performance limits of different kinds of solar array designs under adverse space plasma and radiation conditions. Verify ground tests and provide performance comparison. | | | | | |
| NPS-001 | FERRO —Thin-film Ferroelectric Experiment Test the integral component of ferroelectric memory (ferroelectric material in capacitor form). Demonstrate non-volatility of ferroelectric materials under simulated working conditions and ionizing radiation. | | | | | |
| SSD-001 | CRUX/CREDO —Cosmic Ray Upset Experiment Validate model used to predict upset rates of memory microcircuits. Obtain flight upset data on memory microcircuits; aid circuit designers. | | | | | |
| Experiment Requirements | | | | | | |
| Experiment | Weight (lbs) | Power (watts) avg/peak | Telemetry (kbps) | Stabilization (degrees) control/knowledge | Field-of-View | Orbit (km) |
| PASP Plus | 120 | 90/140 | 3 | 0.5 deg/0.5 deg | Sun-pointing | Near Polar |
| CRUX/CREDO | 30 | 20 | <1 | no reqmt. | no reqmt. | Near Polar |
| FERRO | 5 | 5/10 | <1 | no reqmt. | no reqmt. | Near Polar |

These experiments were flown on a PegaStar[®] spacecraft bus developed for STP by the Orbital Sciences Corporation (OSC). In the PegaStar approach, the existing launch operations capabilities of the Pegasus[®] Air-Launched Vehicle are augmented with those needed for on-orbit operations. In this way, the third stage of the Pegasus becomes a fully-functional spacecraft bus capable of meeting the APEX experiments' requirements. By modifying the spacecraft structure

and upgrading some components so that they can do “double duty” (serving both the spacecraft and the launch vehicle), PegaStar can deliver more useful payload to orbit than can a separate Pegasus-launched satellite. Two PegaStar spacecraft have been developed to date—APEX, and its sister spacecraft, known as “SeaStar,” which was developed for NASA’s Goddard Space Flight Center.

The design requirements for the spacecraft are shown in Table 2-2. A computer model of the APEX spacecraft in its flight configuration is shown in Figure 2-1. With PegaStar, the launch vehicle avionics that were previously attached to the Pegasus thrust tube and avionics deck have been moved and are now attached to two of the spacecraft bus panels. Directly forward of the bus panels is an Avionics Shelf on which the experiment electronics boxes are mounted. The shelf has a hexagonal shape and is 37 inches wide (measured from parallel sides). The Avionics Shelf

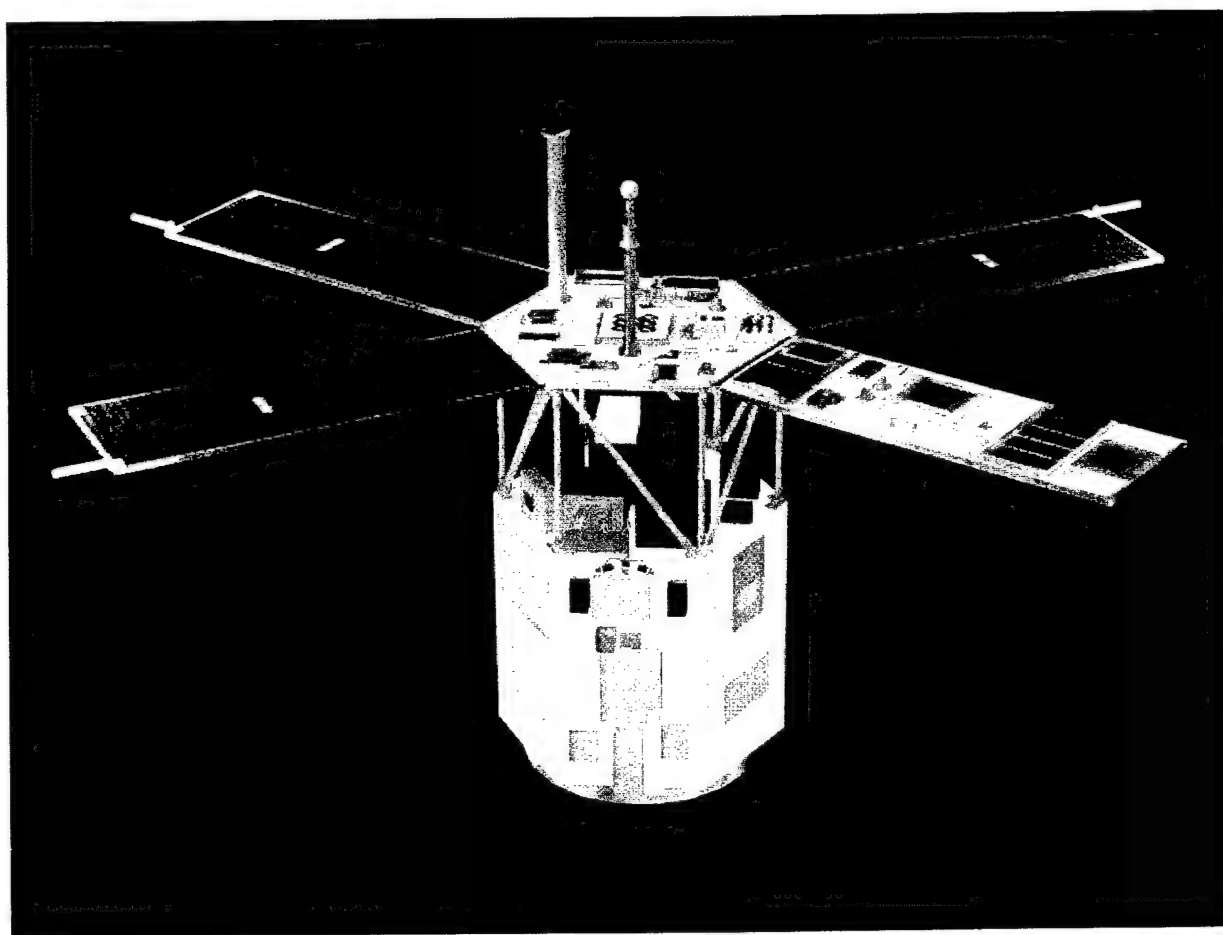


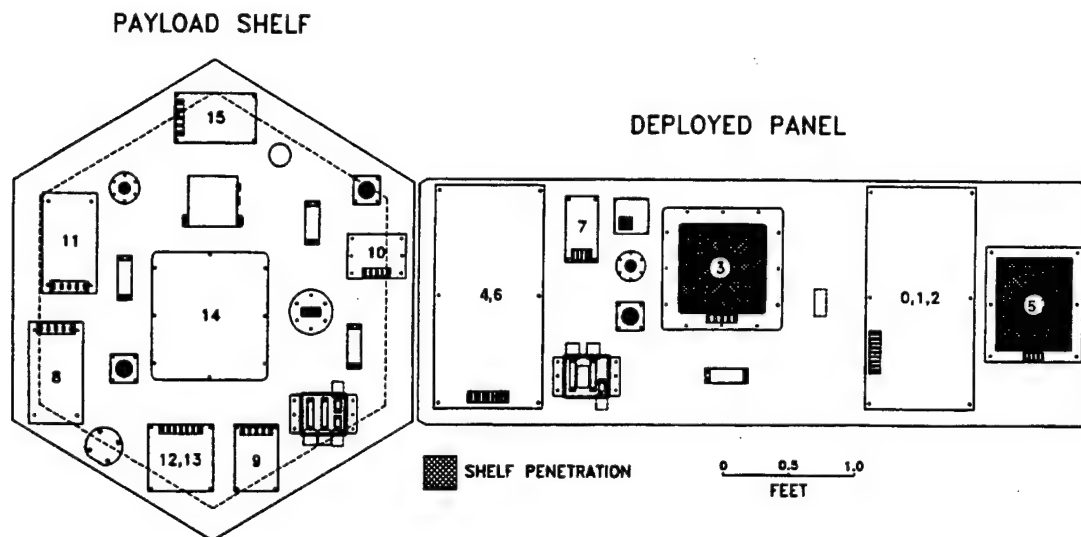
Figure 2-1. APEX Deployed Configuration. (Courtesy Capt. Mike Van Riet)

Table 2-2. APEX Spacecraft Requirements

| Requirements |
|--|
| MIL-STD-343, Class C |
| One year design life; three year goal |
| Reliability: 0.9 |
| SGLS Compatible |
| High radiation exposure orbit: 195+10 nm x 1000+100 nm, 70° inc. |
| 3-axis stabilized: + 0.5 deg. (5 deg. in roll) |
| Payload weight capability: 155 lbs. |
| Low outgassing |
| Exp. Data Storage (MB): > 26 |
| Exp. Power: 170 peak., 113 average |
| Radiation resistance: > 5 krad |

includes the electronic boxes for the PASP Plus instruments (Controller, Langmuir Probe, Transient Plus Monitor (TPM), Electrostatic Analyzer (ESA), Dosimeter, Electron Emitter) and the other APEX experiments, CRUX/CREDO and FERRO. This shelf is connected by a truss structure to a similarly shaped Payload Shelf, on which some of the PASP Plus solar arrays and diagnostic devices are mounted. Seven of the PASP Plus test arrays, including the two concentrator arrays, are mounted on the top of the Payload Shelf. The APEX sun sensor, which keeps the satellite pointing toward the sun (except during the portion of the orbit when the sun is eclipsed by the earth) to within $\pm 0.5^\circ$, is mounted between the two concentrators. Mounted on the Payload Shelf are two 24-inch booms, one holding the Langmuir Probe sensor head and the other holding the APEX magnetometer (used to maintain orientation when the satellite is in eclipse).

In order to provide more mounting area for the PASP Plus arrays and sensors, a deployed Payload Panel is also provided. This panel was deployed at the same time as the three spacecraft solar array panels. The Deployed Payload Panel contains the remaining five test arrays and a few small sensors. The Space Station and APSA (Advanced Photovoltaic Solar Array) arrays have cutouts in the panel so that the arrays are open to space on both sides, as they would be in their



| Item No | PASP Plus Test Module | Item No | Instrument |
|---------|------------------------------|----------------|------------------------------|
| 0, 1, 2 | Si Standard | 18, 19, 20, 21 | TPM E-field Sensors |
| 3 | Si Wrap-Thru (Space Station) | 23 | LP Boom & Sensor |
| 5 | Thin Si (2 mil), APSA | 27 | PASP Sun Sensor |
| 4, 6 | GaAs on Ge, 3.5 mil | 30, 31 | Quartz Crystal Microbalances |
| 7 | AlGaAs/GaAs | 32, 33, 34 | Calorimeters |
| 8 | GaAs on Ge, 7 mil, Wrap-Thru | | |
| 9 | Amorphous Si | | |
| 10 | InP | | |
| 11 | GaAs on Ge, 7 mil | | |
| 12, 13 | GaAs/CuInSe ₂ | | |
| 14 | GaAs Mini-Cassegrainian | | |
| 15 | GaAs/GaSb Mini-Dome | | |

Figure 2-2. PASP Plus Instrument and Test Array Layout.

regular operational configuration. Three of the TPM's E-field sensors are mounted triangularly on the payload shelf, and the fourth is mounted on the Deployed Payload Panel. Figure 2-2 shows the Payload Shelf and the Deployed Payload Panel layout. At the end of each of the solar array panels and the Deployed Payload Panel are the spacecraft antennas. There are two uplink antennas and two downlink antennas.

2.1 Spacecraft Development

In the Summer and Fall of 1992, the three APEX experiments were delivered to OSC's integration facility in Chantilly, Virginia. After delivery, the experiments underwent a comprehensive suite of "bench tests" to insure the compatibility of the experiment interfaces with the APEX spacecraft avionics prior to integration with the actual flight hardware. These tests were first performed with experiment simulators and a set of non-flight avionics components that comprised the APEX Electrical Engineering Model (EEM). The EEM was also used to perform extensive software development tests prior to installing the flight software on the flight avionics units. Additional tests were performed to insure that the spacecraft was compatible with the Pegasus launch vehicle and with the Air Force Satellite Control Network (AFSCN).

Meanwhile, an engineering model of the flight structure was also developed. This Mechanical Engineering Model (MEM), shown in Figure 2-3, was used to verify and refine the flight structure design. It was designed to be identical to the flight structure, except that mass models were used to simulate the satellite and experiment avionics. The MEM was subjected to a variety of mechanical tests, including pyrotechnic shock, static loads, and random vibration.

One of the most important findings of these tests was that some spacecraft secondary structures experienced higher than expected vibration levels during the MEM random vibration test. In order to reduce these vibration levels, a shock absorbing material (3M Corp. ISD112) was installed at strategic locations. A retest of MEM random vibration was performed in January of 1993, and it confirmed that the new design was effective in reducing vibration levels.

The Orbital Data Processing (ODP) system for APEX was also developed at the Air Force Geophysics Directorate at Hanscom Air Force Base (AFB), MA. This system is a modification of a system developed for the Space Test Program's Combined Release and Radiation Effects Satellite, which was launched in June 1991. The ODP system was used to process spacecraft telemetry tapes recorded at the remote tracking stations of the AFSCN. It stripped out the spacecraft telemetry and experiment data and formatted it so that the experiment agencies could analyze the experiment operations. Sample telemetry tapes were prepared using the EEM to provide a first test of the ODP system.



Figure 2-3. APEX MEM Structure. (Photo Courtesy Orbital Sciences Corp.)

Integration and Testing

Over the subsequent months, the spacecraft was built up in a series of steps. The Attitude Control System was developed and tested with a computer simulation. Then the flight components were used for "hardware-in-the-loop" testing, to insure that the spacecraft would properly respond to correct attitude errors. After the proper operation of the components and the software was verified, they were installed on the flight unit. The spacecraft electrical components and other avionics were also functionally tested and installed, and the experiments were integrated with the flight vehicle and calibrated.

By the Fall of 1993, the spacecraft was ready to be tested as a unit. To do this, a comprehensive set of functional tests was developed. This Comprehensive Performance Test (CPT) was performed before environmental testing in order to verify proper operation of spacecraft systems as an integrated unit. Another CPT was planned for after environmental testing to insure that no damage had been done to the spacecraft and that it was ready to be launched.

The CPT included simulations of launch and on-orbit operations. Also, the spacecraft response to various anomalies and spacecraft contingencies that might be expected to occur on-orbit was tested. Spacecraft performance margins were measured by subjecting the spacecraft to increasingly severe "stress tests." For example, commands were sent to the spacecraft at faster and faster rates to measure processing margins. Invalid commands were sent to the spacecraft to insure that the spacecraft would reject them. Communication links were tested by commanding the spacecraft with attenuated "hard-wired" links from the ground support equipment. In addition, commanding was performed using the spacecraft antennas.

The CPT proved to be extremely valuable for discovering software errors and unexpected system responses. As the test proceeded, software improvements were made and portions of the CPT re-run to verify the correctness of the software changes. In addition, telemetry tapes created during the test were sent to the ODP facility at Hanscom AFB so that an "end-to-end" test of the ODP system could be performed. The test insured that the system was ready to support orbital operations. Finally, after all software improvements had been incorporated, a formal CPT was run to insure that the spacecraft was ready for environmental testing.

Environmental Testing

The first environmental test to be performed was the Pyroshock test. In this test, the spacecraft was suspended from a crane and instrumented to record shock levels at various locations. The spacecraft separation system was fired to separate the satellite from an inert Pegasus third stage motor. After the test, a Limited Performance Test (LPT) was performed to insure that the spacecraft had survived without damage. The LPT was run after all of the environmental tests and was composed of a subset of the tests that comprise the CPT.

Tests were run to verify successful deployment of the three solar array panels and the experiment payload panel (see Figure 2-4). Since the launch locks that secure the panels used paraffin actuators instead of pyrotechnic devices, it was possible to repeatedly test the actual flight hardware. Heat was used to melt the paraffin in the actuators, causing it to expand and drive a piston that released the launch locks. When the heat was removed, the paraffin re-solidified and the launch locks could be secured until the next deployment. The spacecraft solar array panels

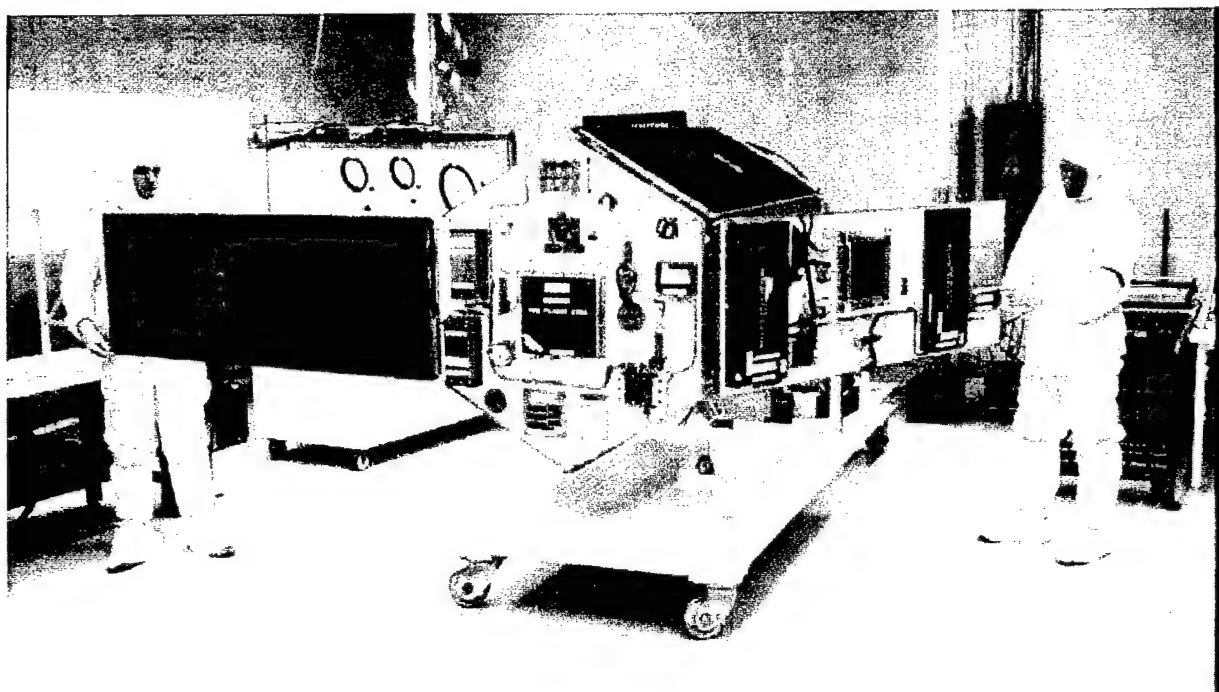


Figure 2-4. APEX Deployment Testing. (Photo courtesy Orbital Sciences Corp.)

were spring loaded, with the force provided by the deformed spring driving the deployment action. Since the experiment payload panel required more torque to deploy properly, an active mechanism was provided to drive the deployment of this panel. It also utilized a paraffin actuator.

In January of 1994, the APEX spacecraft was shipped to the Naval Research Laboratory in Washington, DC for the remaining environmental tests. In the Electromagnetic Compatibility (EMC) Test (Figure 2-5), the susceptibility of the spacecraft to radio frequency radiation was measured by operating the spacecraft while it was exposed to various frequencies of such radiation. Following this test, the Thermal Vacuum/Thermal Balance Test was performed. The spacecraft was subjected to eight hot and cold cycles while operating in vacuum conditions. It was during this test that the only hardware failure during environmental testing was experienced. A DC-DC converter in an avionics box known as the Attitude Control Electronics (ACE) failed during the second hot cycle. This caused concern since there were twelve similar DC-DC converters made by the same manufacturer installed on various boxes throughout the spacecraft. OSC and the Aerospace Corporation jointly undertook an extensive failure analysis to determine why the converter failed, and the implications of the failure for the other boxes that used these



Figure 2-5. APEX EMC Test Setup. (Photo courtesy Orbital Sciences Corp.)

converters. The results of this analysis showed that the converter failed because it did not have an adequate thermal conduction path to properly remove the heat produced in vacuum conditions. It was determined that there were no inherent part quality problems that would require the removal and replacement of the other converters. This prevented a long and costly delay that would have resulted should replacement of the converters and the subsequent re-testing have been required. Additional heat sinking was added to the converter mounting in the ACE box and at some other converter locations. The thermal vacuum testing was resumed and was completed without further incident.

After the random vibration test was performed on the vehicle, it was shipped back to OSC. A mass properties test was performed to measure the spacecraft weight and inertial properties. A second mechanical motion test was done to insure that the deployment mechanisms had not been damaged during the environmental testing. Finally, the CPT was re-run in April 1994 to verify that the spacecraft was ready for shipment to the launch site.

Launch Site Processing

In May 1994, APEX was shipped to NASA's Dryden Flight Research Center at Edwards AFB in California. APEX was to be the third STP spacecraft launched with the Pegasus launch vehicle in a period of three months. The Space Test Experiments Platform (STEP) Mission Two was successfully launched on 19 May using a standard Pegasus. However, there was a failure of the Pegasus XL launch vehicle during the launch of STEP Mission One on 27 June. Preparations to launch APEX were slowed somewhat as OSC, the USAF, Aerospace and others assessed the STEP launch failure. The spacecraft team used the additional time to continue to run orbital simulations developed during the CPT. It was quickly determined that the Pegasus failure was due to control instability that was specific to the XL version of the vehicle. Since APEX would fly on a standard Pegasus, launch site processing resumed in earnest, and a launch date of 3 August was established.

Due to the nature of the experiments being flown, a target orbit was established that would maximize the spacecraft's exposure to the natural radiation of space. The original target orbit was 360 by 1950 km (195 by 1000 nautical miles), with an inclination of 70 degrees. However, since the primary experiment as well as some launch vehicle and spacecraft components had been delivered with lighter weight units than those in the original mass budget, the launch weight of 572 pounds was somewhat less than originally planned. So the mission apogee was targeted higher in order to increase the spacecraft's exposure to the Van Allen radiation belts. In fact, the desired apogee was "as high as possible" for this reason.

The APEX spacecraft was integrated onto the launch vehicle (Figure 2-6) and the combined system attached to NASA's B-52, tail number 008, on 2 August.

2.2 Launch, Operations, and Problems

At 07:37 PDT on 3 August 1994, the APEX spacecraft was successfully launched on a standard Pegasus booster, (Figure 2-7) released from a NASA B-52 over the Western Test Range off the coast of California. This launch was the last standard Pegasus mission to be flown out of

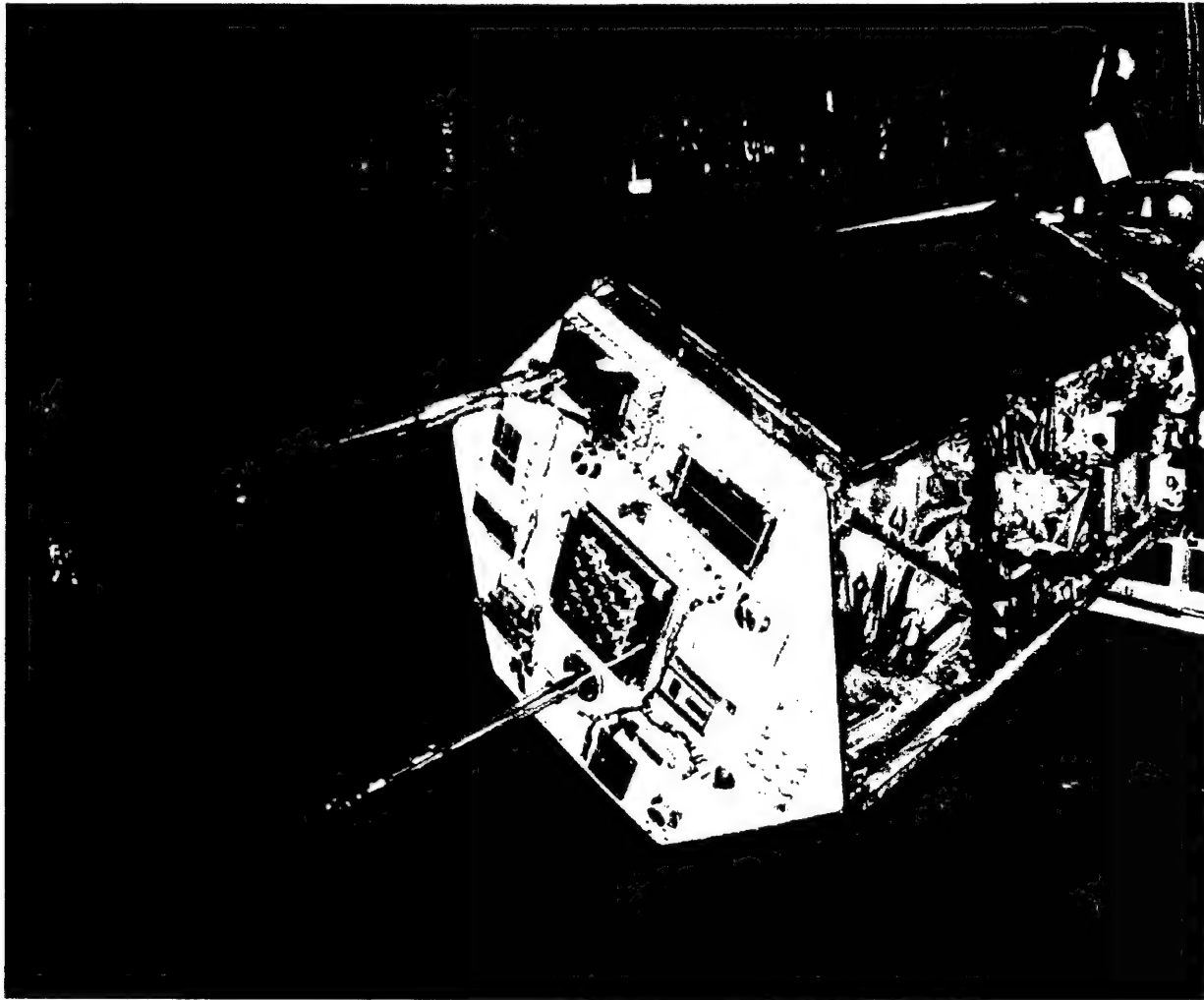


Figure 2-6. APEX Integrated With Pegasus Launch Vehicle. (Photo courtesy Orbital Sciences Corp.)

Edwards Air Force Base using the venerable B-52 #008, distinguished for its launches of notable test vehicles such as the X-15.

The B-52 took off at 06:55 PDT, after a slight delay needed to close the air conditioning panel of the Pegasus fairing. This was the only launch “anomaly” seen on the mission; everything else proceeded perfectly. The spacecraft was active during launch, allowing us to monitor its telemetry. This made it especially interesting when the fairing separated and the morning sunlight hit the satellite’s stowed solar arrays. Immediately, the telemetry showed that APEX’s batteries were being charged. We were able to confirm third-stage separation before contact was lost.



Figure 2-7. APEX and Pegasus Mated With B-52
(Photo courtesy Orbital Sciences Corp.)

The release from the B-52, the three stages of rocket firings, the satellite's lock-on to the sun, and the extension of its four deployable panels all occurred without problems. APEX made contact with the Indian Ocean ground station exactly as planned, 37 minutes after launch. The spacecraft was found to be functioning nominally. By the second contact, we began initializing the APEX subsystems and experiments.

The Pegasus booster placed APEX into a 70° inclination, 363 x 2552 km [196 x 1377 nautical mile (nmi)] orbit, agreeably satisfying PASP Plus's data-collection objectives. In fact, the higher apogee (2552 km instead of the originally baselined 1950 km) achieved by Pegasus allowed the satellite to traverse well into the earth's inner radiation belt. This let us accomplish the "array

power degradation vs. radiation” portion of the PASP Plus experiment in roughly half the time originally planned.

Later in the day of 3 August 1995, some intermittent APEX sun-sensor glitches put the spacecraft in a contingency mode and shut off the experiments. These anomalous readings continued for several contacts, and then ceased altogether. At this point, experiment operations were allowed to continue. Although experiment initialization was delayed about a day, the spacecraft was never in any danger and otherwise behaved exactly as expected. By 7 August 1994, all the experiments were completely initialized and collecting data. According to the operators at Onizuka AFB, this was one of the smoothest launch and early-orbit operations seen in years.

Operations continued smoothly until 4 November 1994, when a pressure sensor on one of the common pressure vessel batteries shorted out. The short corrupted all the temperature and pressure sensors (they were all multiplexed together) of the Battery Charge Regulator (BCR), fooling it into thinking the batteries were always fully charged and allowing only low current trickle charging. The immediate solution was to raise the trickle charge rate to a level that would provide enough power to run the spacecraft bus and heat the batteries to a safe level. This, however, did not provide enough power to allow the experiments to operate. Weeks later, some extremely limited experiment operations (I-V curves only) were performed, though only during sunlit portions of the orbit. In the mean time, Orbital Sciences Corp. (OSC) worked on new software code that would circumvent the BCR charging scheme and use bus voltage and battery cooling-plate temperatures to determine proper charging rates. Once implemented, APEX would be able to return to full experiment operations in sunlight and eclipse.

By mid-December, the new charging code was ready to be uploaded to the spacecraft. However, within several hours after the code was enabled, the spacecraft computer lost communications with other subsystems. The only recovery from this condition was a complete “reboot” of the spacecraft, which required the new code to be uploaded from the beginning, a three day process. After the code was reloaded, it was enabled and again the spacecraft computer lost communications and the spacecraft was “rebooted.” A third attempt produced the same result.

After reviewing the data, it was determined that each of the spacecraft computer glitches happened at apogee over the South Atlantic Anomaly (SAA). It also appeared to happen only when the PASP Plus controller was on. Based on this information, one explanation for these events is that radiation degradation of the spacecraft electronics lowered their resistance to electromagnetic interference (EMI). Possibly, the combination of some low-level noise from the PASP Plus controller and the increased radiation from passing through the SAA at or near apogee surpassed a threshold the spacecraft operating subsystems could no longer tolerate. Plans were developed to load the new charging code once again and then turn off the PASP Plus controller whenever the spacecraft passed over or near the SAA at higher altitudes (>1300 km). On 17 January 1995, APEX was once again fully operational, and PASP Plus operation was restored except for the SAA restriction.

Operations then continued smoothly in this state until 26 March 1995, when the spacecraft computer repeatedly lost communications with the BCR and turned off the experiments as a contingency. The spacecraft recovered from the communication losses by itself, but this reset some of the system default settings to values that applied to the original charging scheme, not the new charging code. Recovery required only reloading the correct default settings, but the communication problems continued to happen without explanation. The communication upsets coincided to a period of high space weather activity (K_p indices as high as 5 or 6) and generally happened during perigee passes over Antarctica. After 4 April 1995, these conditions cleared up and the problems ceased without ground intervention.

Another major anomaly happened on 16 May 1995. The satellite's Housekeeping Interface Unit (HIU) failed completely. The radiation to which APEX had been exposed was higher than expected for the *baselined* orbit (1950 km apogee instead of the actual 2552 km). The total dose expected after six months was exceeded in four. As a result, components such as the HIU degraded at a faster rate than originally anticipated. The loss of the HIU meant loss of the temperature and voltage data that the spacecraft computer used for the new battery charging code. Again, APEX could not adequately charge its batteries and had only enough power to support limited operations of the experiments during sunlight only.

To overcome this problem, OSC decided to make use of the battery-charging data APEX had amassed over nine months of on-orbit operation. Tables were developed to determine the right charging current for the batteries based on eclipse duration and power consumption of the experiments. The ground control team used these tables to command the spacecraft to charge itself at the correct rate at the correct time. This "open loop" charging is risky in that too low a charging rate could freeze the spacecraft batteries and damage them irreparably. Too high a charging rate could overheat the batteries and, again, damage them. Despite these risks, this method of battery charging allowed the experiments on APEX to operate at nearly 100 percent of their capability after 7 July 1995.

During "open loop" charging, the PASP Plus experiment was operated in an "out of memory" condition (APEX tried to maintain PASP Plus in its operating condition or, in the case of an interruption, return it to the same condition before the interruption). For example, in the event of a Controller current *over-limit* condition, power would be briefly interrupted, but then automatically re-applied, and the last command issued to the Controller would be re-sent, all without ground intervention. This automatic re-application of power and re-issuing of a bias command could happen many times (hundreds or even thousands) before the anomalous Controller condition (e.g., a high-voltage line "short") would be noticed on the ground. It was this "out of memory" operation of PASP Plus that prompted the 11 August 1995 "many times repeated" high-voltage over-current to cause the loss of further array I-V curve data.

After the 11 August 1995 failure of the PASP Plus Controller, the other APEX experiments, including the PASP Plus Dosimeter (on a separate line from the Controller), continued to operate. Starting in September 1995, APEX experienced problems with its dosimeter interrogator interface such that APEX could no longer telemeter data from the PASP Plus dosimeter. Because of the many previous APEX subsystem malfunctions and the software patches applied to keep APEX operating, for a while STP and OSC decided *not* to reboot the whole system, lest something else fail and the whole system go down. Finally, on 9 December 1995 a "firecode" reset was sent to APEX, re-enabling interrogator operation. Several 10-minute pieces of dosimeter data were successfully acquired over the next few days. On 14 December 1995, the PASP Plus Dosimeter was turned on and left on.

On 2 June 96, the APEX satellite experienced a catastrophic failure. Its attitude control electronics (ACE) failed; sun-sensor and magnetometer data were lost. The satellite tumbled, preventing solar array pointing, thereby draining the batteries. The loss of power precluded satellite systems functioning. All efforts to recover the spacecraft after this failure proved unsuccessful. On 11 June 1996, Det 2 (SMC/TEO) at Onizuka AFS decided that it would undertake no further effort to revive communication with the satellite.

2.3 PASP Plus Operations and Problems

The PASP Plus team undertook experiment commanding and *quick-look* data evaluation (using an on-site GSE) at the Satellite Control Facility at Onizuka AFB, CA. After turn-on and checkout of the PASP Plus instruments and some initial I-V curve taking, array biasing began on 7 August 1994. Data gathering involving the positive and negative biasing of the PASP Plus test arrays took place at various times over the period from 7 August 1994 to 11 August 1995, with several long gaps due to APEX subsystem problems.

PASP Plus biasing was halted by the APEX Battery Charge Regulator problem on 4 November 1995. After a thorough study, a software-patch fix was developed and tested by OSC and sent up to the satellite. PASP Plus operations were started again on 15 January 1995, and continued with various interruptions and operating-regime limitations (sunlight only, only at altitudes <1200 km when near the South Atlantic Anomaly, etc.) until 16 May 1995. Then, problems with other satellite subsystems and the time needed to find the appropriate fixes and PASP Plus operating-time limitations caused biasing operations to be halted from 17 May to 1 July 1995. Full PASP Plus operations, including biasing, continued from 1 July 1995 until 11 August 1995, when the over current (probably a short) in the high-voltage network of the PASP Plus controller resulted in the end of all biasing operations. Unfortunately, this also resulted in the end of I-V curve data gathering as well.

On 11 August 1995, after the PASP Plus controller experienced input current surges during positive biasing, it also began telemetering anomalous state of health [SOH] information (obviously erroneous voltage and temperature values). It was also not producing I-V curves, although it appeared to shift from one array to the next properly. After 11 August 1995, the

controller was no longer able to process analog-based data including those needed to produce test-array I-V curves. Direct digital data, such as those coming from the sun sensor or the TPM, were being properly processed; reasonable values were seen. The PASP Plus dosimeter (separately connected) was unaffected at that time and continued to supply radiation dose data.

The reason why the high-voltage biasing failure incapacitated the Controller's A/D converter, eliminating further taking of I-V curves, has been determined. Because of various APEX malfunctions that turned off the experiments, in August 1995 PASP Plus was operated in an "out-of-memory" condition. When the *over-current* due to the high-voltage failure occurred, power was briefly interrupted, but was then reapplied with PASP Plus still in the biasing mode. This re-application of power and resumption of biasing caused hundreds of high-voltage induced over-current pulses before the over-current caused power interruptions were noticed on the ground, and the high-voltage biasing stopped. These over-current pulses propagated into the A/D converter and eventually disabled it. The high-voltage biasing failure was a PASP Plus controller malfunction, but the loss of further I-V curves happened because PASP Plus was forced (because of APEX problems) to operate in the "out-of memory" mode.

Table 2-3 shows the data gathering periods for positive biasing, summarizing the voltage and plasma density ranges and the environmental and operating conditions encountered. Table 2-4 does the same for the negative biasing periods (Refs. 2-1, 2-2).

PASP Plus conducted comparative space-testing of many different kinds of solar arrays under a wide range of controlled conditions with a self-sufficient set of diagnostic sensors, so that the ways an array's performance is degraded can be fully correlated with the interactions of the space environment. By August 1995, PASP Plus had collected an order of magnitude more data about environmental interactions on solar arrays than all previous space-borne photovoltaic experiments combined.

Table 2-3. Data Collection Periods for Positive Biasing

| Biasing Period | Voltage Range | Plasma Density (cm^{-3}) | Environment and Operations Comments |
|--------------------|------------------|--|---|
| 7 Aug – 18 Aug 94 | +75 V to +500 V | $6 \times 10^3 \rightarrow 1 \times 10^5$ (2×10^5 rare) | Bias ± 20 min around perigee. Ram angle at perigee $\leq 90^\circ$ until 15 Aug. No eclipse over 7 to 17 Aug. All biasing in sunlight. Emitter on 1/3 of orbits after 11 Aug. |
| 10 Oct – 30 Oct 94 | +100 V to +300 V | $6 \times 10^2 \rightarrow 2 \times 10^5$ | Biasing around perigee. Ram angle at perigee $\geq 90^\circ$ and no eclipse for whole period. Emitter on about 1/3 of orbits. |
| 24 Oct – 30 Oct 94 | +100 V to +320 V | $4 \times 10^2 \rightarrow 2 \times 10^5$ | Biasing around the orbit. Ram angle at perigee $71^\circ \rightarrow 59^\circ$ for 24 to 30 Oct. No eclipse until after 28 Oct. Emitter not on. |
| 15 Jan – 17 Jan 95 | +75 V to +220 V | $2 \times 10^3 \rightarrow 6 \times 10^5$ | Biasing only in sunlight. Controller off for altitudes over 1200 km. Ram angle at perigee $106^\circ \rightarrow 97^\circ$. Emitter not on. |
| 12 Feb – 2 Mar 95 | +50 V to +220 V | $4 \times 10^2 \rightarrow 3 \times 10^5$ | Biasing 40 min before to 30 min after perigee, but off for altitudes over 1200 km when near SAA. No eclipse throughout period. Ram angle at perigee $64^\circ \rightarrow 96^\circ$. Emitter not on. |
| 27 Apr – 16 May 95 | +50 V to +430 V | $4 \times 10^2 \rightarrow 8 \times 10^2$ (1×10^2 rare) | Biasing around orbit, but off for altitudes > 1200 km when near SAA. Ram angle perigee $105^\circ \rightarrow 74^\circ$. Emitter not on. APEX problems! No biasing 17 May to 1 Jul. |
| 31 Jul – 11 Aug 95 | +50 V to +490 V | $2 \times 10^2 \rightarrow 3 \times 10^5$ | Biasing around orbit, but off for altitudes over 1200 km when near SAA. Ram angle at perigee $78^\circ \rightarrow 51^\circ$. Emitter not on. PASP+ controller problem 12 Aug! No more biasing. |

Table 2-4. Data Collection Periods for Negative Biasing

| Biasing Period | Voltage Range | Plasma Density (cm^{-3}) | Environment and Operations Comments |
|--|--------------------------------------|---|---|
| 22 Aug – 3 Sep 94 | –75 V to –450 V | $\leq 6 \times 10^2 \rightarrow 6 \times 10^5$ | No biasing in eclipse after 26 Aug. Higher negative voltages (–220V to –450V) only in sunlight. Unfavorable ram angles at perigee ($111^\circ \rightarrow 135^\circ$). TPM thresholds set at 0. |
| 17 Oct – 22 Oct 94 | –160 V to –400 V | $\leq 6 \times 10^2 \rightarrow 4 \times 10^5$ | No eclipse period in orbits. Ram angle at perigee is $\leq 90^\circ$ over 17 to 23 Oct ($88^\circ \rightarrow 73^\circ$). Arrays #2 and #1 are limited to –380V. TPM thresholds set at 0. |
| 31 Oct – 4 Nov 94 | –160 V to –370 V | $6 \times 10^2 \rightarrow 2 \times 10^5$ | Eclipses return on 29 Oct. Ram angle at perigee $57^\circ \rightarrow 53^\circ$ in period. Arrays #2 and #1 limited to –300V (orbits include eclipse). TPM threshold at 0. APEX problem 4 Nov! |
| 18 Jan – 11 Feb 95 | –280 V to –460 V | $6 \times 10^3 \rightarrow 6 \times 10^5$ (some higher over 18–20 Jan) | Biasing only <1200 km. For APEX safety, all Controller ops in sunlight until 4/5 Feb, then 10 min at end of eclipse. No significant eclipse measurements. Ram angle at perigee $95^\circ \rightarrow 64^\circ$. TPM threshold at 0 until 1 Feb, then set at 1. |
| 3 Mar – 26 Mar 95 30 Mar – 1 Apr 95 | –240 V to –430 V –240 V to –300 V | $6 \times 10^3 \rightarrow 8 \times 10^4$ | Bias 12 min before to 42 min after perigee; this includes all of eclipse. Ram angle is $\leq 90^\circ$ only past middle of eclipse. Ram angle at perigee $98^\circ \rightarrow 176^\circ$. TPM threshold set at 1. |
| 13 Apr – 8 Apr 95 | –240 V to –370 V | $6 \times 10^3 \rightarrow 3 \times 10^5$ | Bias 20 min before to 40 min after perigee; this includes all of eclipse. Ram angle is $\leq 90^\circ$ only past middle of eclipse. Ram angle at perigee $143^\circ \rightarrow 127^\circ$. TPM threshold set at 1. |
| 1 Jul – 18 Jul 95 | –300 V to –460 V | $2 \times 10^2 \rightarrow 4 \times 10^5$ | Biasing around orbit, but off for altitude over 1200 km when near SAA. Ram angle is $\leq 90^\circ$ only past middle of eclipse. Ram angle at perigee $135^\circ \rightarrow 109^\circ$. TPM threshold set at 1. |
| 19 Jul – 30 Jul 95 | –450 V to –500 V | $2 \times 10^2 \rightarrow 3 \times 10^5$ | Biasing around orbit, but off for altitude over 1200 km when near SAA. Ram angle is $\leq 90^\circ$ only past middle of eclipse. Ram angle at perigee is $109^\circ \rightarrow 80^\circ$. TPM threshold set at 1. |

From its August 1994 to August 1995 operations in space, PASP Plus collected a huge data base on environmental interactions (both space-plasma and space-radiation induced) on an extensive, representative collection of solar arrays. It has led to the full development of cause-and-effect relationships. The experiment allowed comparison of in-space measurements with analytic and computer-generated simulation models, with favorable results. This will lead to the use of these experimentally validated interaction codes to predict the performance of future solar arrays in particular space environments.

2.4 Results for the Other Experiments

CRUX/CREDO

Results from the CRUX/CREDO experiment greatly expanded the data available to experimenters. Other versions of the CRUX/CREDO experiment have previously flown on five Space Shuttle missions. But, because of the Shuttle's brief flight times and benign radiation environment, the data base of SEUs experienced was not large enough to be statistically significant—only about 100 total upsets. During the APEX mission, CRUX/CREDO is estimated to have recorded around one million upsets on the static random access memory (SRAM) parts under test. This wealth of new data from CRUX/CREDO directly aided in understanding SEUs and predicting upset behavior in microcircuits.

One of the important findings concerning SEUs that was made with CRUX/CREDO is the dominant effect that trapped protons can have on the upset behavior of SRAMs. (Refs. 2-3, 2-4). In the past, heavy ions dominated. But advances in technology employed in present microcircuits has increased the sensitivity of these devices to a point where vulnerability to protons trapped by the Van Allen belts dominates. In addition to SRAMs, CRUX/CREDO also flew power MOSFET test devices, and experienced the first burn-outs of these parts in space. (Ref. 2-5) Single event burnouts in SRAMs were also dominated by protons.

One of the most surprising findings from the CRUX/CREDO data was the device to device variation in SEU sensitivity within a part type. Even parts from the same mask set showed as much as a 15 to 1 variation in upset rates. Another surprising result was that 98 percent of the circuit burn-outs occurred at orbit locations with a dipole shell value of $L > 3$, even though these

locations accounted for only 60 percent of the time on-orbit. This also results from interactions with trapped protons.

FERRO

Unfortunately, an error in the FERRO experiment software that was not detected on the ground prevented the return of useful FERRO data. Since the purpose of this experiment was to measure the changes in properties of ferroelectric memories as they are fatigued, a limited amount of testing was done on the ground. This was to prevent the premature aging of the memories (before the start of the mission). However, limiting the experiment interface testing caused a software timing error to go undetected until the experiment was in orbit. Subsequent to the development of the FERRO experiment, new ferroelectric memory technologies have been developed that do not exhibit the fatigue degradation that was to be tested.

References for Chapter 2

- 2-1. D. A. Guidice and K. P. Ray, "PASP Plus Measurements of Space Plasma and Radiation Interactions on Solar Arrays," AIAA 96-0926, *34th Aerospace Sciences Meeting*, Reno, NV, 15-18 January 1996.
- 2-2. D. A. Guidice, H. B. Curtis, M. F Piszczor, and J. R. Palys, "Survey of Experimental Results from One Year of PASP Plus Orbital Operation," AIAA 96-2331, *27th AIAA Plasmadynamics and Lasers Conference*, New Orleans, LA, 17-20 June 1996.
- 2-3. Adolphsen, J., *et al.*, "Single Event Upset Rates on 1 Mbit and 256Kbit Memories: CRUX Experiment on APEX," *IEEE Transactions on Nuclear Science*, Dec. 1995.
- 2-4. Adolphsen, J., *et al.*, "SEU Data From the APEX Cosmic Ray Upset Experiment: Predicting the Performance of Commercial Devices In Space," *IEEE Transactions on Nuclear Science*, June 1996.
- 2-5. Adolphsen, J., Barth, J., and Gee, G. B., "First Observations of Proton Induced Burn-Outs of Power MOSFETS in Space: The CRUX Experiment on APEX," *IEEE Transactions on Nuclear Science*, (to be published).

Chapter 3 Instrumentation

D. A. Guidice and P. S. Severance, Phillips Laboratory, Hanscom AFB

The PASP Plus experiment consists of four kinds of equipment:

- a. a set of test arrays, some of which are divided into biased and unbiased modules.
- b. experiment-control instrumentation capable of creating *array* or *spacecraft* conditions under which measurable environmental interactions occur.
- c. interactions-measuring instrumentation that quantify what happens when the ambient or created conditions impact the performance of the test arrays.
- d. diagnostic sensors to measure the ambient environmental conditions affecting array performance (Ref. 3-1).

3.1 Test Arrays

To maximize the scope of the investigation, a variety of conventional and advanced-concept solar arrays were included in the array complement. As shown in Table 3-1, twelve different solar arrays were investigated on PASP Plus. Other than Array 0,1,2 (basic silicon, which serves as a standard), array selection was based on the array's availability (at no cost to the experiment) and its possible use on future DoD or NASA space missions.

A very detailed description of the PASP Plus test arrays, including cell and array mechanical configurations and color photographs, is given in a report by Adams (Ref. 3-2).

Four different silicon (Si) solar cells were flown. Referring to Table 3-1, the first Si array (0,1,2) is comprised of 2 x 4 cm, 8-mil thick standard Si solar cells, conventional interconnects, and fused silica coverglass. These cells are representative of many DoD and NASA solar array designs that have flown in the past and are still flown today. The array contains three electrically isolated modules. Module 0 was *not* high-voltage biased. It serves as a benchmark for comparison with the *biased* Module 1 (same area, number and kind of cells, etc.) for investigating whether or not high-voltage operation (biasing) affects an array's susceptibility to radiation. For the two biased modules, Module 2 has three times the surface area (three times the

Table 3-1. PASP Plus Solar Arrays

| Module No. | Cell/Array Type | Number of Cells | Cell Size (cm x cm) | Array Developer |
|--------------|---------------------------|-----------------|---------------------|-----------------|
| 0,1,2 | Si (Std) 8 mil | 20, 20, 60 | 2 x 4 | RCA / WL |
| 3 | Si 8 mil, wtc [Space Sta] | 4 | 8 x 8 | Lockheed |
| 5 | Si 2.2 mil [APSA] | 12 | 2.6 x 5.1 | TRW/JPL |
| 9 | Amorphous Si//Si | 1 | 4 x 4 | TRW |
| 4,6 | GaAs on Ge 3.5 mil | 20, 12 | 4 x 4 | ASEC |
| 8 | GaAs on Ge 7 mil, wtc | 4 | 4 x 4 | Spectrolab |
| 11 | GaAs on Ge 7 mil | 8 | 4 x 4 | Spectrolab |
| 7 | AlGaAs//GaAs | 20 | 0.7 x 0.7 | VS Corp. |
| 10 | InP 12 mil | 10 | 2 x 2 | Spire/NRL |
| 12,13 | GaAs//CuInSe ₂ | 9, 3 | 2 x 2, 2 x 4 | Boeing |
| 14 | GaAs Mini-Cass | 8 | Concentrator | TRW |
| 15 | GaAs//GaSb Mini-Dome | 12 | Concentrator | Boeing |

wtc = wrap-through connectors

// = multi-junction cells

bold = biased

number of cells) of Module 1. This difference was used to examine the relationship between high-voltage induced effects (leakage current and arc rate) and module area.

The second Si solar array (Module 3) is comprised of 8 x 8 cm cells, 8-mil thick, with wrap-through connectors. These are baselined to provide power for the International Space Station (ISS). The flexible wrap-through connector design is expected to reduce cell laydown manufacturing costs and decrease its susceptibility to space-plasma effects when operating at high voltage. This array was biased to determine how the cell's isolated wrap-through contact design influences its high-voltage performance.

The third Si-cell Array (Module 5) is the Advanced Photovoltaic Solar Array (APSA), which emphasizes light weight. The array consists of 2.6 x 5.1 cm, 2.2-mil thick Si cells bonded to a flexible substrate. APSA holds great promise for high specific power applications (≥ 130 W/kg).

The APSA module was biased to demonstrate its operation in the space plasma, but biasing was limited to +300 V and -300 V.

A 4 x 4 cm thin-film amorphous Si array (Module 9) was also tested on PASP Plus, but was not biased. With its low cost, this type of array may have some applications in space if its radiation resistance is satisfactory. However, amorphous Si has the problems of low efficiency and susceptibility to the Stabler-Wronski solar-UV deterioration effect.

The next three arrays listed in Table 3-1 utilize GaAs on Ge solar cells. These arrays represent an important technology that offers higher conversion efficiency and higher radiation resistance over Si-cell arrays.

The first of the three PASP Plus GaAs on Ge arrays is comprised of 4 x 4 cm, 3.5-mil thick solar cells. This array has two separate modules (4 and 6) with conventional interconnects and ceria-doped (CMX) coverglasss. Both modules, which have different cell areas, were biased.

The next GaAs on Ge array (Module 8) consists of 4 x 4 cm, 7-mil thick cells with CMX coverglasss. The performance of this array can be compared with the final GaAs on Ge array (Module 11), which is identical in solar cell material and array substrate; however, 8 has wrap-through connectors instead of the conventional interconnects of 11 and 8 has one-half the number of cells. The wrap-through connectors have good prospects for improved high-voltage operation due to the "concealed" interconnects. Both of these GaAs on Ge arrays (Modules 8 and 11) were high-voltage biased.

The next three arrays in Table 3-1 (AlGaAs//GaAs, InP, and GaAs//CuInSe₂) were not high-voltage biased, but their performance was measured as a function of exposure to the natural space environment and orbital temperature excursions. All array strings were laid down with conventional interconnects and coverglass. The InP solar cell is important because of its moderately high conversion efficiency and very high radiation resistance. The GaAs//CuInSe₂ solar-cell array has dual-junction mechanically stacked cells. The AlGaAs//GaAs solar-cell array has dual-junction monolithic cells.

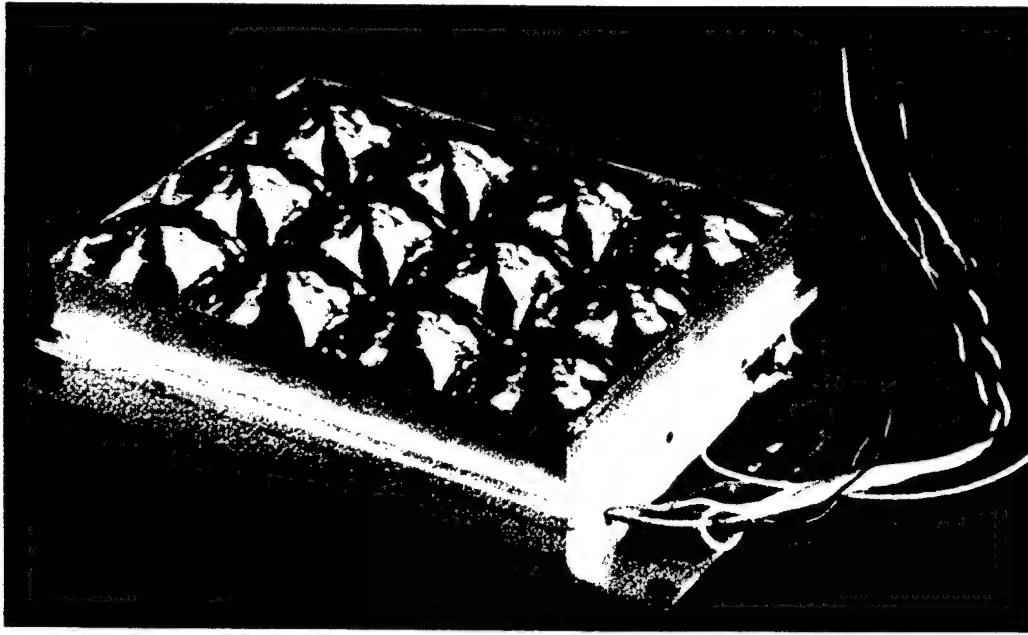


Figure 3-1. Mini-Dome Concentrator Array with GaAs//GaSb Multi-Junction Solar Cells.

Both of the multi-junction arrays have high conversion efficiencies and good radiation resistance. Since the photovoltaically generated voltages from the two parts of a dual-junction cell are quite different, their outputs are matched (connected in the array) in a non-unity ratio (as much as 3:1). An important aspect of PASP Plus's radiation degradation investigation is to see whether radiation causes significant "mismatching" losses in these kinds of arrays.

The last two solar arrays shown in Table 3-1 are concentrator designs. The first is the Mini-Cassegrainian array, whose eight cells each focuses (concentrates) sunlight, using metallic reflecting mirrors, onto a very small GaAs solar cell mounted to the bottom of the primary mirror. The second concentrator array (Mini-Dome) has 12 fresnel-lens focused units with GaAs//GaSb as the mechanically-stacked dual-junction cell. This array with its prismatic coverglass and GaAs//GaSb cells features high conversion efficiency. Concentrator designs are important for their potential high voltage use since the small solar cells are isolated from the space plasma environment by the concentrating elements and the array support structure. A photo of the Mini-Dome concentrator array is shown in Figure 3-1.

3.2 Experiment Control Instrumentation

Controller: The instrument that governs the operation of the experiment is the PASP Plus controller built by Amptek. Its principal functions include:

- a. Receiving commands from the APEX satellite (which receives many of the commands from the ground stations) and distributing them to interaction measuring units and diagnostics sensors whose commands and telemetry go through the controller.
- b. Collecting scientific and "housekeeping" data from the interaction measuring units and diagnostic sensors and sending the data to the APEX satellite, which in turn sends them to the ground stations in the form of real time data and (mainly) data dumps.
- c. Producing a 64-point I-V curve for each of the 16 array modules according to programmed sequences. The short-circuit current (I_{sc}) and open circuit voltage (V_{oc}) are measured first; then a programmable active MOSFET load sets the load resistance at 62 predefined in-between values, and module current and voltage (at each point) is measured. The I-V curve measurement is completed in two seconds; current and voltage are measured with 12-bit resolution.
- d. Applying positive and negative biasing voltages to each or any of the ten biased modules for 23 seconds (out of 30) in four 30-sec intervals (two minutes total) in predefined sequences. The biasing ranges are 50 to 500 V, positive or negative (as commanded). The voltage resolution is 4 V (3.92 V, to be exact), with a precision of 0.5 V. There are seven preprogrammed sequences of bias voltages in the four 30-sec intervals of the two-minute bias period, one of which is all zeros (no bias), and one programmable sequence allowing any four available values (3.92 V resolution) within the 50 to 500 V range. The biases (either positive or negative) are applied so as to be additive to the module's generated voltage (although in most of the biasing measurements the module's generated voltage was short-circuited). The controller also continually measures the physical (thermal) temperatures of the twelve arrays.

Emitter: PASP Plus also has an additional experiment-control device: an electron emitter. It produces a stream of *outgoing* electrons to help balance the *incoming* flow of electrons. For positive biasing, the charge balance of the satellite produces negative potential contours around the vehicle. These contours limit PASP Plus's ability to simulate realistically the high positive voltage operation of a large functional array. The use of an electron emitter could eliminate the

negative potential contours and improve the simulation. However, in the course of our on-orbit measurements, it was found that the emitter, when it was on (only during positive biasing), interferes with the Langmuir Probe measurements of plasma density, which are essential to the leakage current investigation.

3.3 Interactions Measuring Instrumentation

Electrometer: The electrometer (a wide dynamic range ammeter) located within the controller was used to measure the leakage current from the space plasma. It measured leakage current in two linear ranges from 0.2 mA to 20 mA with a resolution of 0.2 mA. However, for low leakage currents in sunlight (in the order of a few microamperes or less), sunlight-generated photoelectrons enter into the electrometer measurements, adding to the plasma leakage current measured. For leakage currents greater than a few microamperes, photoelectron current is negligible.

Transient Pulse Monitor (TPM): The TPM consists of an electronics box (central processing unit), four electromagnetic transient sensors (E-field sensors for detection of radiated pulses) and a current-loop sensor (for detection of power-line arc pulses) wrapped around the high-voltage line inside the PASP Plus controller. The TPM measures the properties (amplitude, derivative, integral) of the largest pulse in each one-second interval and the number of pulses (up to 15) in that one-second interval. It was used to obtain the arc rate and characteristics of arc-discharge pulses that occur during negative biasing of the test arrays.

3.4 Diagnostic Sensors

Sun Sensor: A sun incidence-angle sensor measures the angles (in two orthogonal axes) between the normal to the panel surface and the direction to the center of the sun. The PASP Plus sun sensor, mounted on the deployed payload panel, measures the alignment of this panel (and its test arrays) to the incident solar energy. The APEX sun sensor, mounted on the payload shelf between the Mini-Cassegrainian and Mini-Dome concentrators, is used to *control* the alignment of the payload-shelf normal (central axis) to the center of the sun by means of APEX's attitude

control system. To meet PASP Plus requirements for its concentrator arrays, the APEX satellite, while in sunlight, had to point its payload-shelf axis to within $\pm 0.5^\circ$ of the center of the sun.

Langmuir Probe: The Langmuir probe measures low-energy plasma parameters (density and temperature) of the space environment in front of the PASP Plus arrays. To sweep the appropriate voltage range with respect to the space plasma, the PASP Plus Langmuir probe was equipped with a SENPOT (potential sensor), capable of sensing how far negative the satellite frame-ground is below space-plasma reference and compensating for this deviation up to about -30 V. The vehicle-frame negative potential is due to the fact that APEX's spacecraft-power solar arrays are configured (like all space vehicles) with its positive terminal high (around +30 V) and the negative terminal connected to vehicle frame-ground. The positive (high) end of power arrays goes to only 20 to 25 V positive with respect to the space plasma while the vehicle frame-ground goes to 10 to 5 V negative (how far depends on the amount of metal surface area there is on APEX to collect the positive ions needed to balance the electrons coming to the power arrays). The Langmuir probe does not make measurements during the application of high-voltage bias (either positive or negative) on the PASP Plus test arrays. When biasing is taking place, the Langmuir probe makes its measurements during the 7 seconds of the 30-sec biasing interval when bias voltage is not applied.

Electrostatic Analyzer (ESA): The ESA measures the energetic-particle density (of electrons and positive ions separately) in 20 logarithmically spaced bins over the energy range of 30 eV to 30 keV. The ESA uses a rapidly stepped high-voltage electric field across curved microchannel plates (electric centripetal force balances the particle's kinetic centrifugal force) to guide the charged particles to the channeltron amplifiers and detectors. By stepping the cross-guide voltage, the ESA obtains the (energy) spectral distribution of the energetic charged particles in the 30 eV to 30 keV range. The ESA can be used to detect the passage of APEX through an enhanced auroral region. In addition, the lower-energy portion (from 30 to 200 eV) of the ion spectrum can be used to determine the negative potential of the satellite during high-voltage positive biasing. When the satellite frame is at a certain negative potential, the thermal (< 0.3 eV) ions coming to the satellite (and the aperture of the ESA) are accelerated to an energy (in eV) corresponding to the satellite negative potential (in Volts). For higher bias voltages ($> +300$ V) on

the larger arrays and high plasma densities ($>3 \times 10^{10} \text{ m}^{-3}$), the ESA detected ion peaks as high as 95 eV.

Contamination Monitors: Contamination monitors are used to give an indication of the amount of effluents deposited on array surfaces (this leads to decreased sunlight collection and array output power (as measured by the I-V curves). PASP Plus contamination sensors included two QCMs (quartz crystal microbalances) and three calorimeters. The information from these monitors could allow us to differentiate the solar-array power-output degradation caused by radiation-dosage damage from any caused by effluent deposition. The QCMs measure the mass of material deposited on the QCM's surface disk from the change in its internal oscillator frequency. The deposited mass/area is given roughly by: $m (\text{g/cm}^2) = 1.6 \times 10^{-9} \Delta f$ (in Hz). Over one year, the Δf measured was about 1500 Hz, so material contamination is not considered significant. The calorimeters' surfaces have materials similar to the coverglasses of some of the test arrays. By monitoring their temperatures, we could see if there has been any change in the absorption-to-emission (α/ϵ) ratio. A trifling examination of calorimeter data did not reveal any evidence of significant coverglass darkening.

Dosimeter: The PASP Plus radiation dosimeter is used to measure the high-energy particle flux and dose from protons and electrons that lead to degradation in solar-array power output. It has a separate interface (power, command, telemetry) with the APEX satellite; it is not controlled by the PASP Plus controller. Its design has three hemispheric domes of varying thickness for higher energy particles ($\geq 20 \text{ MeV}$ protons) and a thinner flat disk (for structural reasons) to measure the lower energy protons ($\geq 5 \text{ MeV}$) mainly responsible for radiation damage in solar cells. Table 3-2 gives some of its detection characteristics. A photo of the PASP Plus dosimeter, built by Panametrics, Inc. is given in Figure 3-2.

Table 3-2. Dome Thickness and Electron and Proton Energy Ranges for the PASP Plus Dosimeter

| Aluminum Shields | | | Electron Threshold (MeV) | Proton Energy (MeV) |
|------------------|------------------------------|------------|-----------------------------|------------------------|
| Dome | Density (g/cm ²) | Shape | | |
| D1 | 0.0294 | Flat | 0.15 | 5-80 |
| D2 | 0.55 | Hemisphere | 1.0 | 20-115 |
| D3 | 1.55 | Hemisphere | 2.5 | 32-120 |

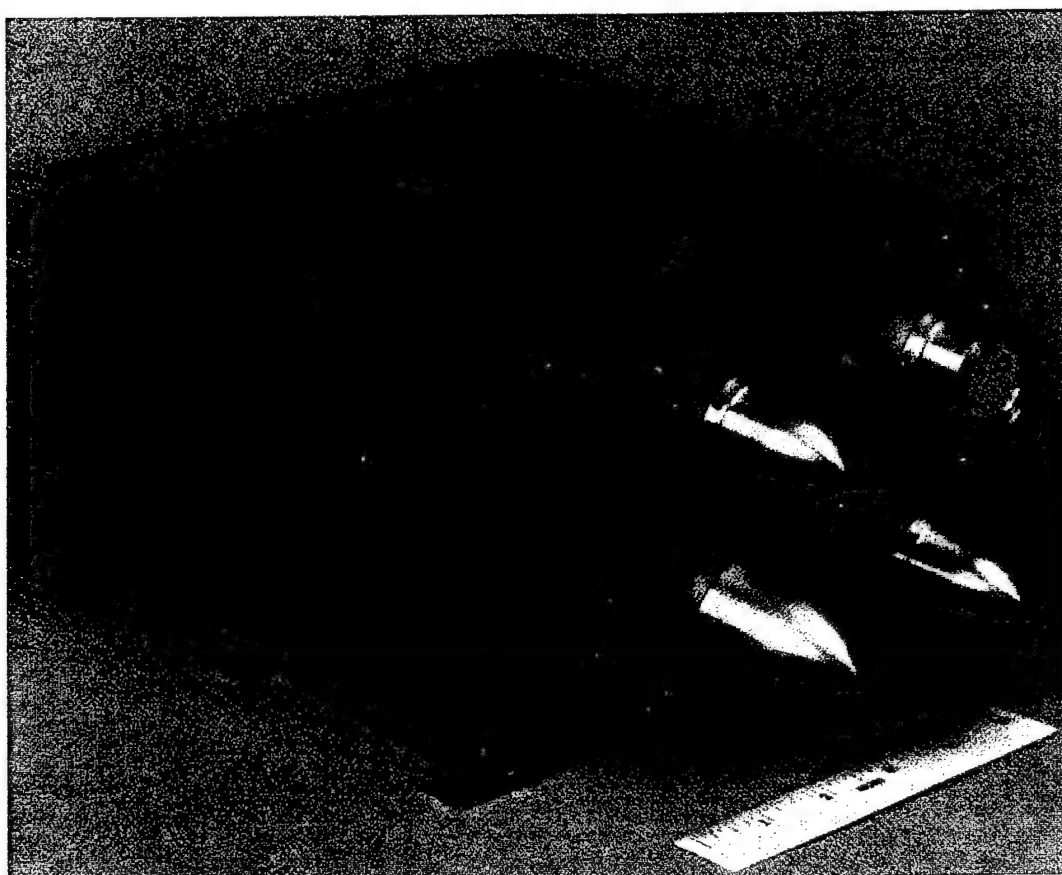


Figure 3-2. PASP Plus dosimeter with four shield thicknesses (one thin disk and three thicker domes) used for measuring flux and dose of energetic electrons and protons in four energy ranges.

References for Chapter 3

- 3-1. Guidice, D., Severance, P., Curtis, H., and Piszczor, M., "Investigation of Space-Environment Effects on Photovoltaic Technologies by the PASP Plus Experiment," AIAA paper 95-0371, *33rd Aerospace Sciences Meeting*, Reno Nevada, 9-12 January 1995.
- 3-2. Adams, S.F., "Photovoltaic Array Space Power Plus Diagnostics Flight Experiment: Pre-Flight Description of Experimental Photovoltaic Modules," WL-TR-92-2080, Wright Laboratory, October 1992.

Chapter 4

Radiation Degradation

D. C. Marvin, Aerospace Corporation
H. B. Curtis, NASA/Lewis Research Center

The two principal objectives of the PASP Plus experiment are to study the degradation of the solar cell modules in the trapped electron and proton environment and to observe the current leakage and arcing effects during high voltage biasing. This chapter focuses on the former objective. The radiation effects are studied by collecting complete current-voltage (I-V) characteristics (and the associated temperature) of each module, and observing the degradation in properties such as short circuit current (I_{sc}), open circuit voltage (V_{oc}), maximum power (P_{max}), and fill factor (FF). Complete I-V data were obtained for approximately one year before failure of the experiment. The low altitude of this mission resulted in significant earth albedo contributions to the solar cell output at most times of year. The data are difficult to correct for this highly variable effect, and no attempt has been made in this regard on the data presented here. However, at the end of this section are several examples of "clear view data." These are selected data points that coincide with times when the experiment has no view of the earth and therefore no albedo contribution. The usual corrections have been made for seasonal variations in earth-sun distance and temperature. No angle of incidence corrections were needed since sun sensor data showed that the spacecraft maintained sun-pointing attitude to within 1 degree at all times.

The layout of the experiment modules is illustrated in Figure 4-1. Modules 8 through 15 were mounted on the payload shelf and therefore had the mass of the spacecraft providing backside shielding. The other modules were mounted on one of the deployed panels, which provided approximately 30 mils of equivalent shielding. In general the modules on the deployed panel were mounted on samples of aluminum honeycomb for handling, which contributed an additional 30 mils of equivalent shielding. Thus, the backside shielding of most modules on the deployed panel is taken to be 60 mils fused silica equivalent (FS). Modules 3 and 5 were exceptions to this layout; these solar cells were mounted on Kapton blankets for use without a rigid substrate. In order to accurately represent their performance in this type of array, a cutout was made in the

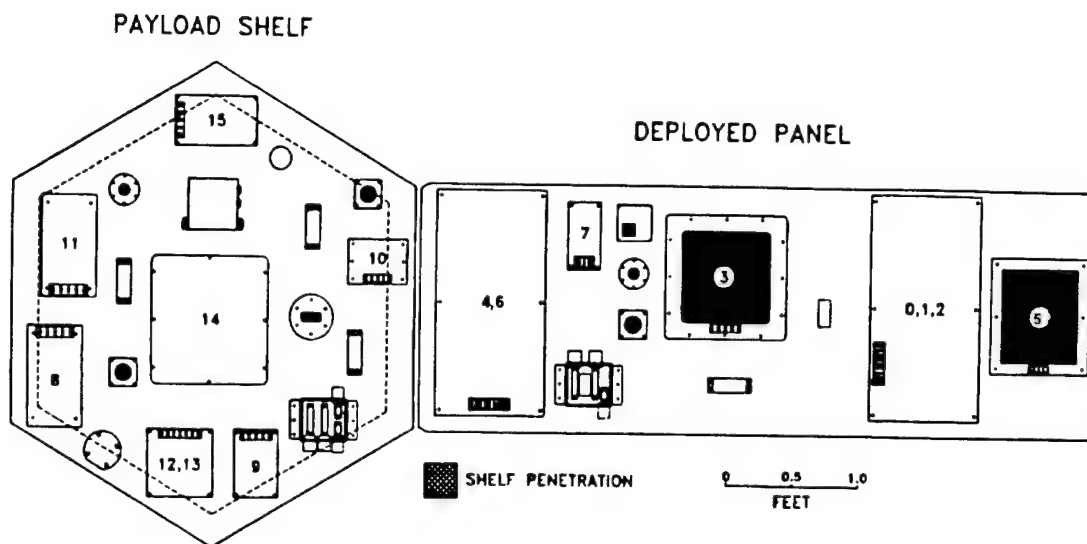


Figure 4-1. Location of solar cell modules on APEX spacecraft using module numbers.

deployed panel beneath these two modules. The backside radiation shielding is therefore calculated with only the blanket contribution, which typically amounts to the equivalent of 2 to 4 mils of fused silica.

It is clearly an approximation to divide the backside shielding of modules into only two primary groups, those on the deployed panel with finite shielding assumed and those on the payload shelf with infinite shielding assumed. Modules near the boundary of these structures experience some spacecraft shielding, but not over the entire 2π steradian backside. This approximation is acceptable because the amount of radiation entering the front of the cells through the coverglasses exceeds that entering the back of the cells through even 60 mils FS by a factor of four or more in most cases. Thus the accuracy of the predictions depends primarily on the front side shielding.

The observed degradation in the solar cell parameters is compared with behavior predicted using the methodology discussed in Reference 4-1. This procedure uses the NASA trapped particle models (AP-8 and AE-8) and ground measurements of solar cell behavior under 1 MeV electron irradiation. The radiation environment for the APEX orbit was derived from these models using ephemeris software developed at The Aerospace Corporation and verified using Space Radiation for Windows (Ref. 4-2). The equivalent 1 MeV electron exposures were obtained using the

EQFLUX computer code from JPL. The response of each solar cell type to 1 MeV electron irradiation in ground measurements was obtained from Reference 4-1 for silicon cells and from the polynomials developed by Anspaugh (Ref. 4-3) for GaAs. The data on silicon cells were generally fit to within 1 percent absolute (i.e., they reproduce an observed degradation factor of, say, 0.85 to within ± 0.01) with a two-parameter equation of the form

$$X/X_0 = 1 - a \times \log_{10}(1 + F/b) \quad (4-1)$$

where X can be any of the solar cell parameters I_{sc} , V_{oc} , or P_{max} , a and b are parameters, and F is the number of 1 MeV electrons/cm². This equation is not suitable for use with GaAs solar cells and so polynomials were used. The disadvantage of the polynomials is that they are ill-behaved outside the range $10^{12} \text{ cm}^{-2} < F < 10^{16} \text{ cm}^{-2}$ of fluence values F .

4.1 Experiment Results

A key issue for advanced solar cells is obtaining accurate solar simulators to assess their performance. Therefore, an important part of any space experiment is the opportunity to compare ground and space data on such cells. It is desirable to obtain the first flight data as early as possible, before any degradation effects have occurred. Figure 4-2 compares the ground P_{max} data for all of the functioning modules with space data taken in the first few hours of the APEX mission. It shows that for most modules the agreement is within 3 percent, which should be considered quite good. The exceptions are the amorphous silicon module (Module 9), which is approximately 9 percent low on-orbit, and the indium phosphide module (Module 10), which is 5 percent low on-orbit. There is no ready explanation for the discrepancy in these two cases.

The remaining figures in this section compare the predicted degradation in solar cell maximum power with the actual flight data. Similar plots of V_{oc} , I_{sc} , and FF have been prepared but are not presented here except in cases where further discussion of unexpected results is needed. Complete I-V curves are also available. The predictions are referred to in the figure legends as "pre-flight predicts" because they are normalized to the pre-flight ground measurements and use radiation degradation predictions to generate the time development of the performance. The actual flight data consist of five day averages (except in cases where five days of contiguous data

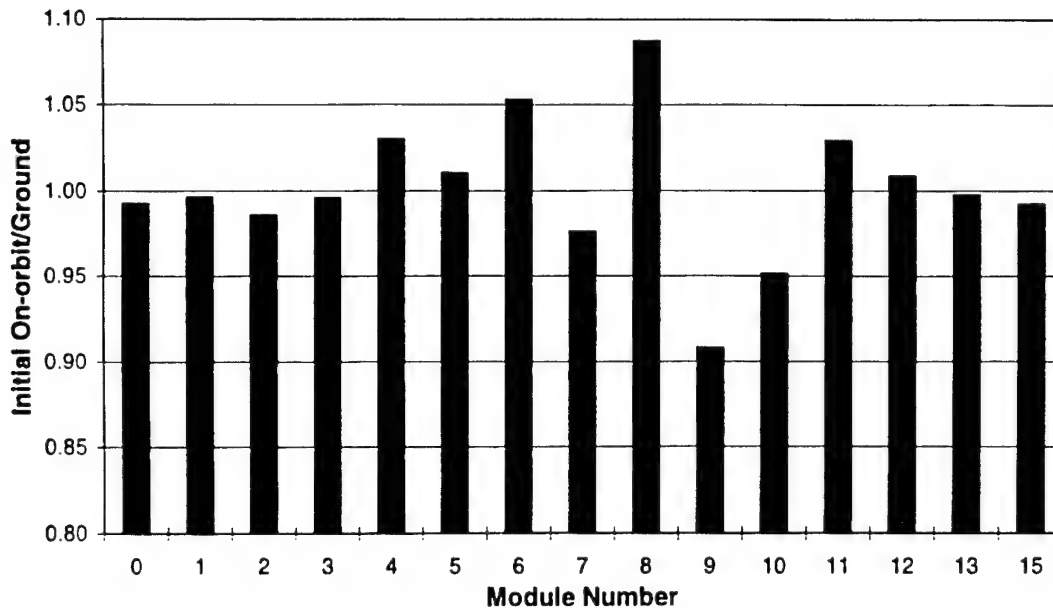


Figure 4-2. Ratio of initial on-orbit power to ground-measured power for each functioning module.

are not available, e.g., during the period of flight anomalies discussed elsewhere in this report), which have been adjusted for solar intensity and temperature. The mini-Cassegrainian concentrator experiment failed early in the mission and no useful data were obtained.

Silicon Solar Cells

Modules 0,1 and 2 contain identical silicon solar cells wired in series strings as described in Table 4-1. The pre-flight circuit efficiencies are 13.9, 13.8 and 13.8 percent. The Pmax flight data in Figure 4-3 indicate that much less degradation occurred than predicted. Although not presented here, the flight data for Isc and Voc show that both parameters degraded less than predicted, i.e., the behavior of Pmax is not due solely to a discrepancy in current or voltage. Assuming that the radiation environment description is not in error, the possible causes of this disagreement are incorrect shielding specification or incorrect cell description. On the former issue, Figure 4-5 in Reference 4-4 shows a cross section of Modules 0,1 and 2 that specifies a 6-mil-thick-fused silica (FS) coverglass and 1 mil of adhesive on top of the cells. The value of 6 mils FS effective shielding listed in Table 4-1 was used for the radiation predictions, since the adhesive contributes at most 0.5 mils additional shielding due to its low density. The statement referring to 8 mil coverglass on Page 15 of Reference 4-4 is a typographical error. A front

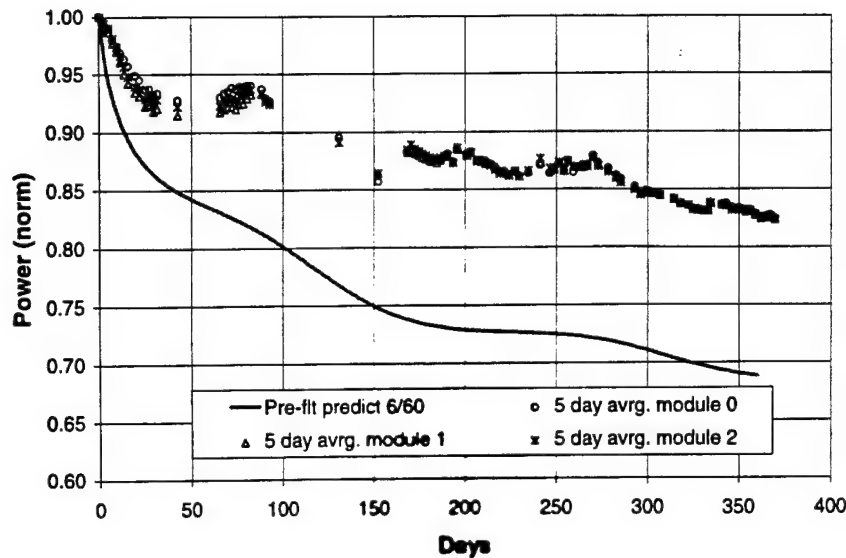


Figure 4-3. Power degradation in Modules 0, 1, and 2, showing much less degradation than expected.

shielding thickness on the order of 50 mils FS would be required to cause agreement between the observed power degradation and the prediction.

The backside shielding has been taken to be 60 mils FS since there are two substrates under the solar cells; an experiment substrate consisting of 0.5 inch aluminum honeycomb with two 10 mil graphite/epoxy face sheets, and the actual deployed wing substrate, which consists of 0.5 inch honeycomb with 11 mil aluminum facesheets. With respect to cell description, it is certain that these are n/p back surface field/reflector silicon cells (BSFR) manufactured by Spectrolab. The only uncertainty is whether the back surface field is produced by boron or aluminum doping. These cells were procured by RCA in 1984, and no documentation exists that contains a precise description. In this analysis it has been assumed that they are boron doped by the following reasoning: Reference 4-1 provides averaged beginning of life (BOL) performance data on both cell types (Figures 3.90 and 3.92). These data are compared with the BOL ground data on Module 0 in Table 4-2. Clearly the data for boron-doped BSFR cells matches the Module 0 data more closely. It might be argued that the match is too close, given that losses are present in the 20 cell string that constitutes Module 0, and that the aluminum-doped cells parameters provide needed margin to produce the observed string performance. However, if the module were fabricated using above-average cells, then this extra margin would be available even in the

Table 4-1. Summary Description of PASP Plus Modules

| Module # | Solar Cell Size, Type and Thickness | Coverglass Thickness | Configuration | Front/Rear Shielding Used in Prediction (mils FS) |
|----------|-------------------------------------|----------------------|------------------|---|
| 0 | 2x4 cm BSFR Si (8 mil) | 6 mil FS | 20 series | 6/60 |
| 1 | 2x4 cm BSFR Si (8 mil) | 6 mil FS | 20 series | 6/60 |
| 2 | 2x4 cm BSFR Si (8 mil) | 6 mil FS | 60 series | 6/60 |
| 3 | 8x8 cm WT Si (8 mil) | 5 mil CMX | 4 series | 7.4/5 |
| 4 | 4x4 cm GaAs/Ge (3.5 mil) | 4 mil CMX | 5sx4p | 5.7/60 |
| 5 | 2.6x5.1 cm BSFR (2.2 mil) | 2 mil CMX | 12 series | 3/3 |
| 6 | 4x4 cm GaAs/Ge (3.5 mil) | 4 mil CMX | 4sx3p | 5.7/60 |
| 7 | 0.5 cm ² AlGaAs/GaAs | 24 mil FS | 4sx5p | 24/60 |
| 8 | 4x4 cm GaAs/Ge WT (7 mil) | 6 mil CMX | 4 series | 7.8/60 |
| 9 | 4x4 cm Amorphous Si | 20 mil CMX | 1 series | 26/60 |
| 10 | 2x2 cm InP (12 mil) | 6 mil FS | 10 series | 6.5/∞ |
| 11 | 4x4 cm GaAs/Ge (7 mil) | 6 mil CMX | 4sx2p | 7.8/60 |
| 12 | 2x2 cm GaAs/CIS | 2 mil CMX | 9 series, 3:1 VM | 3.4/∞ |
| 13 | 2x4 cm GaAs/CIS | 2 mil CMX | 3 series, 4:1 VM | 3.4/∞ |
| 14 | Minicassegrainian GaAs/Ge | | 8 series | |
| 15 | Minidome GaAs/GaSb | ≈ 90 mil FS | 4sx3p | 90/∞ |

BSFR = back surface field and reflector

FS = fused silica

CMX = ceria-doped borosilicate glass

WT = wrap through contacts

VM = voltage matched configuration

boron-doped devices. A definitive statement cannot be made without knowing the specifications of each cell used for the module. If the prediction in Figure 4-2 were to assume the aluminum-doped cells, the curve would show $P/P_0 \approx 0.655$ at 360 days instead of the 0.685 shown, creating an even larger discrepancy with the flight data.

The wrap-through contact BSFR silicon cells in Module 3 are the Space Station design mounted on Kapton blankets. The pre-flight circuit efficiency is not available, but the BOL efficiency derived from the first 5 hours of flight is 12.2 percent. The 5 mil CMX coverglass combined with

Table 4-2. Comparison of Module 0 Cell Performance With Two Types of BSFR Cells

| | Module 0 | Boron BSFR | Al BSFR |
|----------------------------|----------|------------|---------|
| Isc (mA/cm ²) | 40.6 | 40.8 | 42.5 |
| Pmax (mW/cm ²) | 19.1 | 19.0 | 19.9 |

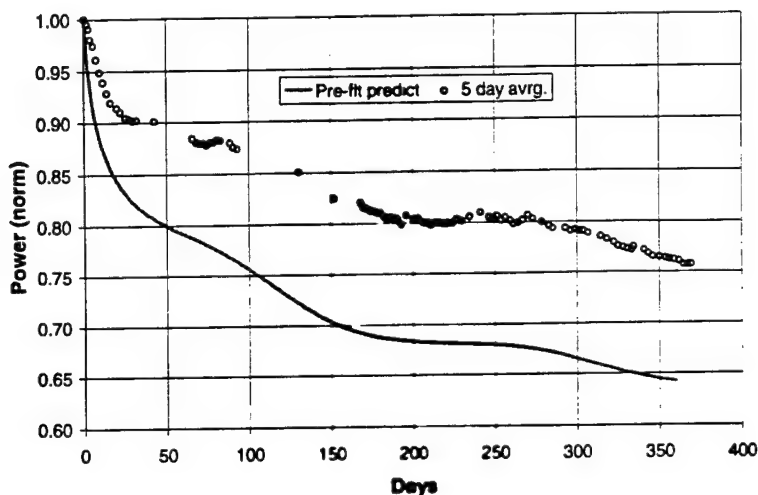


Figure 4-4. Power degradation for Module 3 comprised of Space Station cells, showing significantly less degradation than predicted.

3 mils of adhesive results in the front shielding equivalent to 7.4 mils FS shown in Table 4-1. The rear shielding calculation is complex due to the presence of copper traces in the Kapton blanket, and to the absence of a dominant rigid substrate. The 5 mil FS value was provided by NASA (Ref. 4-5). The predicted degradation for these cells shown in Figure 4-4 is greater than for the similar cells in Modules 0, 1 and 2 due primarily to this reduced shielding. The observed degradation in this module is also much less than predicted.

The cells in Module 5 are from the Advanced Photovoltaic Solar Array (APSA) program, with a pre-flight circuit efficiency of 12.0 percent. The assembly is very similar to the Space Station blanket except that the solar cells are only 2.5 mils thick and the coverglass is 2 mil CMX. The effective shielding properties of this assembly are also from Reference 4-5. Figure 4-5 compares the predicted degradation in Pmax and the flight data. These cells are predicted to degrade the least of any of the silicon cells in spite of the thin shielding, due to the improved radiation

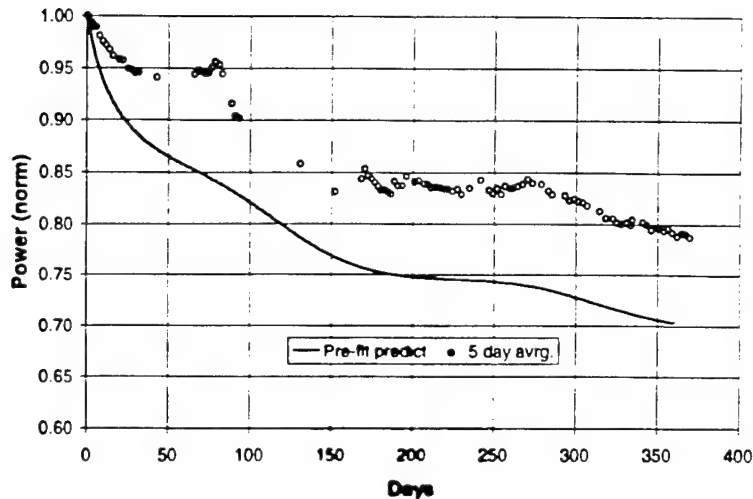


Figure 4-5 Module 5 containing APSA blanket shows less degradation than predicted.

resistance of very thin cells. As with the other silicon cells, the degradation is much less than predicted.

Gallium Arsenide and Related Cells

Modules 4 and 6 contain circuits of identical GaAs/Ge solar cells, with pre-flight circuit efficiencies of 18.6 percent and 17.5 percent respectively. Figure 4-6 shows that the observed degradation in Pmax agrees reasonably well with the prediction. The improved radiation resistance of GaAs cells as compared with silicon cells is clearly apparent from a comparison with Figures 4-2 through 4-5.

Modules 8 and 11 consist of GaAs/Ge solar cells with 7 mil substrates, and pre-flight circuit efficiencies of 15.4 percent and 18.5 percent respectively. The cells in the former have wrap-through contacts similar in concept to the space station cells in Module 3. Some loss in efficiency occurred during integration of the module and so 15.4 percent is not representative of the technology's capability. The degradation of both modules shown in Figure 4-7 follows the prediction reasonably well, and is slightly less than for Modules 4 and 6 due to the thicker coverglass used.

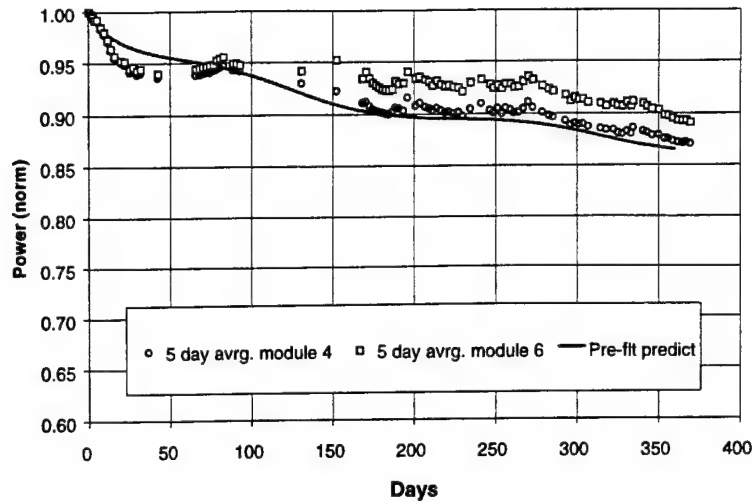


Figure 4-6. Module 4 and 6 data on gallium arsenide solar cells with 3.5 mil germanium substrates.

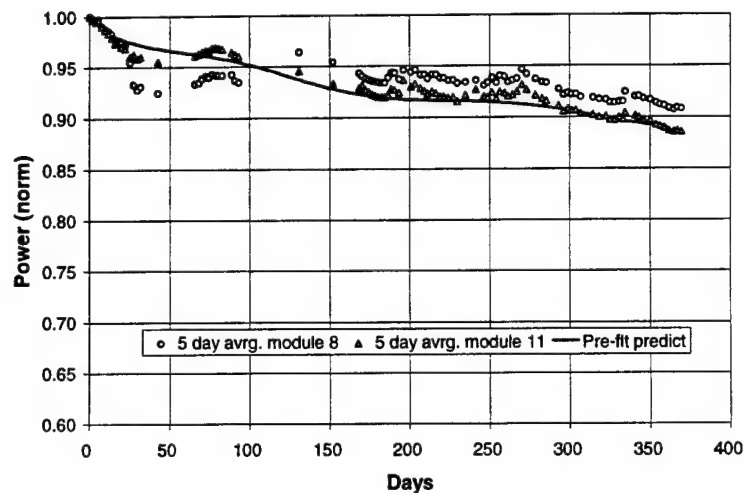


Figure 4-7. Module 8 GaAs/Ge solar cells have wrap-through contacts and Module 11 cells have conventional contacts. Both are on 7 mil Ge substrates.

Module 7 is a circuit of monolithic AlGaAs/GaAs tandem solar cells with a pre-flight efficiency of 17.9 percent. The prediction shown in Figure 4-8 is based on degradation of the GaAs cell only, since no radiation data on AlGaAs cells of this type are available. However, the limited data on other AlGaAs cells suggests that degradation of the GaAs dominates the behavior of the tandem. The flight data show a more rapid initial degradation than expected, but for the majority of the mission the degradation is as predicted. At the end of one year, the deviation from the

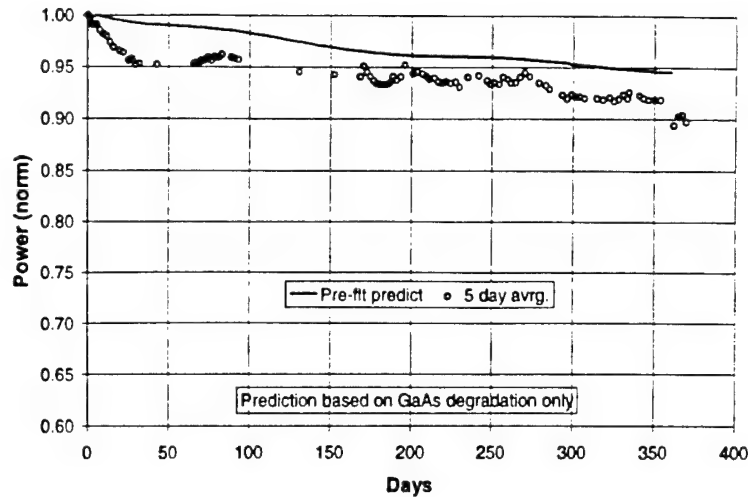


Figure 4-8. Power degradation of tandem AlGaAs/GaAs cell circuit.

model is only 3 percent. From the beginning of the mission, the I-V curves from this module exhibited a slight kink at approximately 1.0 V that was not present in the ground data. No detailed modeling has been performed to determine the possible causes. The use of thick coverglasses on this module is responsible for the limited amount of degradation and prevents an accurate assessment of the degradation occurring in the individual junctions of the tandems.

Modules 12 and 13 contain tandem gallium arsenide/copper indium diselenide circuits with pre-flight efficiencies of 17.3 percent and 18.3 percent respectively. Module 12 uses a voltage matched wiring configuration, in which the nine CIS cells are connected in series and then connected in parallel with three GaAs circuits of three cells each. This arrangement is expected to minimize difficulties with end of life current matching between the two cell types. Module 13 uses a similar concept, except with three parallel circuits of four CIS cells in parallel with three GaAs cells. The behavior of these two modules is very similar as shown in Figure 4-9. The radiation degradation is significantly less than predicted. Limited information on the radiation resistance of CIS cells (Ref. 4-6) indicates that virtually no degradation is expected at these exposures and therefore the prediction is based solely on GaAs degradation. However, these GaAs cells differ from all others in the PASP experiment in that they have a thinner emitter (0.2 microns vs. 0.5 microns), and reverse polarity (n/p vs. p/n). The complexity of the voltage matched circuit configuration makes significant additional analysis necessary in order to conclude that these cell differences are responsible for the unexpectedly good performance.

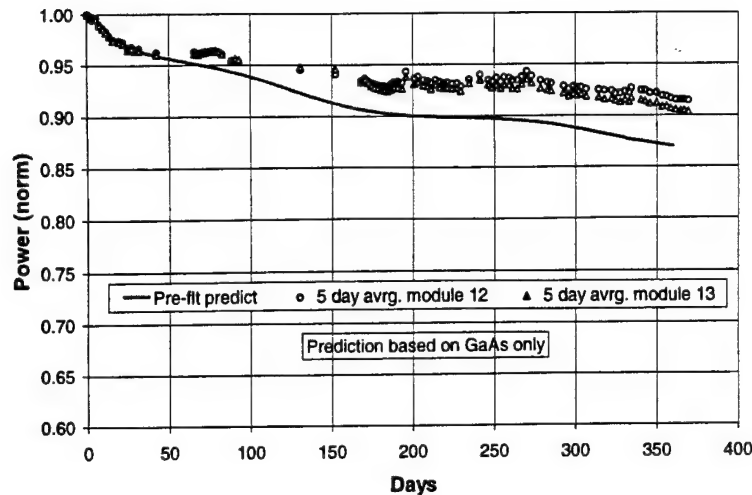


Figure 4-9. Power degradation for two voltage matched GaAs/CIS circuits, showing better than predicted radiation tolerance.

The power degradation of the indium phosphide (InP) circuit in Module 10, which had a BOL efficiency of 18.3 percent, is shown in Figure 4-10. InP has been investigated over the years because of its resistance to radiation damage, and this property is evident in these data. The only module that degraded less than InP is a concentrator module with heavy shielding, and therefore it may be said that InP is (not unexpectedly) the most radiation resistant cell type in the PASP Plus experiment. Unlike most of the other modules, however, the initial flight data show a significant discrepancy with the ground data. The power output from the flight data is 5 percent lower than the ground measurement, and no cause has been identified. The predicted degradation of this cell agrees reasonably well with the flight data, however there is a significant uncertainty in this prediction. The damage equivalence of energetic electrons and protons in InP has not been thoroughly investigated for the cells in this module and therefore the parameters for GaAs were used, as has been the standard practice.

The data on the amorphous silicon array is shown in Figure 4-11. In order to properly represent the data in this figure, it shows absolute power rather than normalized power. Amorphous silicon has been demonstrated to be quite resistant to radiation degradation. and when this feature is considered along with the 20 mil CMX coverglass supplied on Module 9, no radiation degradation is expected in this experiment. However, the light induced degradation known as the Stabler-Wronski effect (S-W) is quite significant. Figure 4-11 shows the flight data for power, a

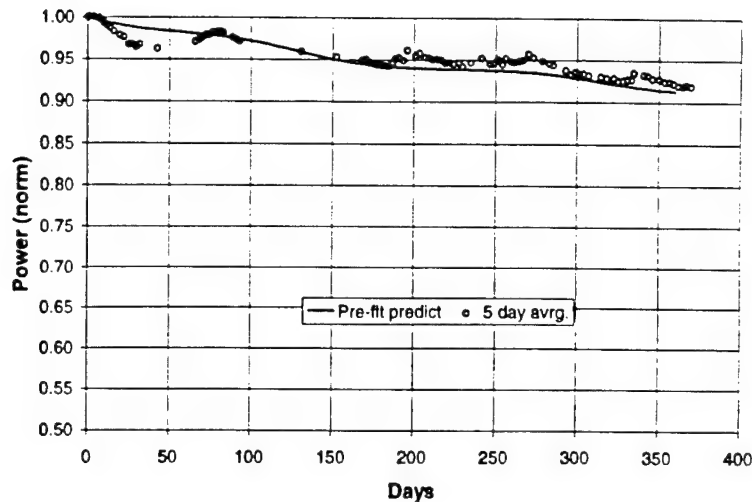


Figure 4-10. Power degradation of indium phosphide module.

few points from Reference 4-7 showing the measured S-W effect on cells similar to these, and a prediction based on this observed after normalization to the BOL efficiency of these modules. The experimental S-W data in Reference 4-7 are obtained from accelerated UV exposure tests, and Figure 4-11 shows that the 50 percent degradation found in these data is quite consistent with the flight data. It should be mentioned that refinements to the amorphous silicon cell structure have been made in the past five years that greatly reduce the S-W effect.

The mini-dome refractive concentrator, Module 15, was built by Boeing using GaAs/GaSb multijunction solar cells and ENTECH lenses. In contrast to the situation with all other modules, it was not possible to obtain good ground measurements of module I-V characteristic and temperature coefficients. Thus, the data shown in Figure 4-12 are corrected for temperature using coefficients determined from data taken at various temperatures during the first few days of flight. The shielding calculation is more complicated than for planar modules due to the presence of the curved dome and fused silica secondary lens shown in Figure 4-13 (Figure 19 in Reference 4-4 shows an earlier version of the concentrator assembly that was not flown). If these two components were planar, they would contribute shielding equivalent to 9 mils and 80 mils of fused silica respectively. The simplifying assumption was made that the total effective planar shielding was 90 mils of silica. Figure 4-12 shows that the power degraded significantly faster than predicted for this amount of shielding, and Figure 4-14 shows that the primary reason is extra loss in I_{sc} . This suggests that the power loss is not due to extra radiation damage in the cell

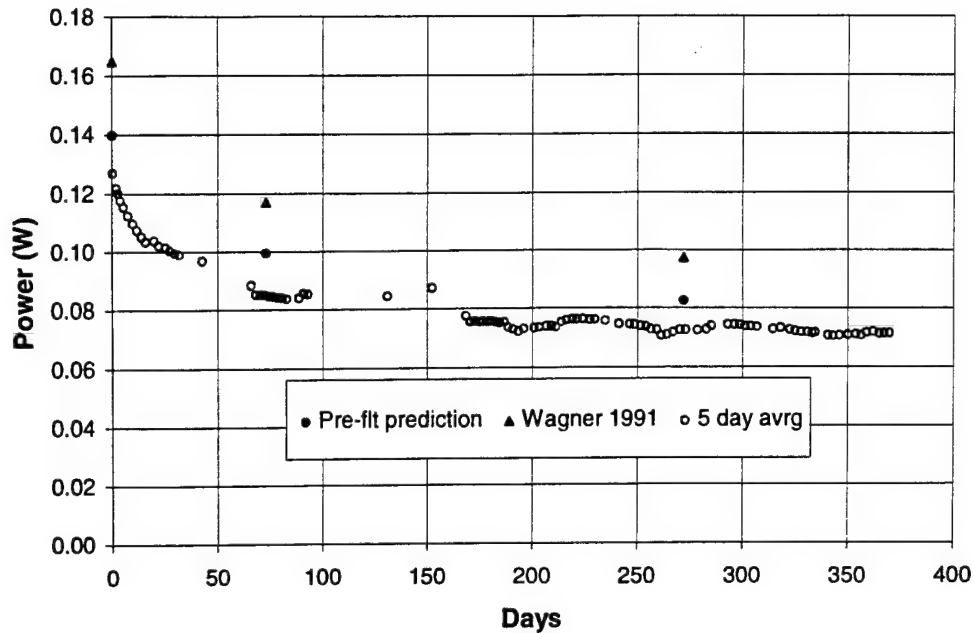


Figure 4-11. Amorphous silicon array power performance compared with pre-flight prediction based on light-induced degradation losses only (no radiation effects).

(since Voc would then show extra loss as well), but perhaps to radiation-induced darkening of either the dome or the secondary lens. Some darkening does occur in fused silica, but it is normally not measurable in sample thicknesses typical of solar cell coverglasses (3–12 mils). However, it might be observed in a much thicker sample such as the 80 mil secondary. The linear characteristic of the degradation is also suggestive of darkening rather than radiation degradation, which usually exhibits an asymptotic behavior.

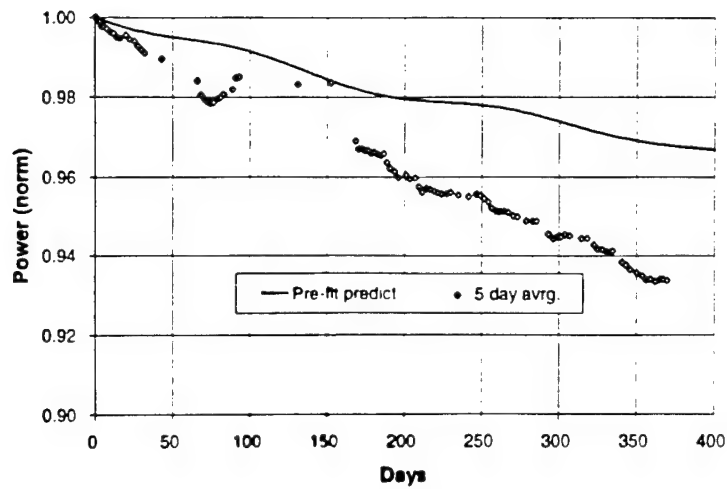


Figure 4-12. Power degradation of GaAs/GaSb concentrator array significantly exceeds prediction

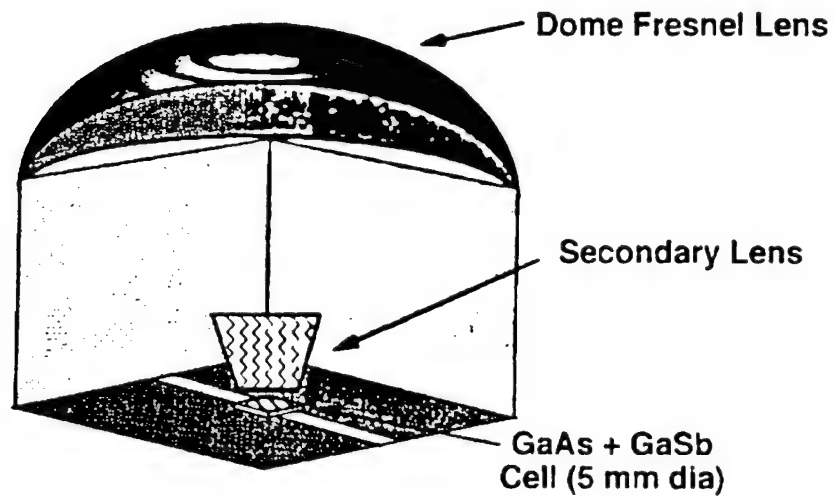


Figure 4-13. Schematic of Module 15 Minidome optical assembly. The secondary lens assembly is not shown to scale.

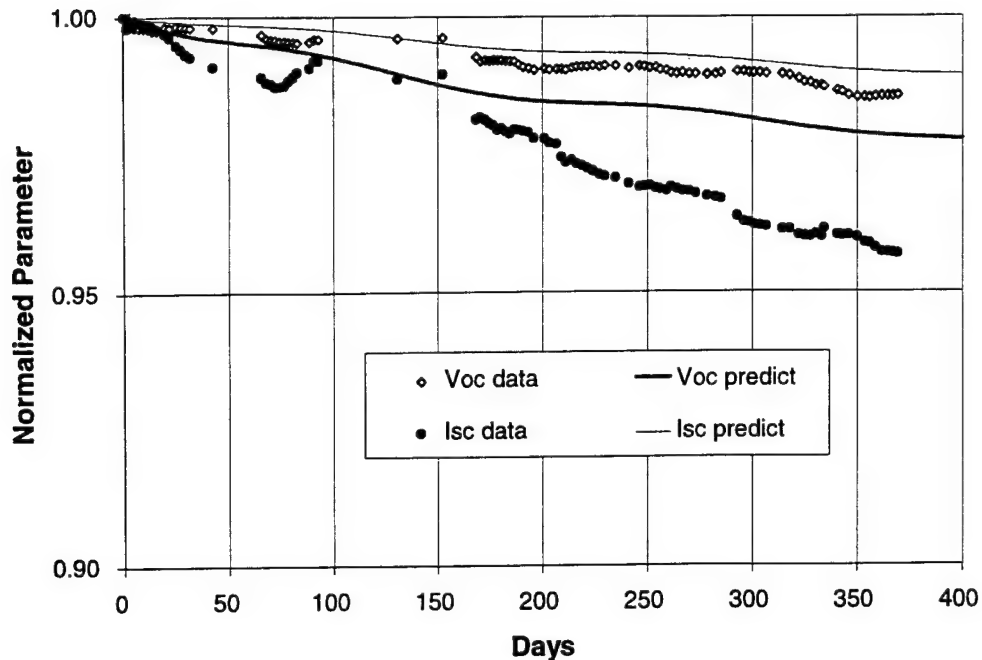


Figure 4-14. Current and voltage degradation of GaAs/GaSb concentrator array, showing that current degradation greatly exceeds prediction, while voltage degradation is reasonably consistent with prediction.

Figures 4-15 and 4-16 show clear view data, along with the five-day averages shown previously, for Modules 0 and 4. The scales are expanded compared with the preceding figures to show detail. The clear view data are only available at certain times of year. At those times the agreement with the five-day average data is reasonably good and a smooth curve could be drawn through all of the clear view data. The excursions, or “bumps” of the five-day average data occur at the other times of year, indicating significant contamination of the data by albedo effects. In contrast with the two planar array cases, Figure 4-17 shows that the concentrator array does not exhibit large excursions. This is due to the limited acceptance angle of the concentrator optics, which excludes most of the wide field albedo light.

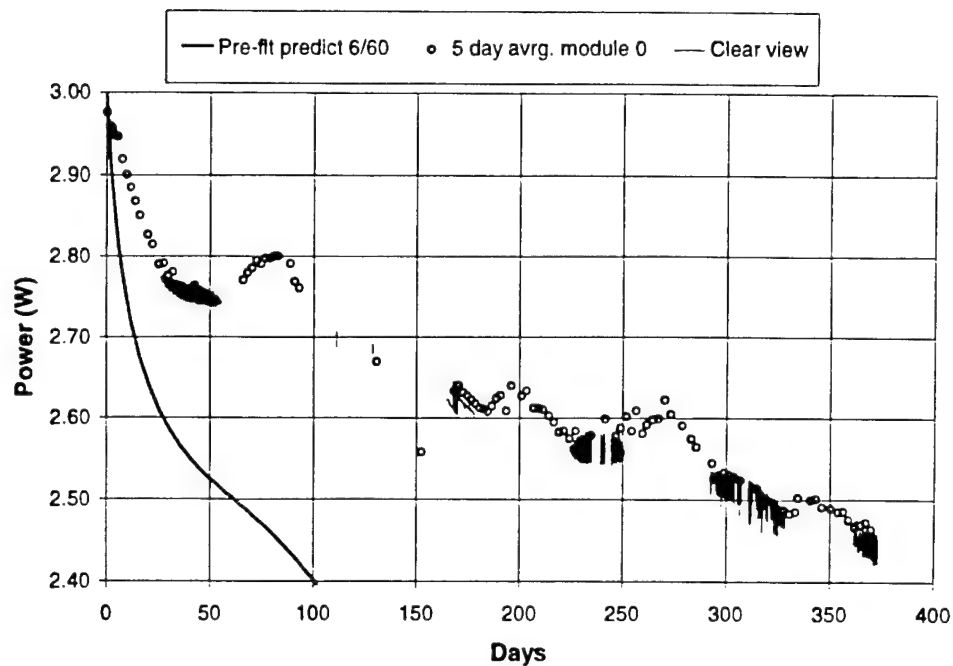


Figure 4-15. Clear view data and five-day average data for silicon Module 0.

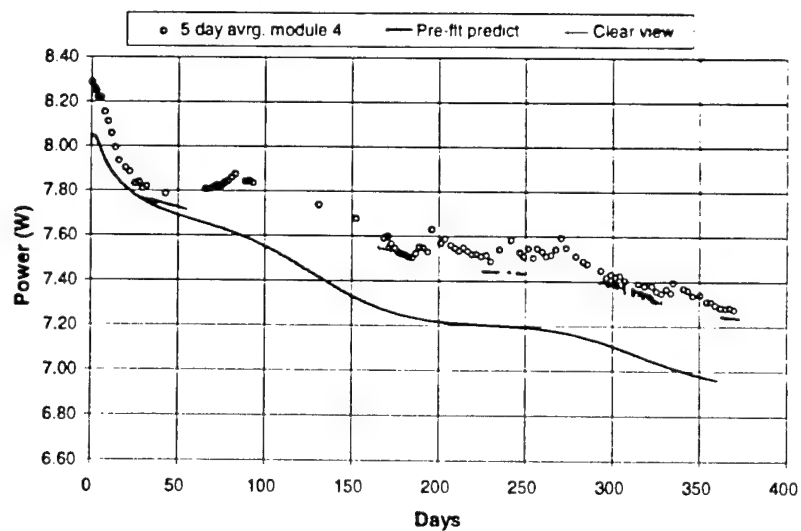


Figure 4-16. Clear view data and five-day average data for GaAs Module 4.

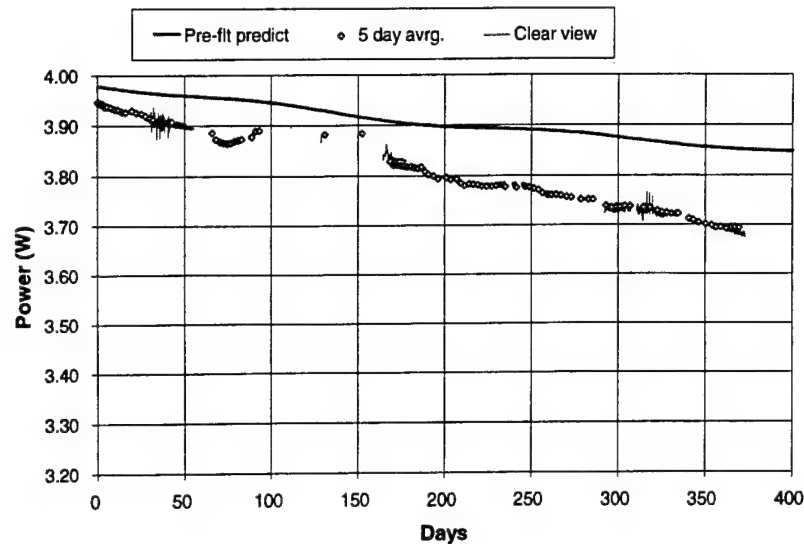


Figure 4-17. Clear view and five-day average data for concentrator Module 15.

4.2 Conclusions

The PASP Plus experiment has returned approximately one year of reliable data from a medium radiation orbit. Agreement between the ground measurements of module power and the earliest flight data is within about two percent for all modules except the indium phosphide and amorphous silicon. All of the silicon solar cell modules have degraded much less than predicted by radiation models, and no convincing explanation has been found for this. The degradation of all other modules is in good agreement (within three percent) with the corresponding predictions.

References for Chapter 4

- 4-1. H.Y. Tada, *et al.*, *Solar Cell Radiation Handbook*, JPL Publication 82-69, 1982.
- 4-2. Copyright Severn Communications Corporation
- 4-3. Personal Communication, Dr. Bruce Anspaugh.
- 4-4. S.F. Adams, "Photovoltaic Array Space Power Plus Diagnostics Flight Experiment: Pre-Flight Description of Experimental Photovoltaic Modules," WL-TR-92-2080, October 1992; H. Curtis, *et al.*, "Early Results from the PASP Plus Flight Experiment," *First World Conference on Photovoltaic Energy Conversion*, pp. 2169-2172, 1994.

- 4-5. Personal Communication, Mr. Michael Piszczor, NASA Lewis Research Center.
- 4-6. R. Mueller and B. Anspaugh, "Technology Readiness in Thin Film Solar Cells," PL-TR-93-1002, May 1993.
- 4-7. S. Wagner, *et al.*, "Performance and Modeling of Amorphous Silicon Solar Cells Soaked at High Light Intensity," Proc. 22nd IEEE Photovoltaic Specialists Conference, pp. 1307, 1991.

Chapter 5

Arc Rate Predictions and Flight Data Analysis for the PASP Plus Experiment

J. D. Soldi, Massachusetts Institute of Technology
D. E. Hastings, Space Power and Propulsion Laboratory

During large negative voltage operation, arc discharges occur. Here arcing is defined as a sudden current pulse up to the order of an ampere on a timescale of a microsecond or less. The current pulse is often accompanied by a spot of light at the edge of the coverglass. Arcing can result in electromagnetic interference, solar cell damage, induced currents in the power system, optical emissions, and an enhanced local plasma density. The PASP Plus experiment biased a set of advanced solar arrays to high negative voltages to examine their arcing characteristics. This chapter describes the results of this experiment.

5.1 Arcing Onset Model

An arcing onset model was used to simulate the PASP Plus experiment. Figure 5-1 shows the solar cell model system used in the simulations. This arcing model is based on the work of Cho and Hastings (Ref. 5-1).

The arc initiation process consists of a series of steps shown in Figure 5-2 and described below.

1. Ambient ions charge the dielectric (i.e. coverglass and adhesive) front surface, but leave the side surface uncharged.
2. As the front surface potential approaches zero relative to the plasma, a strong electric field of $E=V/d$ (where V is the bias voltage and d is the dielectric thickness) is formed at the conductor (interconnect) surface, inducing

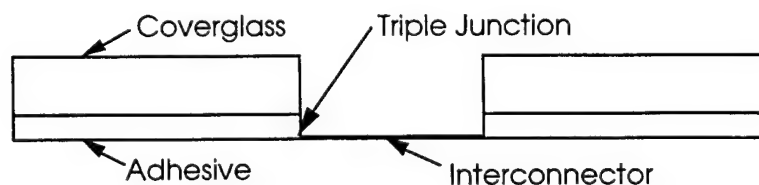


Figure 5-1. Solar cell model system.

pre-breakdown electron emission due to enhanced electron emission (EFEE) from emission sites on the conductor. Electrons are also released due to ion induced emission from ion bombardment of the conductor surface.

3. Some of the emitted electrons strike the dielectric side surface, inducing the release of secondary electrons and causing electron stimulated desorption of neutrals adsorbed on the dielectric surface. If the secondary electron yield is greater than unity, the side surface charges up positively, providing a positive feedback mechanism to further enhance the electric field at the conductor surface.
4. As the electric field increases, the electron emission increases until it is limited by the negative space charge of the emitted electrons.
5. Once the desorbed neutral density becomes high enough, ionization begins due to collisions between electrons and neutrals.
6. If the neutral density is very high, Townsend breakdown occurs. Even if the density is not high enough for Townsend breakdown to occur, breakdown is still possible if the positive ion space charge can cancel the negative electron space charge and enhance the field at the conductor.
7. The arcing time is the minimum of the sum of the ion and EFEE charging times for all the emission sites.
8. A discharge wave created by the arc resets the charging process at all of the emission sites within the area covered by the wave.

This model was developed through the use of computer particle simulations of the arc initiation process. These results were then used to develop analytic formulas for the ion charging time τ_{ion} and the enhanced field electron emission charging time τ_{efec} . The ion charging time is given by

$$\tau_{ion} = \frac{\left[V_e - \left(V_a - \frac{\Delta Q}{C_{front}} \right) \right] C_{front}}{en_e v_{ion} A_{cell}} \quad (5-1)$$

where V_a is the potential difference between the coverglass front surface and the interconnect when the previous arc occurred, V_e is the potential of the current arc, ΔQ is the coverglass

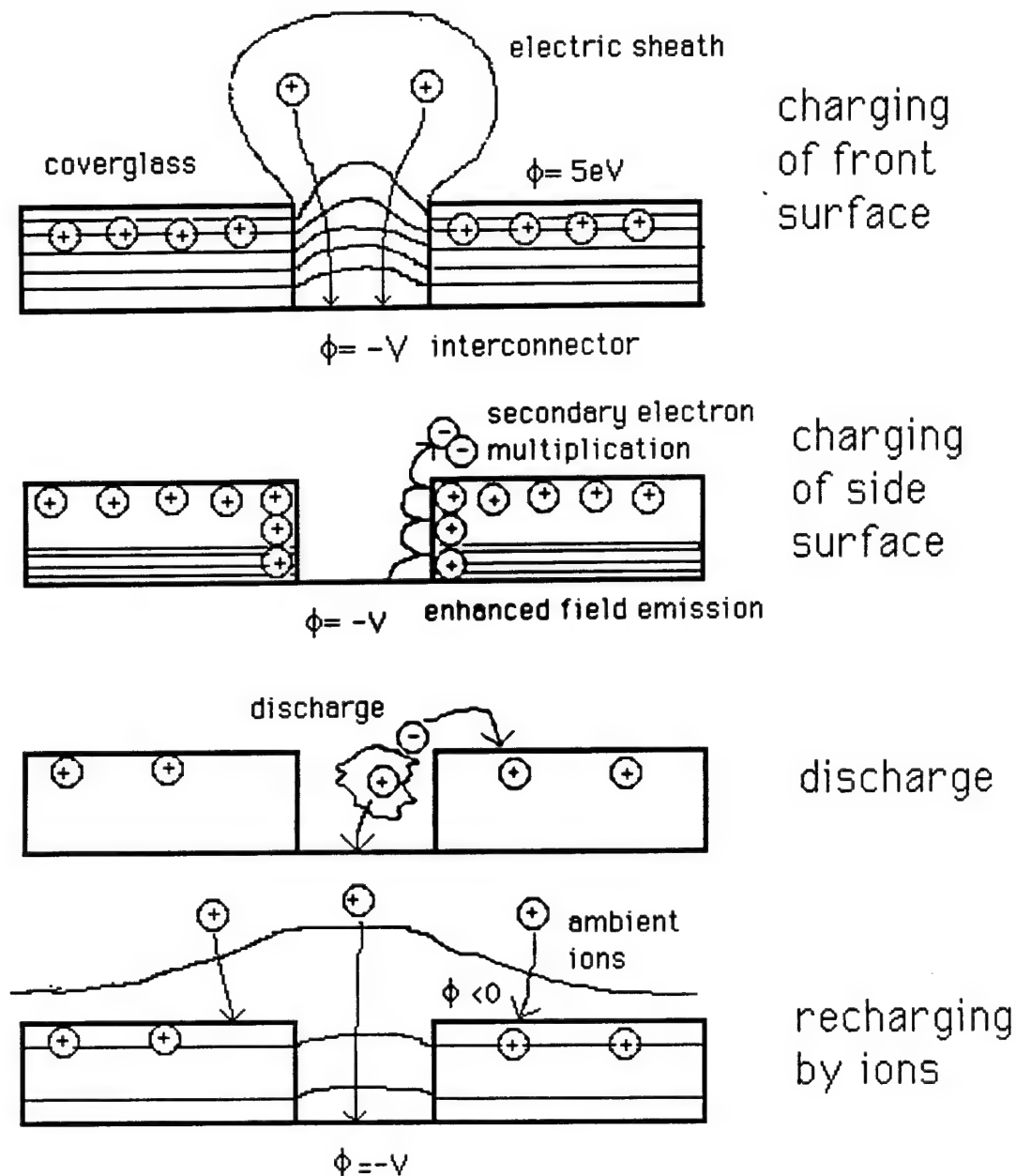


Figure 5-2. Arc initiation process.

surface charge lost from the previous arc, C_{front} is the capacitance of the front surface, e is the electron charge, n_e is the plasma density, v_{ion} is the ion velocity, and A_{cell} is the front surface area.

If the secondary electron yield of the dielectric side surface is assumed to be constant then the EFEE charging time is given by

$$\tau_{\text{efec}} = \frac{C_{\text{dielec}} d_i^2}{(\gamma_{\text{ec}} - 1) \sqrt{S_{\text{real}}} \eta \xi A \frac{S_{\text{FN}}}{S_{\text{real}}} B \beta} \exp\left(\frac{Bd}{\beta \eta \xi_0 V_c}\right) \quad (5-2)$$

where C_{dielec} is the capacitance of the dielectric at the first electron impact point, d_i is distance of the first electron impact point from the triple junction, γ_{ec} is the secondary electron yield, S_{real} is the emission site area accounting for electron space charge, η is a factor to account for the difference in the electric field between the emission site and the triple junction, ξ is a factor to account for the difference in dielectric constants between the coverglass and adhesive, A and B are the Fowler-Nordheim coefficients, S_{FN} is the emission site area determined from the Fowler-Nordheim plot, β is the emission site field enhancement factor, d is the dielectric thickness, and ξ_0 is the value of ξ at the front surface.

The total charging time is then given by the sum of the ion and EFEE charging times

$$\tau_{\text{chrg}} = \tau_{\text{ion}} + \tau_{\text{efec}} \quad (5-3)$$

As can be seen from the above equations, the ion flux, bias voltage and cell thickness, along with the cell material properties, play critical roles in determining the charging times, and therefore the arcing rates. From the model, arcing rates would be expected to increase with increasing ion flux, increasing voltage, and decreasing cell thickness. For a detailed description of the charging model, the reader is referred to References 5-1 and 5-2.

As the dielectric charges, the electrons impacting the side surface induce adsorbed neutrals to be desorbed. If the desorbed neutral density is larger than a critical density of approximately $6 \times 10^{21} \text{ m}^{-3}$ breakdown will occur. The desorbed neutral density is a function of the adsorbed surface neutral density, which is given by

$$N_n(t) = \frac{C_1}{C_2} (1 - e^{-C_2 t}) \quad (5-4)$$

where N_n is the adsorbed neutral density, C_1 is the incoming flux of neutrals, and C_2 is given by

$$C_2 = \frac{C_1}{N_{n0}} + k_1^0 \exp\left(-\frac{E_D}{kT_s}\right) \quad (5-5)$$

where N_{n0} is the neutral density for a monolayer coverage, k_1^0 is the neutral thermal desorption coefficient, E_D is the adsorption energy, T_s is the cell temperature, and κ is Boltzmann's constant. From this it can be seen that the neutral density is a strong function of cell temperature, and therefore, as cell temperature increases, the arc rate is expected to decrease. It is also expected that no arcing would occur above a critical temperature at which there would never be enough neutrals to allow breakdown to occur. In cases where the neutral density is insufficient for breakdown, a small current pulse from the field emission could still be seen until the emission becomes space charge limited.

5.2 Experiment Simulation and Data Analysis

The PASP Plus experiment biased a large set of conventional geometry, wrap-through-contact, and concentrator solar arrays to negative voltages ranging from -75 V to -450 V. The data returned includes arc counts, plasma density, cell temperature, and spacecraft position and orientation, as well as radiation and contamination data. This data allows correlations to be found between arcing and the environmental, operational, and cell geometry/material parameters, which can then be compared with the results from the model simulations.

The computer arc rate prediction code was run for the PASP Plus conventional geometry solar cell modules using the plasma densities and cell temperatures from the experiment. Figure 5-3 shows the typical temperature profiles for the conventional cells on August 22, 1994. As can be seen, the thin APSA cells, which are mounted with open backs, reach very high temperatures (60 C) in sunlight and cold temperatures (-60 C) in eclipse, while the thicker standard silicon shows a much lower temperature variation of -20 C to 40 C. Thus, it would be expected that the APSA cells would show higher arc rates in eclipse and lower arc rates in sunlight. In both the experiment and the simulations, the cells are biased for 23 seconds, but the first two seconds and the last second are not counted in order to avoid detecting the rise/fall of the cell bias. In the analyses of the experimental data, only pulses that are detected by the transient pulse monitors located nearest the biased module are counted.

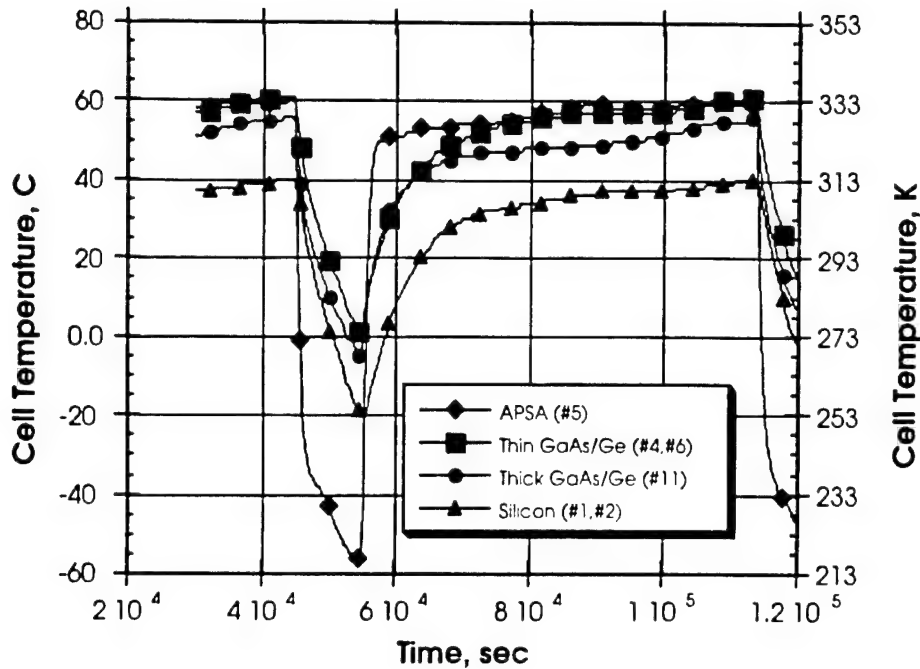


Figure 5-3. PASP Plus conventional geometry cell temperatures.

Figure 5-4 shows a comparison of the simulated and flight data for the standard silicon array Module 1 with a cell temperature of 310 K and an ion flux of $8 \times 10^{13} \text{ m}^{-2}\text{s}^{-1}$, while Figure 5-5 shows the comparison for Module 2 at the same conditions. These two modules differ only in the number of cells (20 on Module 1 and 60 on Module 2). In the graphs, the squares show the maximum number of arcs seen during the 100 simulated trials, while the triangles show the minimum number of arcs seen. The figures show that the arc rate increases with bias voltage, and that the amount of arcing increases with array area. It can also be seen that the simulation is accurately predicting the arc rates for these arrays. For low voltages, the EFEE charging time is expected to dominate. Thus, a fit of the flight data to the form suggested by Equation 5-2 is shown in Figure 5-6. This shows that the data is fit very well by the model form. However, it should be noted that the coefficients of the fit do not match the values expected from typical values of the parameters in Equation 5-2. This is due to the fact that in performing a fit, it is assumed that the parameters in the fit are not functions of the independent variable. This, however, is not the case. In Equation 5-2, many of the parameters vary with bias voltage. For example, as voltage increases, emission sites with lower field enhancement factors, β , are able to arc. Therefore, this factor decreases as a function of voltage. Thus, while the model equation

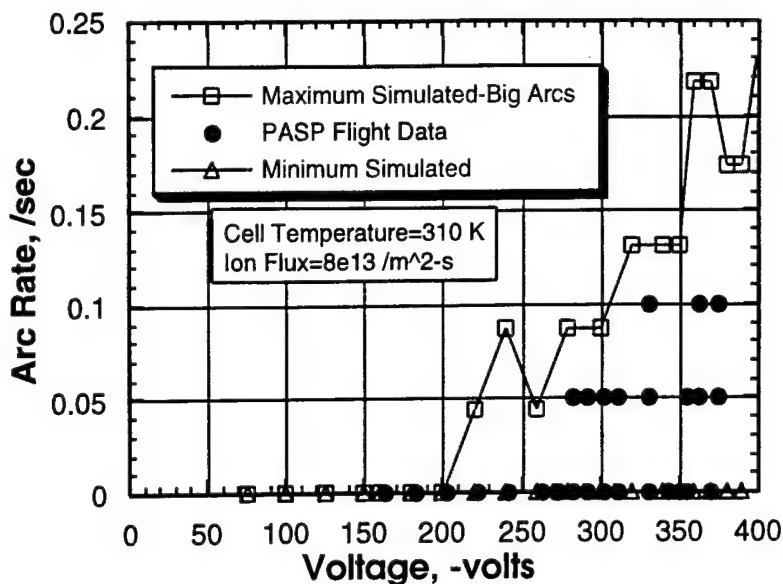


Figure 5-4. Standard silicon array Module 1 arc rate variation with voltage.

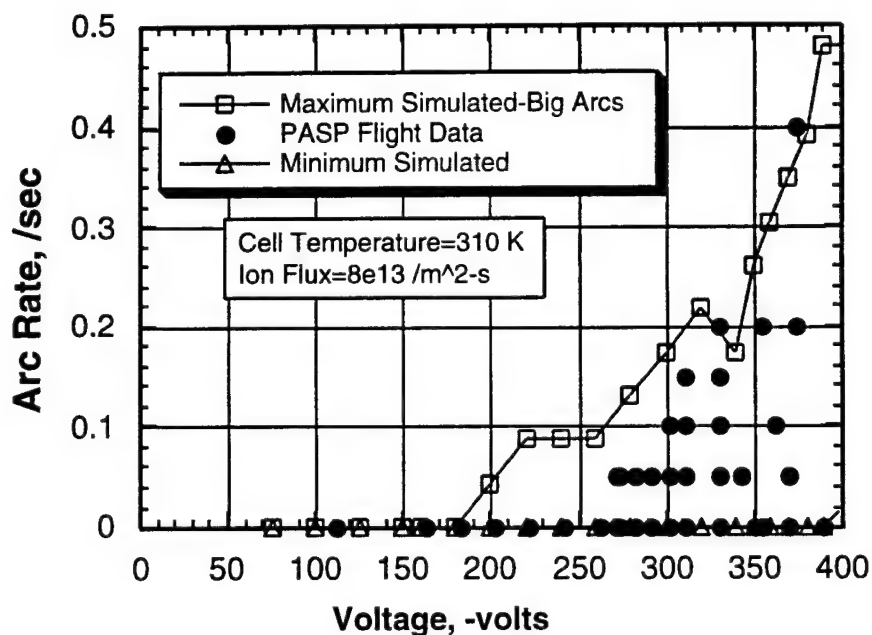


Figure 5-5. Standard silicon array Module 2 arc rate variation with voltage.

form fits the data well, the coefficients must be determined by fits either to experimental data or to simulated data, since the simulations do not assume constant values for the parameters. Once, the coefficients are determined, the model form accurately describes the arcing variation with voltage, including the onset characteristics.

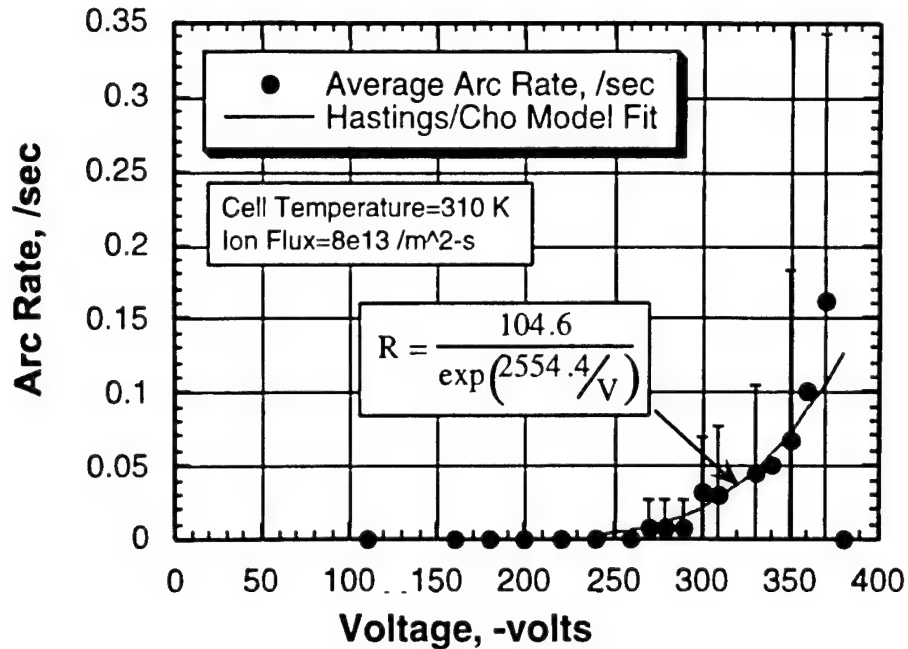


Figure 5-6. Hastings/Cho model fit to standard silicon array Module 2.

From Equations 5-1 through 5-3, it can be seen that for a given experiment duration, there is a critical ion flux below which no arcing will occur. For ion fluxes below this critical value, the ion charging time will be longer than the total experiment and no arcs will be seen. Using Equation 5-1 for Module 2 at -300 V, the theoretical ion charging time was calculated as a function of ion flux and is shown in Figure 5-7. From this, it can be seen that for ion fluxes less than approximately $8 \times 10^{12} \text{ m}^{-2}\text{s}^{-1}$, the theoretical charging time will be greater than the 23 second PASP Plus biasing duration. Figures 5-8 and 5-9 show the arc rate variation with ion flux for Module 2 at 310 K and voltages of -300 V and -330 V, respectively. Although not conclusive, these graphs imply a critical ion flux in the range of 2 to $4 \times 10^{13} \text{ m}^{-2}\text{s}^{-1}$. This is close to the theoretical value of $8 \times 10^{12} \text{ m}^{-2}\text{s}^{-1}$, with the difference possibly due to the time for EFEE charging that must also be done before arcing occurs.

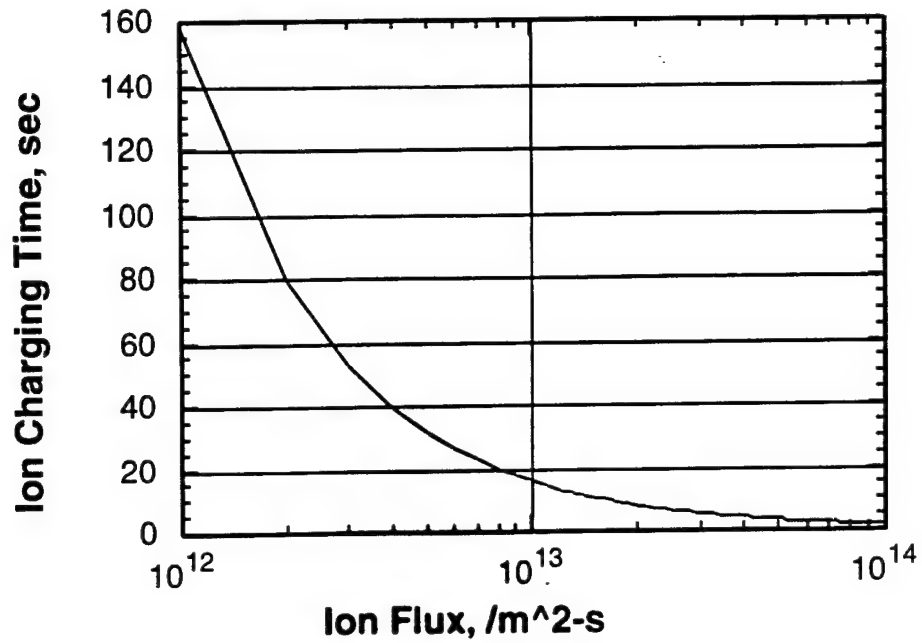


Figure 5-7. Theoretical ion charging time: silicon array Module 2.

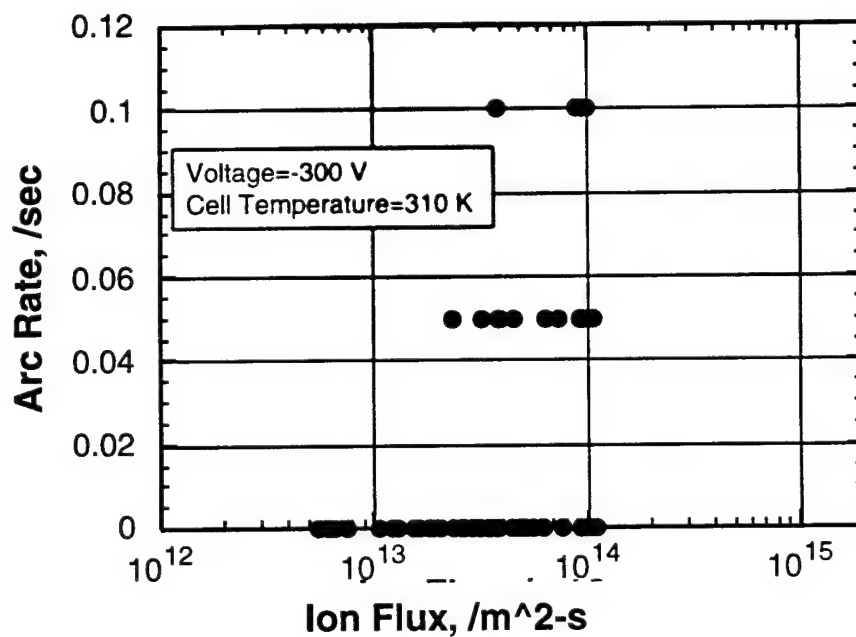


Figure 5-8. Standard silicon array Module 2 arc rate variation with ion flux at -300V.

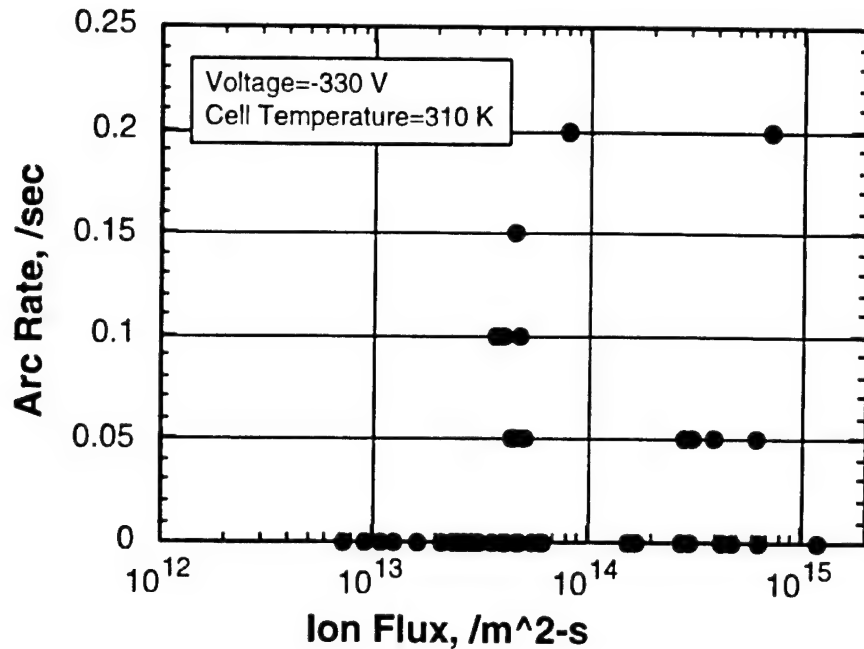


Figure 5-9. Standard silicon array Module 2 arc rate variation with ion flux at -330V.

Along with voltage and ion flux, cell temperature is expected to be a primary factor in the arcing process. Figure 5-10 shows the arc rate variation with cell temperature for the APSA Module 5 at -300 V. This clearly shows that arcing occurs only at the lower temperatures, with no arcing occurring in the many trials above 310 K. From the model, a critical temperature above which no arcing occurs is to be expected. Figure 5-11 shows a plot of the simulated arc rate variation for the APSA cells at -300 V and three different background neutral densities. This shows that a critical cell temperature of between 300 K and 350 K is expected for neutral densities between 3×10^{12} and $3 \times 10^{14} \text{ m}^{-3}$. At the lower densities of PASP Plus, a lower critical temperature would be expected. Figure 5-12 shows the variation in arc rate with voltage for the APSA array at 215 K, which is colder than the standard silicon arrays went to. Again, a clear increase in arc rate is seen with increasing voltage. The onset voltage for arcing is approximately -100 V. This low voltage is due to the thinness of the dielectric on APSA arrays compared to standard cells, which is a strong factor in the EFEE charging time (see Equation 5-2). Again, the simulations accurately predict the arcing levels.

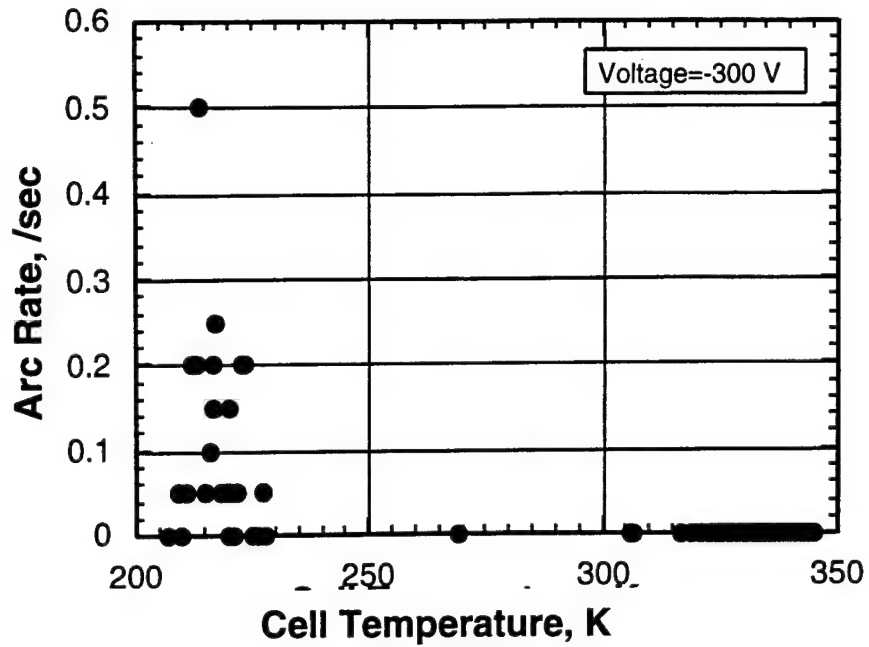


Figure 5-10. APSA array Module 5 arc rate variation with cell temperature at -300V.

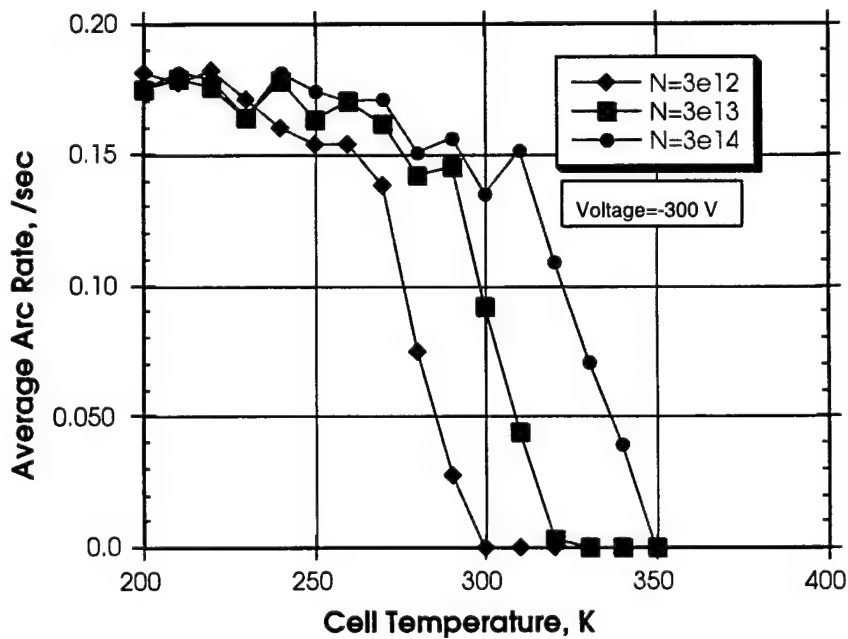


Figure 5-11. Simulated APSA array Module 5 arc rate variation with cell temperature at -300V.

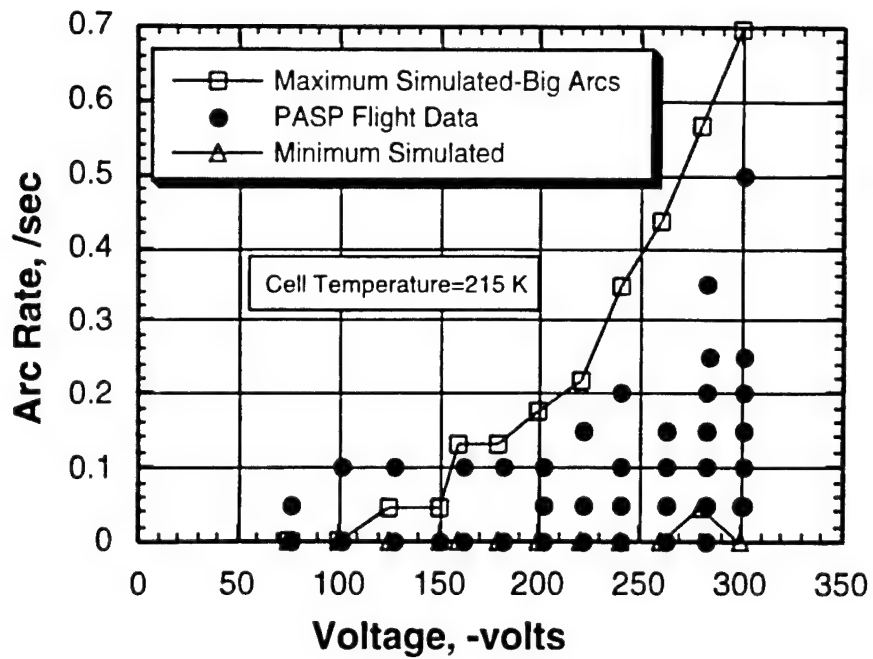


Figure 5-12. APSA array Module 5 arc rate variation with voltage.

Table 5-1. Experimental Arcing Probability

| Module | Total Area (cm ²) | Dielectric Thickness (μm) | Arcing Probability (percent) |
|-----------------------------|----------------------------------|------------------------------|---------------------------------|
| (1) Standard Silicon | 160 | 190 | 41 |
| (2) Standard Silicon | 480 | 190 | 68 |
| (3) Silicon WTC | 256 | 203 | 6 |
| (4) GaAs/Ge | 320 | 153 | 35 |
| (5) APSA | 122.4 | 127 | 48 |
| (6) GaAs/Ge | 192 | 153 | 24 |
| (8) GaAs/Ge WTC | 64 | 152 | 10 |
| (11) GaAs/Ge | 128 | 228 | 12 |
| (14) GaAs Mini-Cas | | | 0 |
| (15) GaAs/GaSb Mini-Dome | | | 0 |

Table 5-2. Simulated and Experimental Arcing Onset Voltages

| Array | Simulated Onset Voltage | Experimental Onset Voltage |
|------------------------|-------------------------|----------------------------|
| (1,2) Standard Silicon | -160 V | -160 V |
| (5) APSA | -100 V | ~-75 to -125 V |
| (4,6) Thin GaAs/Ge | -120 V | -125 V |
| (11) Thick GaAs/Ge | -180 V | -180 V |

Table 5-1 shows the percentage of times arcing occurred on each module when biased to -300 V and the cell temperatures were less than 300 K (except for the concentrator arrays, which were never below 300 K).

The Space Station wrap-through-contact cells are proving to be much more resistant to arcing than the conventional geometry cells. The dielectric thickness is also an important factor in the arcing process. The arrays with thin dielectrics are showing higher arc rates compared to the cells with thick dielectric layers. The concentrators are show very little arcing, which is to be expected since the cells are shielded from the ambient plasma.

5.3 Conclusions

The PASP Plus experiment returned a large amount of data on the arcing characteristics of negatively biased solar arrays in the space plasma environment. Arcing rates and probabilities were dependent on the bias voltage, cell area, cell dielectric thickness, cell temperature, ion flux, and cell geometry. The arcing simulation accurately predicted the arcing levels on the conventional geometry solar array modules. Table 5-2 shows a comparison of the simulated and experimental arcing onset voltages for the conventional cells. For this simulation, the cells were biased for 60 minutes with a cell temperature of 200 K and an ion density of $3.5 \times 10^{11} \text{ m}^{-3}$. These conditions were chosen as worst case conditions to find the lowest possible onset voltage. The bias voltages chosen for the simulations matched those used in the experiment. The arcing onset voltage clearly decreases with decreasing dielectric thickness.

The cells were found to show higher arcing at cold temperatures, which is expected from the model, since at cold temperatures there is a higher neutral density on the dielectric side surface, increasing the probability of breakdown. The data from the APSA cells implies a critical cell temperature above which no arcing would occur. At these temperatures, there is never a high enough neutral density for breakdown. During the experiment, increases in the arc rate were also observed as the spacecraft transitioned from eclipse to sunlight. During these periods, the cells heated up and thermally desorbed adsorbed neutrals, further increasing the chances for breakdown.

A possible critical ion flux for arcing is also seen from the experiment. Fluxes below this level result in charging times greater than the 23 second experiment duration. Also, lower arcing levels are seen in the wake than in ram, where the ion fluxes are much lower. Cells not near the edge of the panel (i.e. modules 1 and 5) show no arcing for angles-of-attack greater than 105° , because of the low resulting ion flux. At lower angles, or on cells near the edge, a sufficient number of ions are drawn around the edge of the panel to charge the dielectric and lead to breakdown.

The cells with thin dielectric layers are showing higher arc rates, while the wrap-through-contact and concentrator designs are showing low arc rates. The arcing rates also increase with cell area, as expected.

References for Chapter 5

- 5-1. D. E. Hastings, M. Cho, and H. Kuninaka, "The Arcing Rate for High Voltage Solar Arrays: Theory, Experiment, and Predictions" *Journal of Spacecraft and Rockets*, Vol 29, No. 4, p 538, 1992.
- 5-2. J.D. Soldi and D.E. Hastings, *Arcing Predictions for PASP Plus Solar Arrays*, Technical Report PL-TR-94-2234, Phillips Laboratory, 1994.

Chapter 6

Parasitic Current Collection by PASP Plus

V. A. Davis, Maxwell Federal Division, Inc.

One of the primary goals of the PASP Plus experiment is to improve our understanding of and quantify parasitic current collection by solar arrays on spacecraft. At low potentials little current is collected by the environment. Above 50 V, a phenomena called snapover occurs in which the current from the plasma dramatically increases. The amount of current depends primarily on the potential of the solar cells with respect to the plasma, the plasma density, and the spacecraft attitude. A Langmuir probe was included in the instrumentation in order to measure the plasma density.

6.1 Langmuir Probe Measurements and Models

Insight into the limitations of models and measurements can be gained by comparing them with each other. For this reason, we compared the various Langmuir probe measurements with models we have at our disposal. We looked at two time periods.

The first time period examined was the first five and one-half hours of August 8, 1994 GMT (day 94220). We used the orbit parameters for APEX from August 7, 1994. Figure 6-1 shows the altitude as computed by EPSAT, which uses the orbit generator ORB, and as output by the PASP Plus software. The agreement suggests that we are modeling the orbit reasonably closely.

Figure 6-2 shows the angle between the ram direction and the solar array normal. The one degree difference between the extreme values given by EPSAT and the extreme values given by the PASP Plus software is due to several factors. APEX does not follow the sun perfectly. The angle between the sun direction and the solar array normal at the time of the first peak in the ram sun angle is 0.4 degrees. The precession of the orbit is not completely followed correctly by the ORB orbit generator. This accounts for up to 0.5 degrees. There may be other contributions also. The level of agreement does indicate that the orbit model is not following the APEX orbit perfectly.

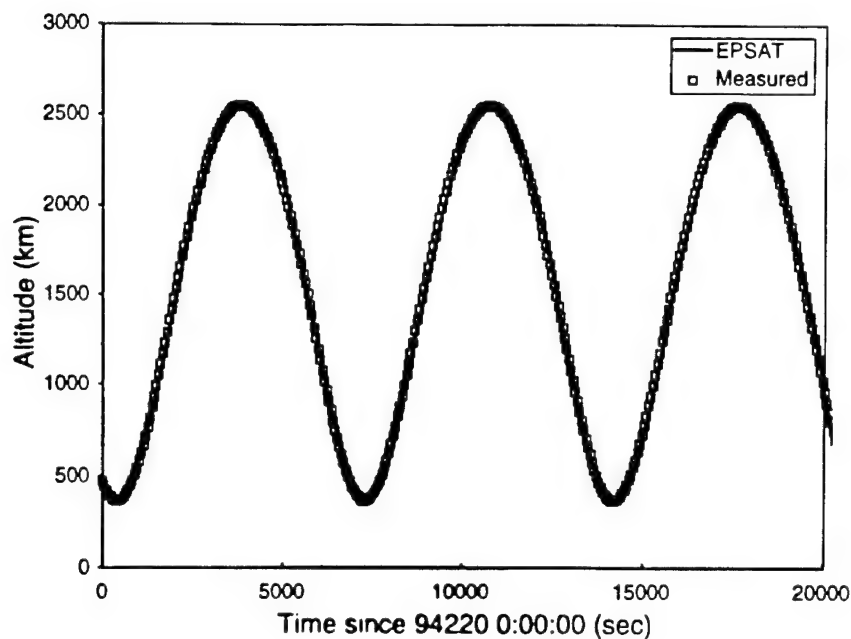


Figure 6-1. Altitude of the APEX spacecraft on August 8, 1994.

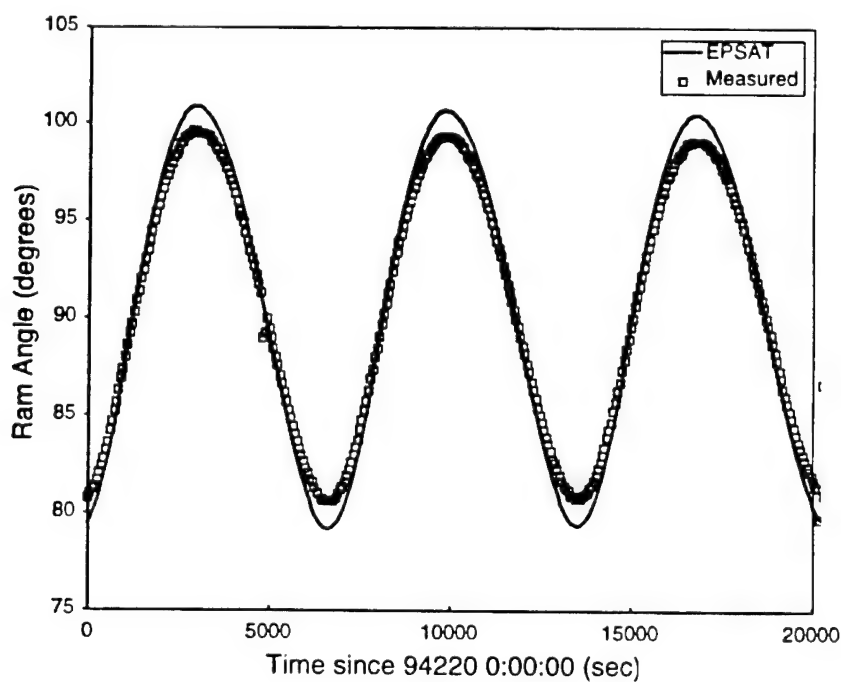


Figure 6-2. Attitude of the APEX spacecraft on August 8, 1994.

Figure 6-3 shows the plasma density as determined from measurements by the Langmuir probe and the plasma density as computed by EPSAT using the IRI-86 model and the ORB orbit generator. Above 1000 km, EPSAT assumes that the plasma density drops in the manner

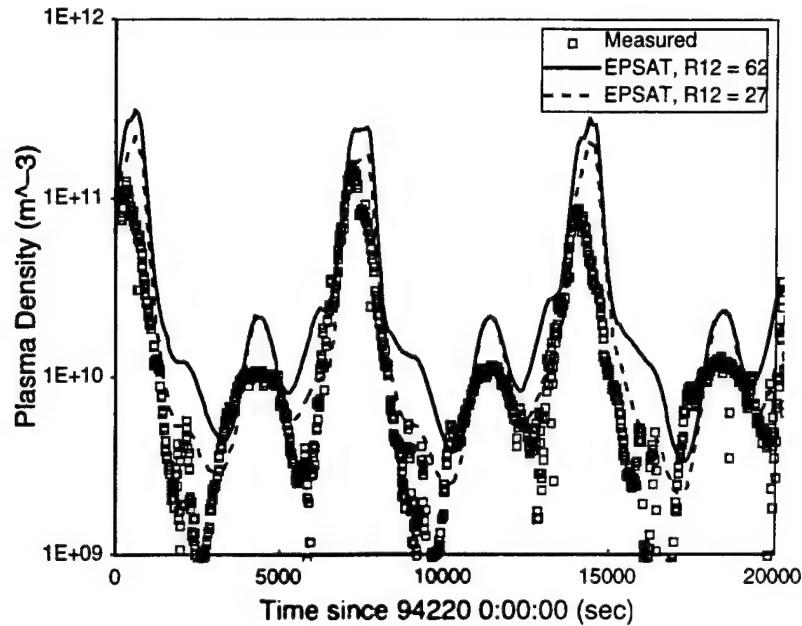


Figure 6-3. Plasma density at the APEX spacecraft on August 8, 1994.

suggested by Al'pert. One of the input parameters to the IRI model is the sunspot number, R12. The EPSAT default sunspot number for this day is 62. The actual sunspot number for this time is 27. The peaks in the plasma density as modeled by IRI are narrower for the lower sunspot number. For both values of the sunspot number, the measured plasma density is lower than the model by a factor of about three. It should be noted that in August 1994, the APEX orbit was such that the low altitudes, high densities occurred while the spacecraft was at the higher latitudes where the IRI model is less accurate.

Figure 6-4 shows the plasma temperature as determined from measurements by the Langmuir probe and the plasma temperature as computed by EPSAT using the IRI-86 model and the ORB orbit generator. The plasma temperature as modeled by IRI does not vary significantly with sunspot number for this case. The model temperature is about 50 percent below the measured values. From the two plasma measurements, we get that the difference between the model plasma thermal current and the plasma thermal current determined from the measurements is a factor of about 2.5, with the model value higher. The difference between the model debye length and the debye length determined from the measurements is a factor of about 1.4, with the measured value higher.

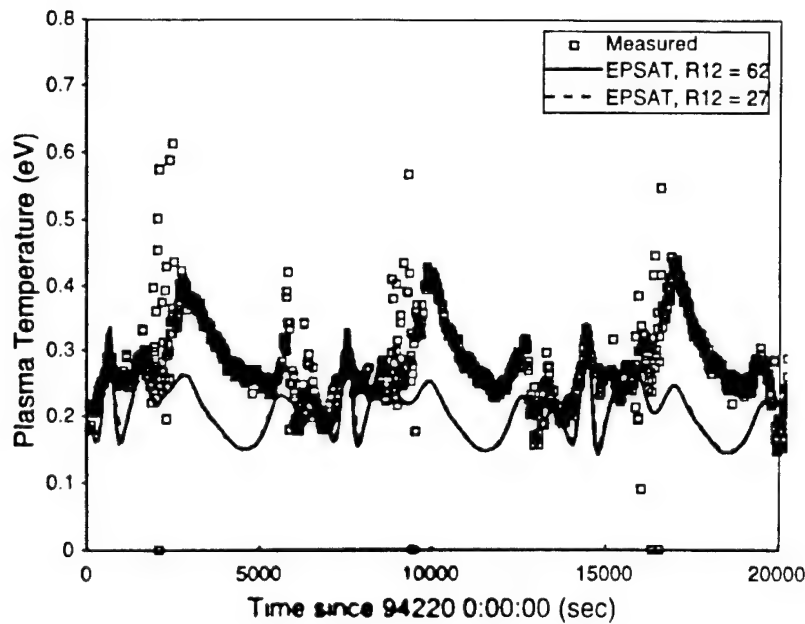


Figure 6-4. Plasma temperature at the APEX spacecraft on August 8, 1994.

Figure 6-5 shows the APEX floating potential as determined from measurements by the Langmuir probe (SENPOT) and the APEX floating potential as computed by EPSAT using the model environments above, the model developed under this contract for solar array current collection, and the EPSAT floating potential model as described in the EPSAT documentation. (The EPSAT and EWB floating potential algorithm for this problem are the same.) The floating potential is determined by the balance between the ion current to the spacecraft body and the electron (and ion) current collected by the power solar arrays. The difference in time of the peak floating potential values is due to a difference in the time of the peak plasma density between the model and the measurements and an unknown factor. That the measured and model values are as similar as they are suggests that the solar array model developed for solar cells between 50 and 500 V can be used for some problems with solar cells from 0 to 36 V.

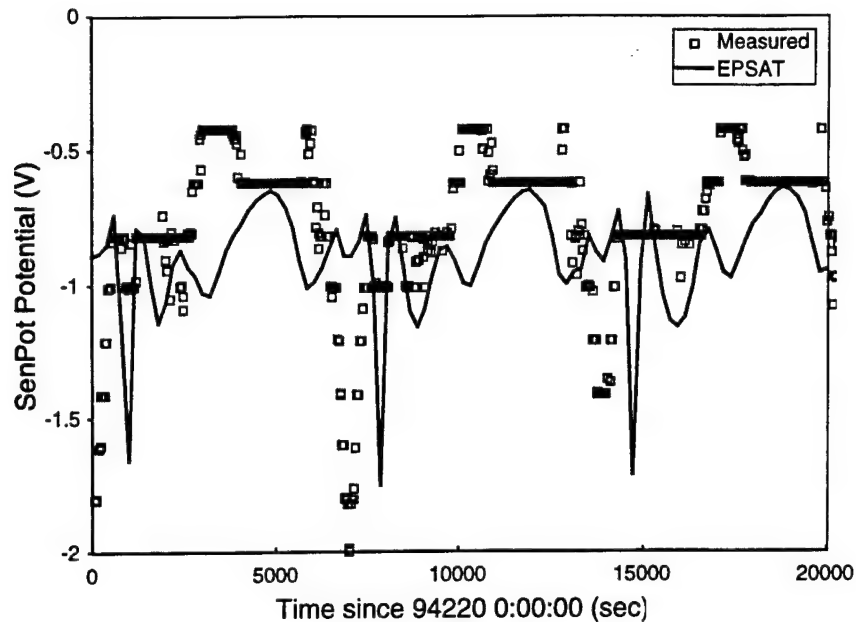


Figure 6-5. APEX floating potential on August 8, 1994.

We looked at the same quantities for the first five and a half hours of February 12, 1995 GMT (day 95043). We used the orbit parameters for February 9, 1995. We adjusted the mean anomaly by 10 degrees in order to track the altitude correctly. We do not have a good enough understanding of the ORB orbit generator to know why this is necessary and if it is appropriate. Figures 6-6 through 6-10 are the various quantities computed. There is a difference of 3 degrees between the calculated and measured peak sun-ram angles. This is most likely due to imperfections in tracking the orbit. The model and measured densities agree better than they do for the August date. In early February, the high plasma density portion of the orbit is in the mid-latitudes where the IRI model is most accurate. The model floating potential varies less than the measured floating potential. In the model, the contribution of current through the Z-93 paint helps to balance the electron current collected by the modules. These measurements could be used to extend the solar array model developed under this contract to solar cells at potentials of 0 to 50 V with respect to the plasma. Electrostatic barriers are known to play a role at the lower potentials.

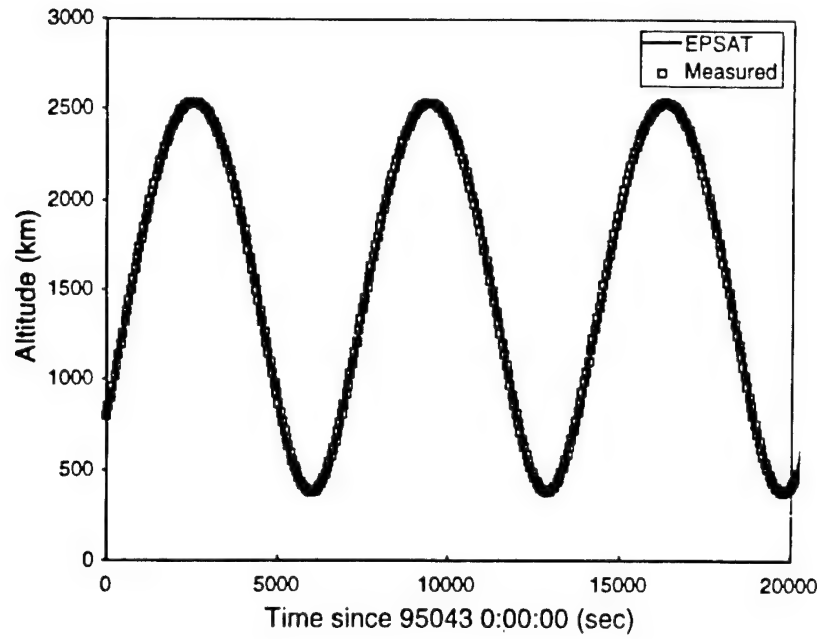


Figure 6-6. Altitude of the APEX spacecraft on February 12, 1995.

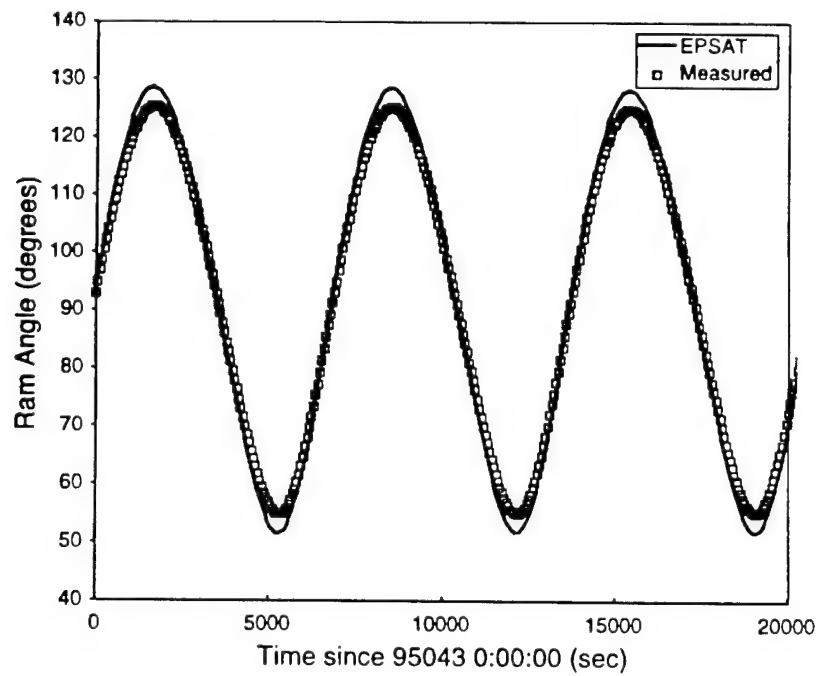


Figure 6-7. Attitude of the APEX spacecraft on February 12, 1995.

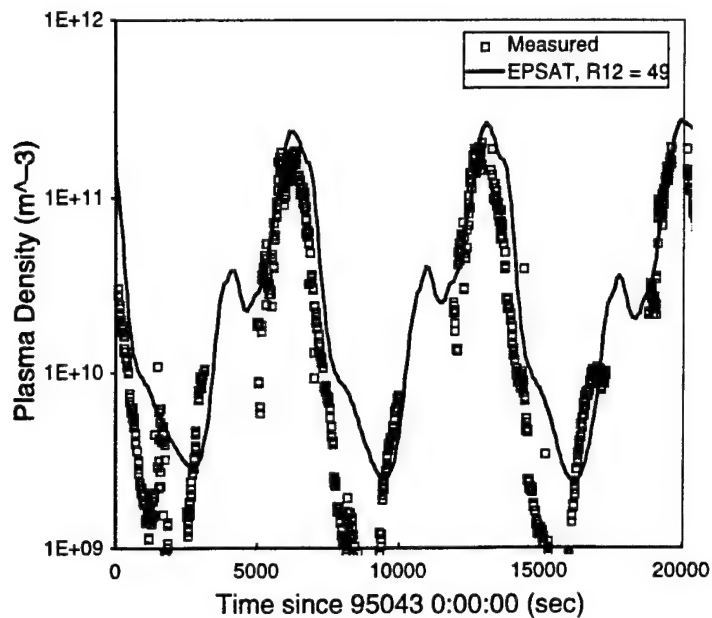


Figure 6-8. Plasma density at the APEX spacecraft on February 12, 1995.

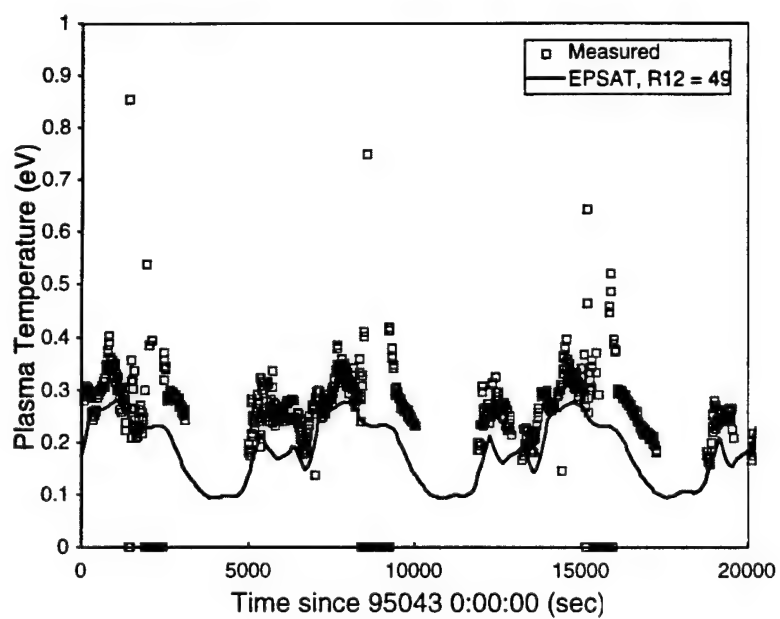


Figure 6-9 Plasma temperature at the APEX spacecraft on February 12, 1995.

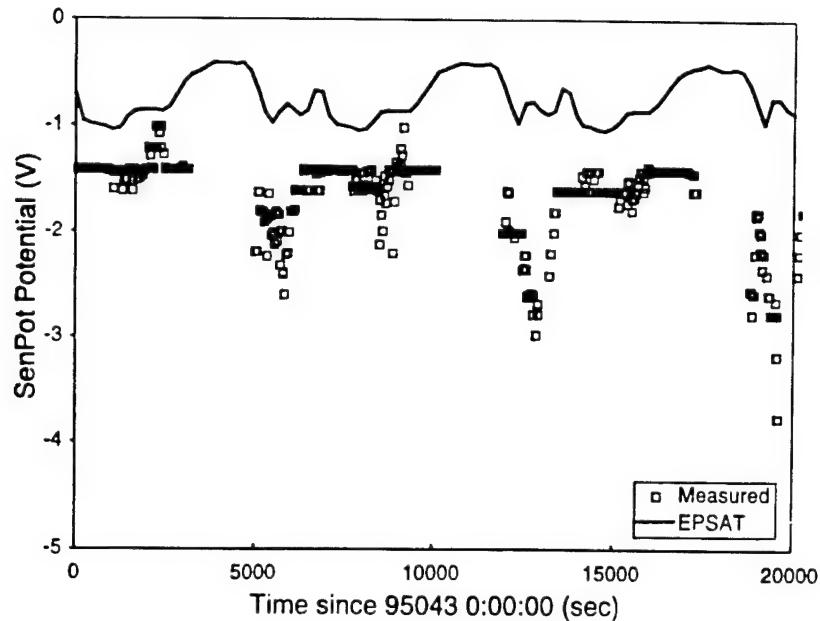


Figure 6-10. APEX floating potential on February 12, 1995.

Accuracy of PASP Plus Langmuir Probe

Densities of the order of 10^9 m^{-3} in sunlight cannot be measured properly as the photoelectrons dominate. Densities greater than $3 \times 10^{11} \text{ m}^{-3}$ also present problems and are unavailable.

We examined the density measurements on a sample day. The ratio of density measurements made 1 second apart varied from 0.108 to 6.07 with 93 percent between 0.8 and 1.25. The ratio of density measurements made 29 seconds apart varied from 0.074 to 8.9 with 91 percent between 0.8 and 1.25. The ratio of temperature measurements made 1 second apart varied from 0.297 to 3.132 with 99 percent between 0.8 and 1.25. The ratio of temperature measurements made 29 seconds apart varied from 0.33 to 2.45 with 96 percent between 0.8 and 1.25.

The ratio of the sizes of the spacecraft body and the probe is such that a few volts on the probe is enough to shift the spacecraft ground potential. Figure 6-11 shows the probe potential with respect to plasma ground as a function of the probe bias. It is linear up to about 4 V with respect to plasma ground. This figure was made for midnight at the start of day 220 in 1994. The plasma density is about 10^{11} m^{-3} and the electron temperature is 0.1 eV. Figure 6-12 compares the current collected by the probe as a function of the applied bias with the current as a function of

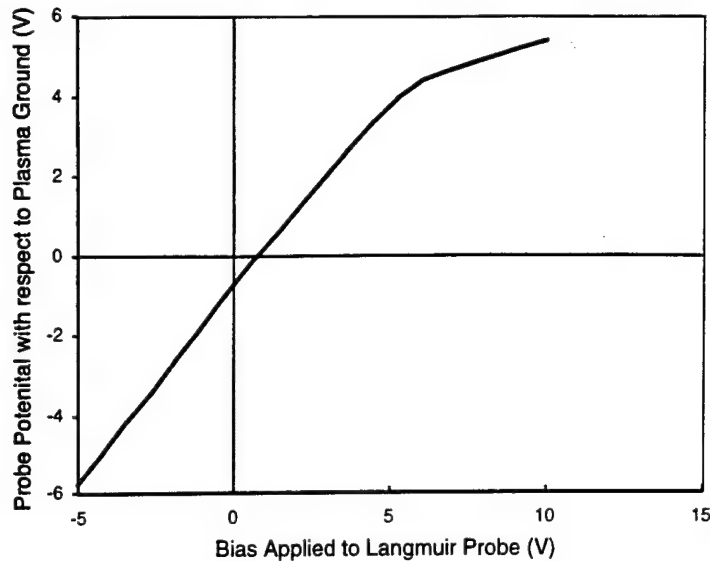


Figure 6-11. Probe potential with respect to plasma ground as a function of the probe bias. Figure is for the conditions at midnight at the start of day 220 in 1994. The plasma density is about 10^{11} m^{-3} and the electron temperature is 0.1 eV.

the probe potential with respect to the plasma. As long as the zero potential offset is included in the interpretation, voltage sweeps under 4 V with respect to the plasma should give reasonable results.

6.2 Current Collection as a Function of Bias and Plasma Density

We examined the measured collected current as a function of the applied bias, plasma density, and temperature. We focused on measurements made in the ram and with the emitter off. We expect that the wake measurements depend on the attitude of APEX. Generally, when the emitter is on, the APEX floating potential is positive and the algorithm for the determination of the plasma density and temperature does not work.

Wake measurements and emitter on measurements should be examined at some time in the future.

Leakage current is measured as part of a 30 second sequence of measurements. During each 30 second sequence there are two Langmuir probe sweeps (one up and one down) with the

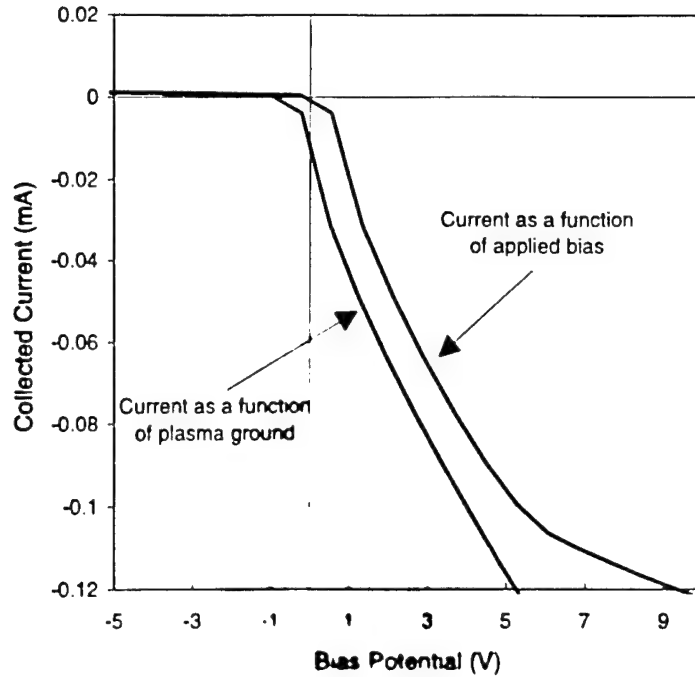


Figure 6-12. Collected current as a function of the probe bias. Figure is for the conditions at midnight at the start of day 220 in 1994. The plasma density is about 10^{11} m^{-3} and the electron temperature is 0.1 eV.

applied bias at zero, and then 23 measurements of the leakage current with the applied bias at a constant. In order to obtain a single current collected, plasma density, and plasma temperature for each 30 second sequence, the following procedure was used. The current collected is the twenty-second current measurement. The plasma density is the plasma density measurement that follows the current measurement sequence. The plasma temperature is the one made at the same time as the density measurement. Current measurements for which the plasma parameters are unavailable were ignored. Alternative schemes were tried and none gave more believable results.

In order to plot the leakage current, we averaged the data. For each 30 second sequence, a collecting area was calculated.

$$\text{Collecting Area (m}^{-2}\text{)} = \frac{\text{Leakage Current (A)}}{2.68 \times 10^{-14} \text{ Density (m}^{-3}\text{)} \sqrt{\text{Temperature (eV)}}} \quad (6-1)$$

The measurements were sorted into bins by plasma density, plasma temperature, and applied bias. The plasma density bins are each a half decade per bin and are labeled by the density at the

geometric center of the bin. Only measurements from $1.78 \times 10^9 \text{ m}^{-3}$ to $5.62 \times 10^{11} \text{ m}^{-3}$ were included. Lower density measurements are excluded because photoemission dominates. Higher density measurements are excluded because the density measurement is unavailable. The probe is unable to properly measure the high current. The plasma temperature bins are 0.1 eV in width and are labeled by the temperature at the center of the bin. Almost all of the measurements are between 0.05 eV and 0.35 eV. There are 23 logarithmically spaced applied bias bins labeled by the bias at the center of the bin. The bins are the following: 49.4, 54.6, 60.3, 66.7, 73.7, 81.5, 90.0, 99.5, 110, 122, 134, 148, 164, 181, 200, 221, 245, 270, 299, 330, 365, 403, 446, and 493 V.

For each plasma density, plasma temperature, and applied bias bin, the average collecting area was computed. As the plasma conditions and applied bias are correlated with the time on orbit, attitude, and location within the orbit, unknown and unaccounted for systematic factors may influence these measurements.

Plots of the collecting area as a function of applied bias and plasma density appear in Figure 6-13. Several features of interest are clear on inspection of the figures.

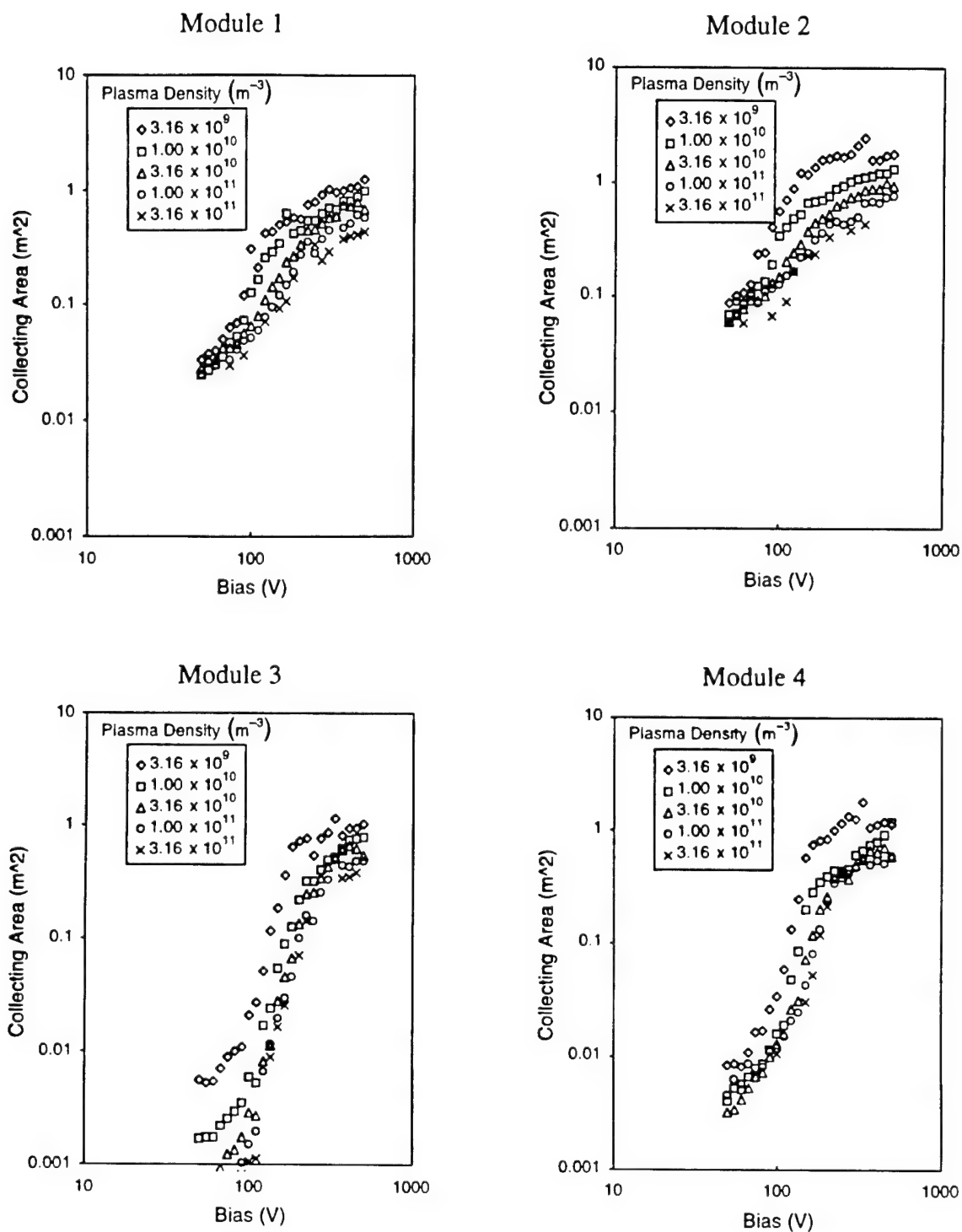


Figure 6-13. Collecting area as a function of cell bias and plasma density (part 1, Modules 1, 2, 3, and 4.).

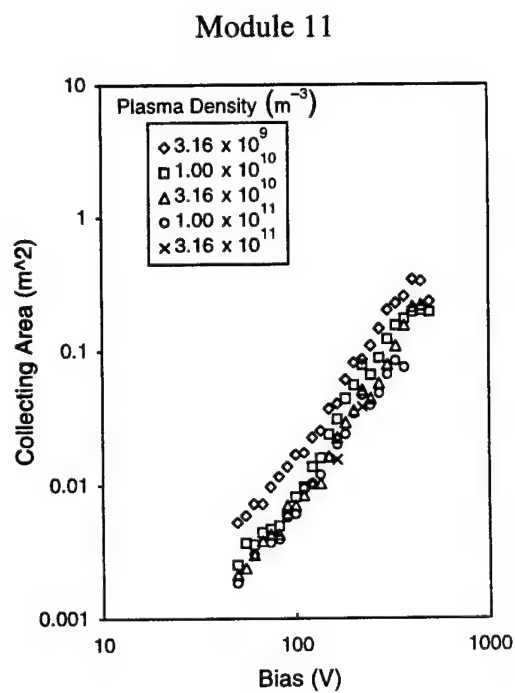
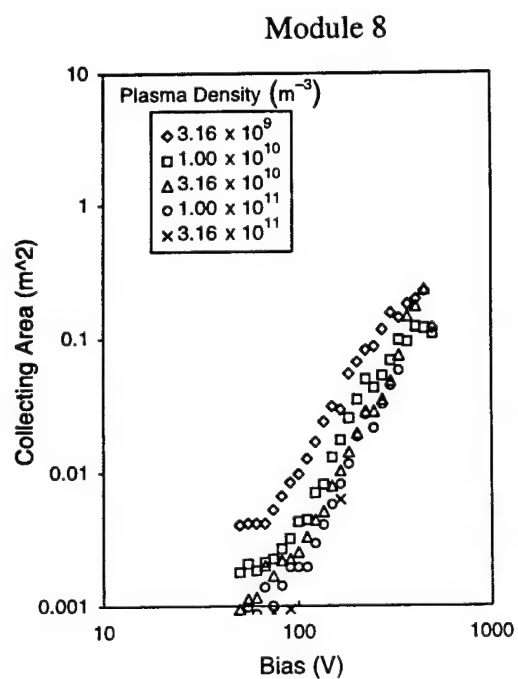
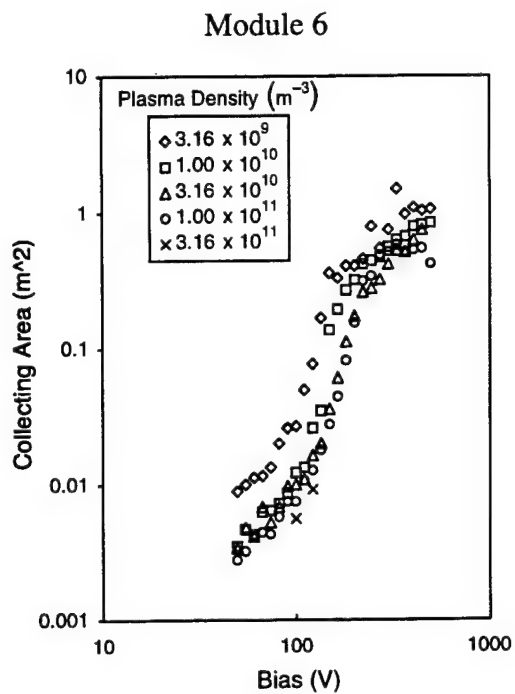
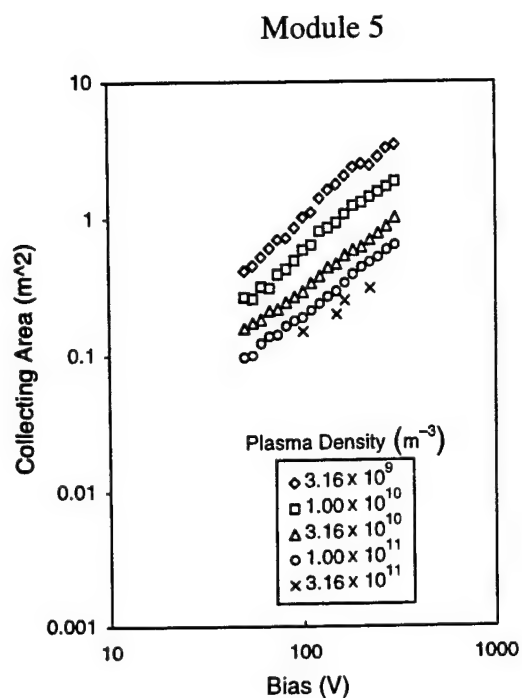


Figure 6-13. Collecting area as a function of cell bias and plasma density (part 2, Modules 5, 6, 8, and 11.).

Table 6-1. Solar-Cell and Module Panel Areas for the PASP Plus Planar Arrays

| Module | Module Area (m ²) | Panel Area (m ²) |
|--------|-------------------------------|------------------------------|
| # 1 | 0.016 | 0.129 |
| # 2 | 0.048 | 0.129 |
| # 3 | 0.026 | 0.078 |
| # 4 | 0.032 | 0.129 |
| # 5 | 0.015 | 0.059 |
| # 6 | 0.019 | 0.129 |
| #8 | 0.0064 | 0.029 |
| # 11 | 0.013 | 0.029 |

Overall, the collecting area rises about two orders of magnitude as the applied bias rises one order of magnitude. This is typical of leakage current when snapover plays a role in the current collection process. Modules 1 and 2, the conventional interconnect design, do not rise as quickly, particularly at the high bias end. This may be because the collected current is high enough that the APEX floating potential goes negative in order to collect enough ions to balance the electron current collected by the biased array module. The APEX floating potential and current collection characteristics are discussed in Section 6-4.

As expected, the current collection characteristic of Module 5, APSA, is different than all of the other modules. Module 5 is discussed in Section 6-7.

In general the collected current is several times the module area. Table 6-1 gives the module and panel areas for the various modules.

There is a minimum collecting area for each plasma density that is the same for all of the modules. The smallest measured PASP Plus leakage current value is 0.2 μ A. Collecting areas near and below this value should be ignored. Table 6-2 relates the minimum leakage current to collecting area.

Table 6-2. Collecting Area in Square Meters at Minimum Leakage Current

| Collecting Area (m ²) | | | |
|-----------------------------------|--------------------|--------|--------|
| Plasma Density | Plasma Temperature | | |
| | 0.1 eV | 0.2 eV | 0.3 eV |
| $3 \times 10^9 \text{ m}^{-3}$ | 0.0075 | 0.0053 | 0.0043 |
| $1 \times 10^{10} \text{ m}^{-3}$ | 0.0024 | 0.0017 | 0.0014 |
| $3 \times 10^{10} \text{ m}^{-3}$ | 0.0007 | 0.0005 | 0.0004 |
| $1 \times 10^{11} \text{ m}^{-3}$ | 0.0002 | 0.0002 | 0.0001 |
| $3 \times 10^{11} \text{ m}^{-3}$ | 0.0001 | 0.0001 | 0.0000 |

The collecting area does not depend strongly on the plasma density and temperature. The collecting area is larger for lower densities (longer debye lengths). The dependence on density is stronger for lower densities.

There is a large amount of scatter in the graphs. When the several measurements in the same bin are compared, variations of a factor of ten are common. Section 6-5 addresses this issue.

6.3 Variation within a Measurement

Each leakage current measurement consists of 23 measurements taken approximately one per second. In general, the 23 measurements vary.

APEX moves fast enough that its plasma environment can vary during the 30 second sequence of a single measurement. Throughout the orbit, the density varies from low to high as often as from high to low. However, we are only examining ram measurements. This introduces an unintended bias in one direction or the other. The following example illustrates how the bias is introduced. Most of the measurements were taken within 20 minutes of perigee. Sometimes the array modules are in the wake during the first 15 minutes of data collection. During the 40 minute period of data collection, the density goes from high to low more than from low to high. The reverse happens when the wake period is at the end of the data collection period. This variation with epoch has not been systematically controlled. A similar bias was introduced by the early practice of making measurements on the array modules consecutively. As a result, measurements

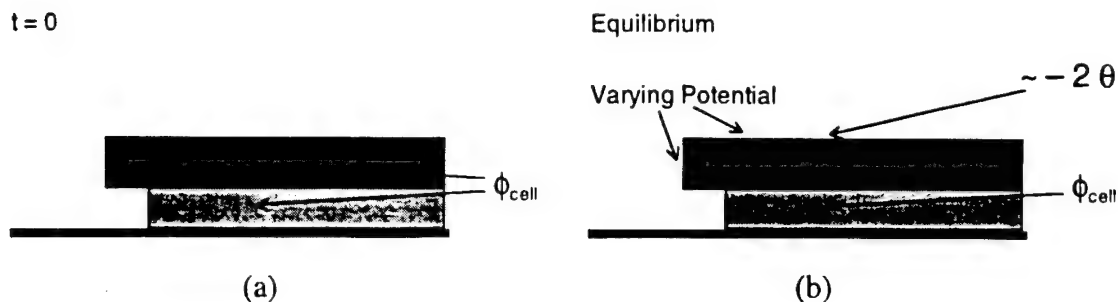


Figure 6-14. Differential charging across solar cell coverglass.

on a given array module at a given applied bias were made predominately at two or three well-separated points in the orbit. Fortunately, the variation in collecting area during the current collection period due to changes in the environment is generally under a few percent.

Differential charging causes a systematic variation in leakage current. Differential charging can occur through the thickness of the test solar cells, through the thickness of the Z-93 paint, and through any annodization or other layer on the surface of the APEX spacecraft. Since APEX is advertised to be completely covered with conducting surfaces (mostly thermal blankets with the conducting side out), this last effect is ignored here.

Figure 6-14(a) illustrates the edge of a solar cell covered by a coverglass and supported by an insulating backing immediately after a bias is applied to the cell. Before the plasma has a chance to respond, the solar cell coverglass and the insulating backing are at the same potential as the solar cell. The electrons in the plasma are attracted to the positive potential coverglass. They deposit their charge on the surface of the coverglass until the surface of the coverglass has a negative potential of a couple of times the plasma temperature. Figure 6-14(b) shows the equilibrium situation. This process is differential charging.

The incident electrons create secondary electrons. Some remain at their creation location developing a differential potential. Some travel across the surface toward the higher potential. Some of these are ultimately collected by the solar cell. These show up as an enhanced leakage current until the equilibrium situation is reached. Those electrons collected as leakage current do not reduce the potential on the coverglass surface.

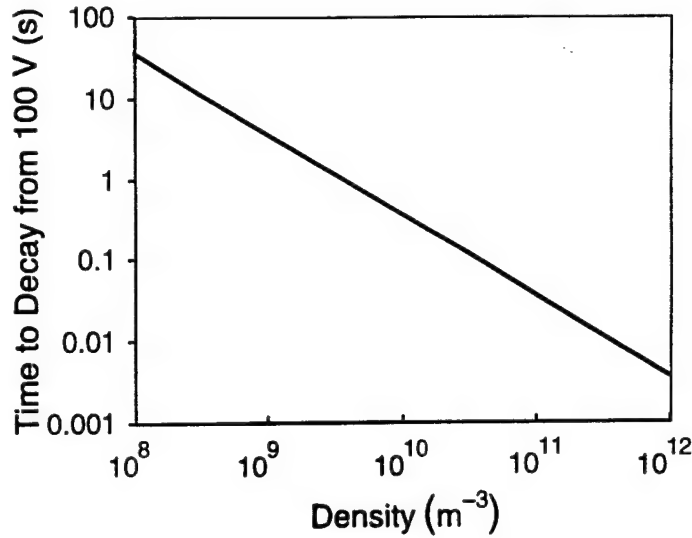


Figure 6-15. Time to decay from 100 V for Module 4 coverglass.

The time scale over which differential charging takes place depends on the incoming current, j_{th} , the dielectric constant, κ , and the thickness of the coverglass, Δ , as well as the initial and final surface potentials.

$$\tau = \frac{(\phi_{cell} + 2\theta) \kappa \epsilon_o}{\Delta (j_{th} - j_{collected})} \quad (6-2)$$

In order to obtain an estimate of the time scale, we ignore the temperature and collected current terms. For glasses, the dielectric constant is three or higher. Modules 4 and 6 have 3.5 mil thick coverglass. Figure 6-15 shows the time to decay from 100 V as a function of the density. At 10^{10} m^{-3} , the time to decay from 100 V is one-third of a second. Since the leakage current does not contribute to reducing the surface current, the actual time to decay is longer.

The Module 4 portion of the data set described in Section 6-2 was examined for systematic variations. In order to examine the relative variation, we normalized the current measurements.

$$\text{Ratio}_i^j = \frac{I_i^j}{\sum_{n=2 \text{ to } 22} I_n^j} \quad (6-3)$$

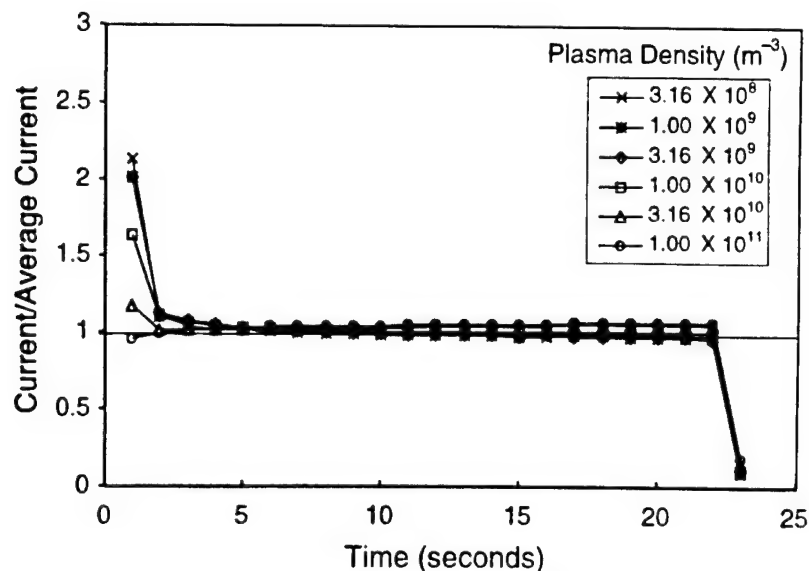


Figure 6-16. Average time variation of Module 4 leakage current for various plasma densities.

The i index refers to the 23 consecutive current measurements. The j index refers to the 30 second measurement sequence. Figure 6-16 shows ratio averaged over all j values for each density as a function of i . The peak current is higher for the lower densities.

The 23rd measurement is systematically approximately one-fifth the average. The reason for this is unknown.

Figure 6-17 shows the maximum ratio for each density value as a function of i . This figure illustrates how high above the average the current measurements are. The amount of maximal variation does not appear to be correlated with density.

Figures 6-16 and 6-17 are examinations of the entire data set at once and show little about how the current measured during a specific 30 second sequence behaves. Figures 6-18 and 6-19 show the time variation for ten specific sequences each. The sequences chosen are the ten at the specified density for which ratio_2^i is largest.

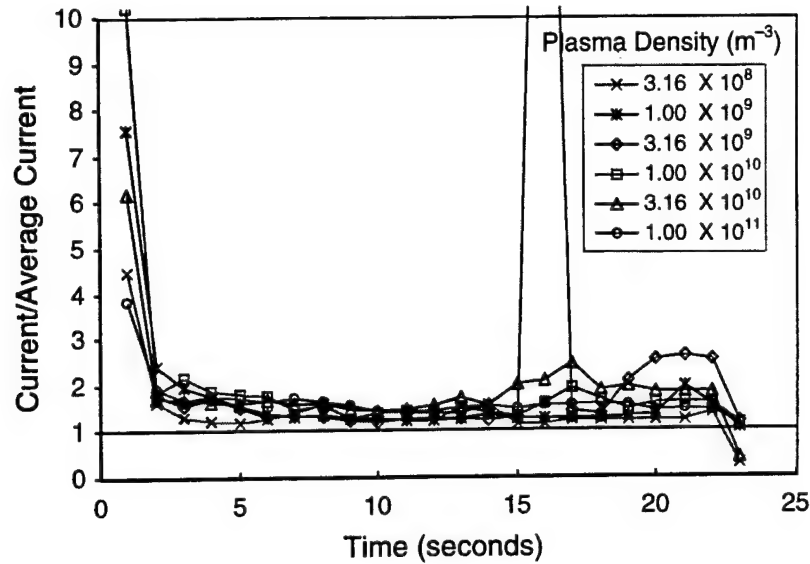


Figure 6-17. Maximal time variation of Module 4 leakage current for various plasma densities.

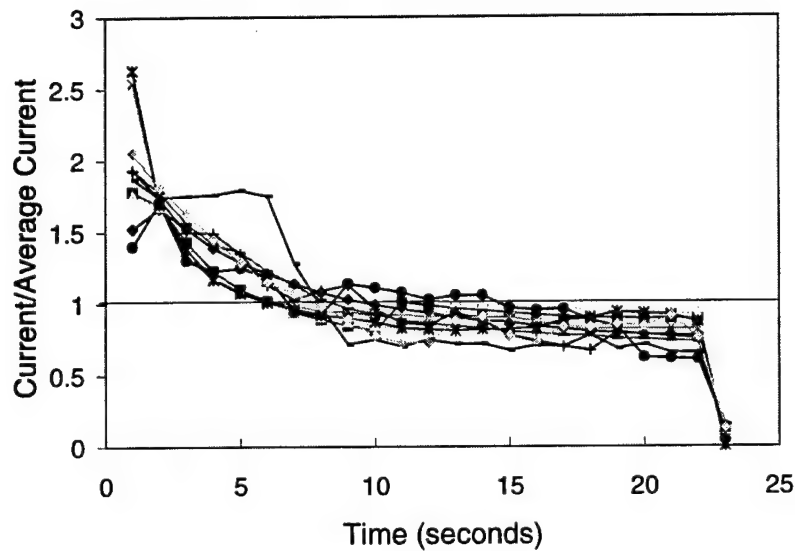


Figure 6-18. Time variation of Module 4 leakage current between $5.62 \times 10^{10} \text{ m}^{-3}$ and $1.78 \times 10^{10} \text{ m}^{-3}$ for the ten sequences with the highest value of ratio at the second point.

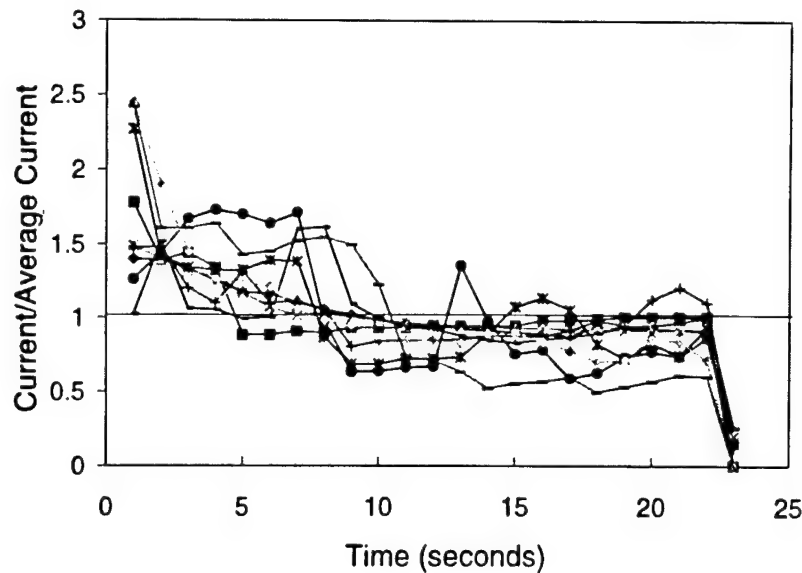


Figure 6-19. Time variation of Module 4 leakage current between $5.62 \times 10^{11} \text{ m}^{-3}$ and $1.78 \times 10^{11} \text{ m}^{-3}$ for the ten sequences with the highest value of ratio at the second point.

The variation in current seen in Figures 6-18 and 6-19 has several sources. At 10^{10} m^{-3} , there is a decrease in current on a time scale of a few seconds. This is consistent with differential charging across the coverglass. The most likely source for most of the rest of the variation is variations in the environment. It is also possible that the extent of the snapover varies under constant conditions.

At both densities, there is a decrease in current on a time scale on the order of 30 seconds. This does not occur in the average or maximum plots. This effect must occur only some of the time. One explanation would be that in these particular cases, the plasma density is decreasing during the measurement period. However, for the ten cases at the higher density, only four of them are during a period of decreasing plasma density. The others have a decreasing or constant plasma density.

6.4 APEX Current Collection Characteristics and Floating Potential

The floating potential of APEX influences the current collected by the modules in two ways. First, the potential difference between the module and the plasma is the sum of the potential of

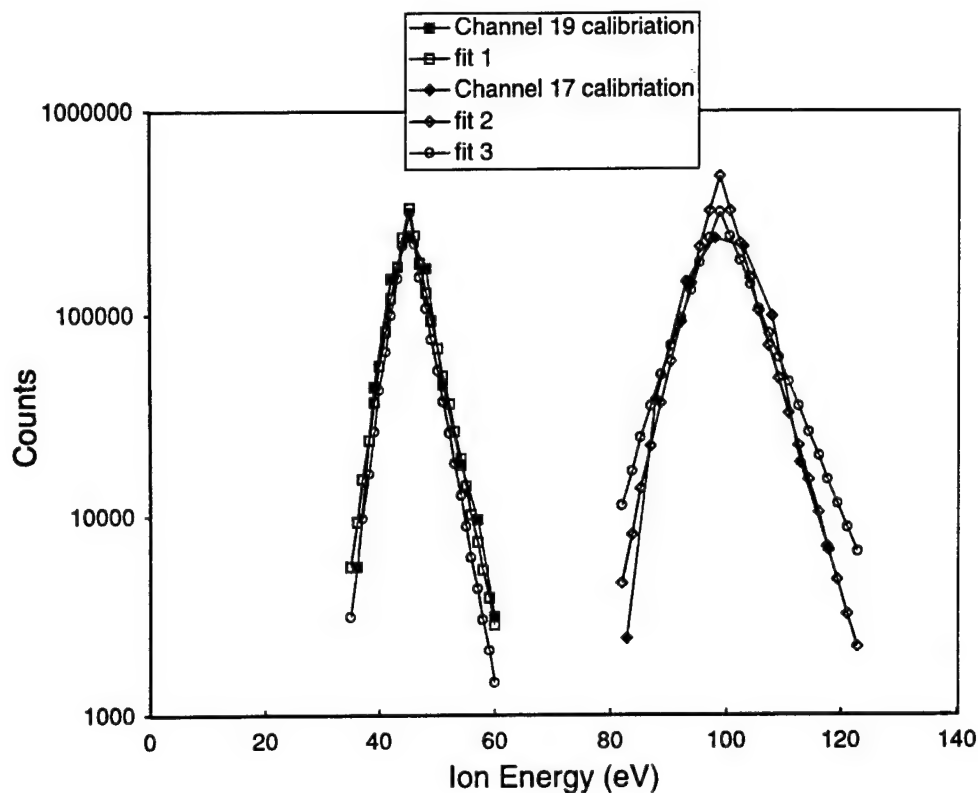


Figure 6-20. Count rate as a function of calibration beam and fits for ESA similar to the one on APEX.

APEX and the applied bias. Second, all of the exposed, grounded, conducting surfaces are at the APEX floating potential and influence the potential in the surrounding space.

Using the ESA to Estimate the APEX Floating Potential

We can use the calibration information to determine the best way to use the ESA count rates to estimate the floating potential. Figure 6-20 shows the count rates from channels 17 and 19 of the SSJ4 calibration of the S13 refurbishment for DMSP F13. This device is similar enough to the one on APEX for our present purposes. Also shown in Figure 6-20 are three fits to the measured points. Fits 1 and 2 are fits to each peak individually. Fit 3 is a fit to both at once.

Fit 1 Counts = $5.3 \times 10^{11} e^{-14x}$

Fit 2 Counts = $2.3 \times 10^{15} e^{-22x}$

Fit 3 Counts = $3 \times 10^{12} e^{-16x}$

where $x = \max\left(\frac{\phi}{\phi_{\text{peak}}}, \frac{\phi_{\text{peak}}}{\phi}\right)$ (6-4)

The two simplest approaches to using the ESA measurements to estimate the ESA potential are linear and logarithmic. The logarithmic estimate requires a scaling constant. The resulting estimate is not sensitive to the constant.

$$\text{Linear Estimate} = \frac{\sum_{\text{all channels}} \phi_{\text{peak}} \text{Counts}}{\sum_{\text{all channels}} \text{Counts}} \quad (6-5)$$

$$\text{Log Estimate} = \frac{\sum_{\text{all channels}} \phi_{\text{peak}} \ln\left(\frac{10^6 \text{Counts}}{\text{Total Counts}}\right)}{\sum_{\text{all channels}} \ln\left(\frac{10^6 \text{Counts}}{\text{Total Counts}}\right)} \quad (6-6)$$

We can use Fit 3 to determine what the count rate would be for a given true potential. Then we can use the two estimates to estimate the potential. A comparison between the estimated potential and the true potential allows us to determine the accuracy of the estimating technique.

Figure 6-21 shows this plot. An examination of Figure 6-21 indicates that both of these methods of estimating the potential have an accuracy of 50 percent.

During biasing with the emitter off, the current collected by APEX can be estimated to be the current collected by the biased solar array module. The other sources of current are typically much lower. Since the total current must be zero, the electron current collected by the biased module must be approximately the ion current to APEX. The ion collecting area can be estimated by

$$\text{Ion Collecting Area}(\text{m}^{-2}) \sim \frac{\text{Leakage Current}(\text{A})}{1.6 \times 10^{-19} \text{ Dens}(\text{m}^{-3}) \text{ Velocity}(\text{m s}^{-1})} \quad (6-7)$$

Figure 6-22 shows the ion collecting area as a function of potential as determined from the ESA measurements. The entire data set (with emitter off and excluding periods when Module 5 is biased) is included. The data is binned, in half decades of density and factors of 1.2 in potential, and averaged.

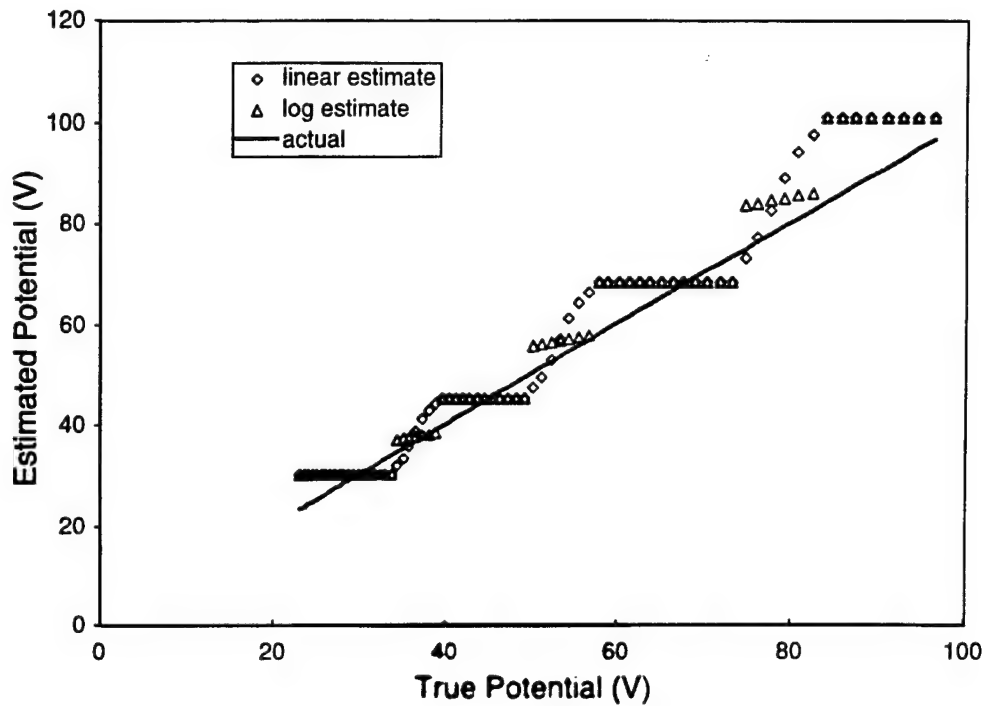


Figure 6-21. Estimated potential as a function of true potential.

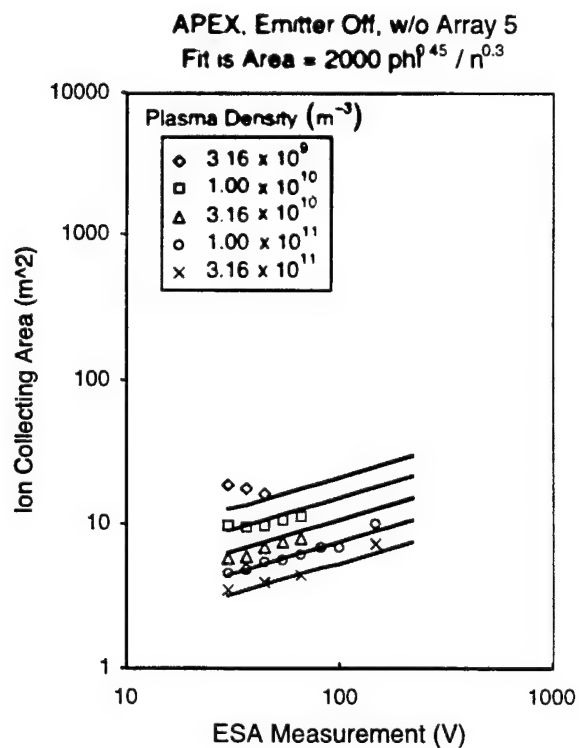


Figure 6-22. Ion collecting area as a function of potential as estimated from leakage current and ESA measurements.

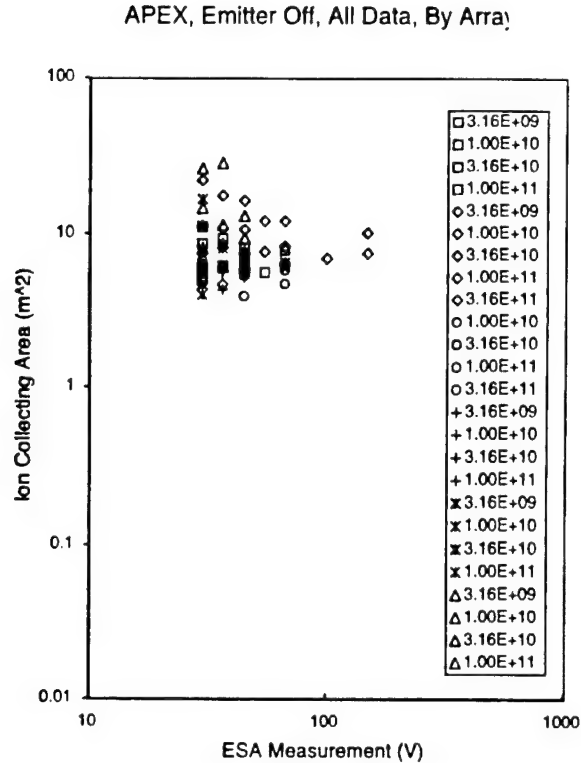


Figure 6-23. Ion collecting area as a function of potential as estimated from leakage current (separated by module) and ESA measurements. The different symbol shapes indicate which module: squares for Module 1, diamonds for Module 2, circles for Module 3, pluses for Module 4, stars for Module 5, and triangles for Module 6. The shades of gray indicate the plasma density.

Figure 6-22 treats the current collected by any of the modules (except 5) as equally valid in the estimation of the ion collection. Figure 6-23 shows collected area as estimated from each of the modules alone. Note that Module 5 gives a larger area than any of the others. This is because the current measured for Module 5 is the sum of the current from the environment and the current that flows through the semiconductive coating.

Simple Fit to the Data

Several different techniques were tried to obtain an overall fit to the data. One fit is given by

$$\text{Ion Collecting Area (m}^{-2}\text{)} = 2000 \frac{\phi^{0.45}}{n^{0.3}} \quad (6-8)$$

Without Array 5

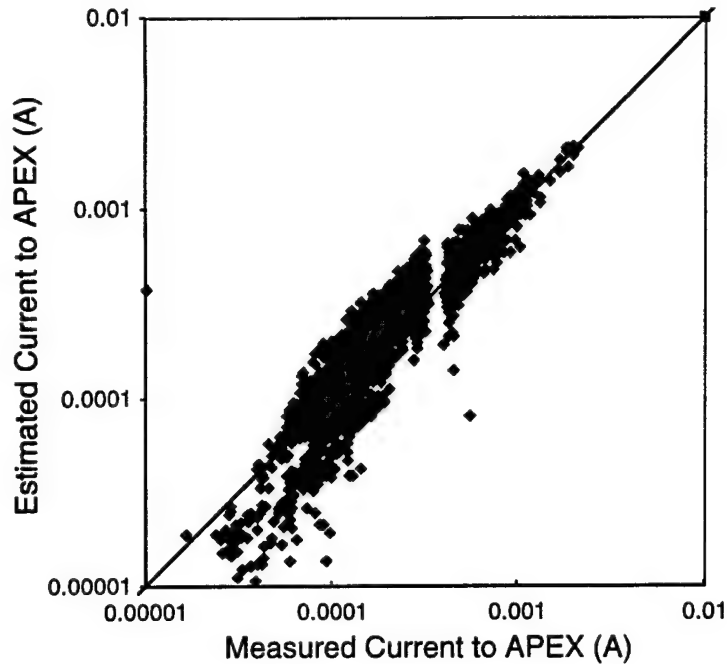


Figure 6-24. Estimated current to APEX compared with the measured current collected by a biased module.

This is the fit shown in Figure 6-22.

We now have a fit to the APEX ion collection as a function of APEX potential. We can use the fit to estimate the leakage current from the ESA measurements. Or we can use the fit to estimate the APEX floating potential from the leakage current measurements.

$$\text{Estim. Leakage Current} = 1.6 \times 10^{-19} \times \text{Dens.} \times \text{Vel.} \times 2000 \times \frac{\text{ESA Measurement}^{0.45}}{\text{Dens.}^{0.3}} \quad (6-9)$$

$$\text{Estimated APEX Potential} = \left(\frac{\text{Leakage Current Measurement} \times \text{Density}^{0.3}}{1.6 \times 10^{-19} \times \text{Density} \times \text{Velocity} \times 2000} \right)^{2.22} \quad (6-10)$$

Figure 6-24 compares the estimated current to APEX with the measured current to a biased module, and Figure 6-25 compares the estimated spacecraft ground potential with the ESA measurement. Note that there are no measurement with currents between 0.325 and 0.4 mA. This is at the upper end of the lower leakage current range that the controller is designed to measure. This is well within the upper leakage current range.

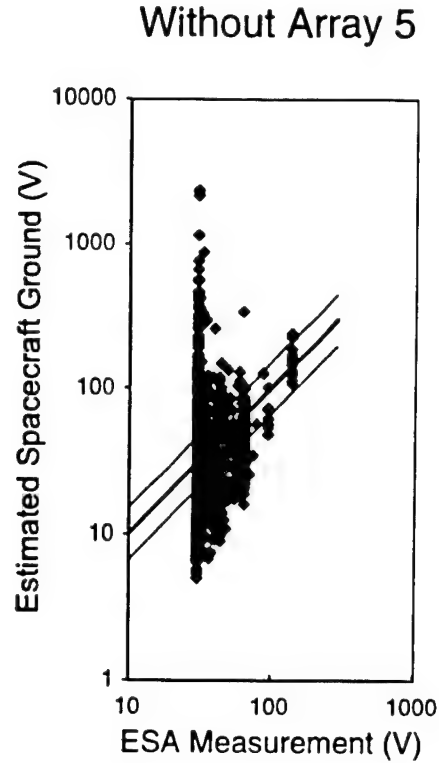


Figure 6-25. Estimated spacecraft ground potential compared with the ESA measurement.

Another Fit to the Data

Another fit to the APEX current collection flight data can be obtained by treating the spacecraft as a sphere in a plasma and computing its sheath radius. We know that

$$\frac{\phi}{\theta} = 0.8356 \left(\frac{r}{\lambda} \right)^{4/3} \left[\left(\frac{r}{a} \right)^{3/4} - \left(\frac{a}{r} \right)^{0.17} \right]^{4/3} \quad (6-11)$$

where λ is the debye length, a is the sphere radius, r is the sheath radius, ϕ is the potential, and θ is the plasma temperature, provides a good fit to the numeric solution of a spherical sheath. If we use a sphere radius of 0.75 m and a plasma temperature of 0.2 eV, we obtain a good fit to the flight data as seen in figure 6-26.

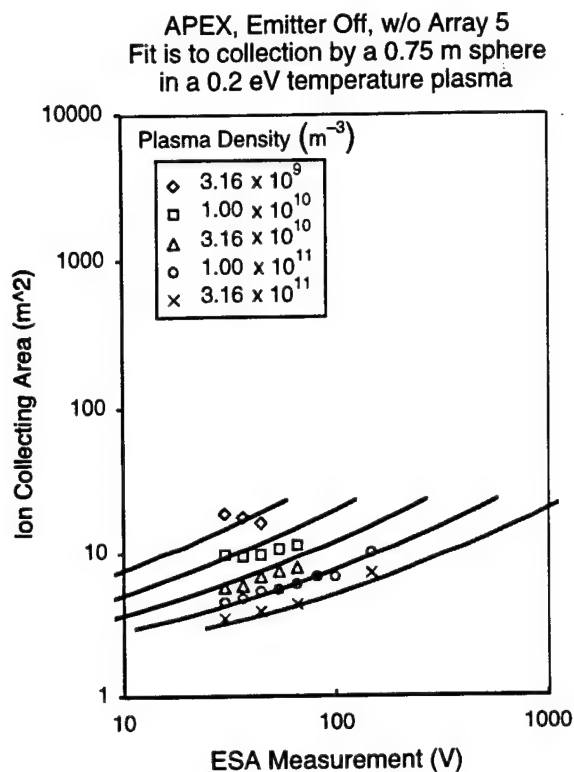


Figure 6-26. Ion collecting area as a function of potential as estimated from leakage current and ESA measurements.

Using this formula we can estimate the APEX floating potential from the leakage current.

$$r(m) \sim \frac{1}{\pi} \sqrt{\frac{\text{Leakage Current(A)}}{1.6 \times 10^{-19} \text{ Dens(m}^{-3}) \text{ Velocity(m s}^{-1})}} \quad (6-12)$$

$$\lambda(m) = 7.44 \times 10^3 \sqrt{\theta(\text{eV})/n(\text{m}^{-3})} \quad (6-12)$$

$$\frac{\phi}{\theta} = 0.8356 \left(\frac{r}{\lambda} \right)^{4/3} \left[\left(\frac{r}{a} \right)^{3/4} - \left(\frac{a}{r} \right)^{0.17} \right]^{4/3} \quad (6-13)$$

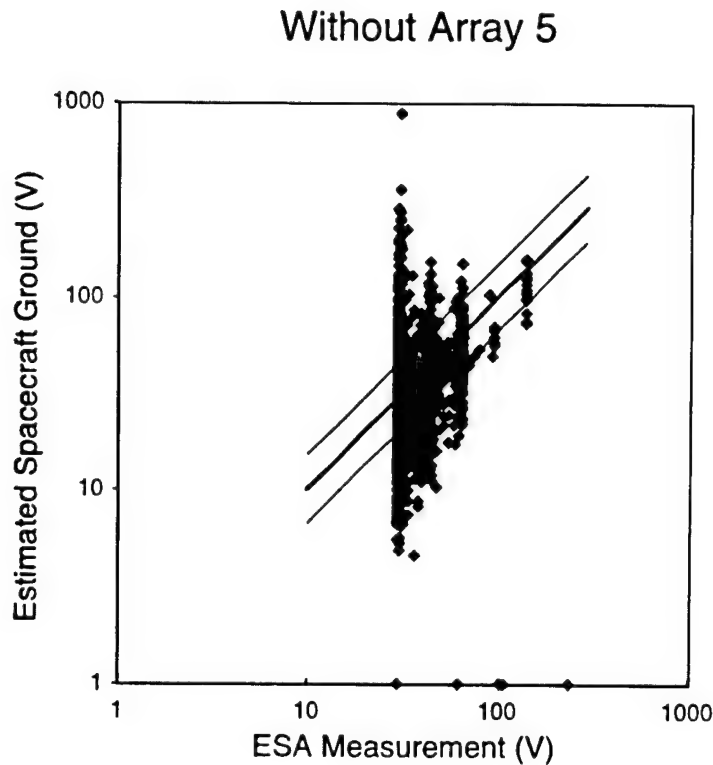


Figure 6-27. Estimated spacecraft ground potential compared with the ESA measurement assuming spherical current collection.

Influence of the Floating Potential

Figures 6-28 and 6-29 show how the current voltage curve for the Module 2 changes when the floating potential of APEX is included. At low bias values the floating potential is negligible. As the electron current becomes larger than the ion current for an uncharged APEX, the floating potential grows and a lower current is collected than if the spacecraft did not charge. The collecting area for the potential difference between the biased array and the surrounding plasma (plotted in Figures 6-28 and 6-29) is greater than the collecting area for the same potential between the biased array and spacecraft ground.

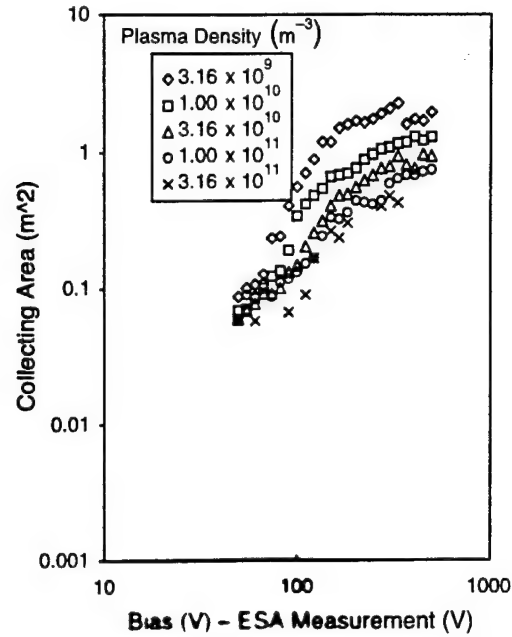


Figure 6-28. Collecting area as a function of bias minus the value of the floating potential as determined from the ESA measurement for Module 2.

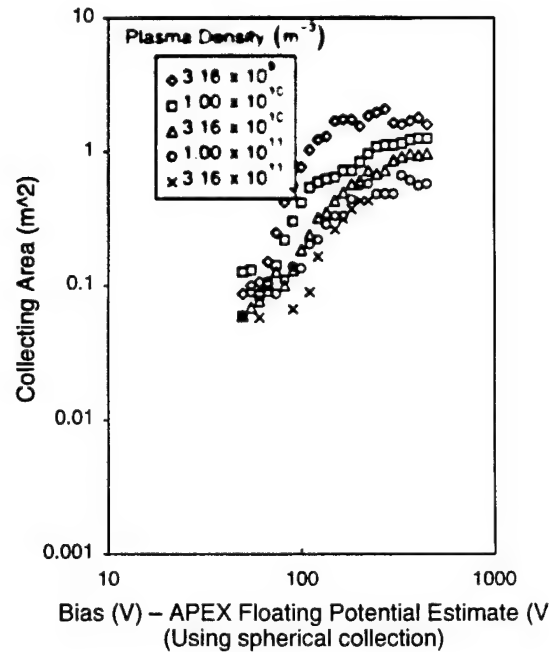


Figure 6-29. Collecting area as a function of bias minus the value of the floating potential as determined from the current, density, and temperature measurements and spherical current collection for Module 2.

6.5 Scatter in Flight Data

One surprising feature in the flight data is the amount of scatter. For the same bias, plasma density, and plasma temperature, the collected current can vary by a factor of ten in some cases. In Figure 6-13, we used averaging to smooth the data. The reason for the variation requires investigation.

Review of Data

Figures 6-30 and 6-31 show the collecting area and collected current plotted as a function of density at four specific bias values for Modules 3, 4, 5, and 11. The amount of scatter does not depend on whether the collecting area or the current is plotted. This suggests that the accuracy of the plasma density and temperature is not the dominate contribution to the scatter. The current plots make it clear that the lower limit values are a result of the precision of the current measurement. The largest variation in values is around 200 V. Above that the values are limited on the high side by the ability of APEX to collect ions. Module 5 shows much less scatter, which suggests that something important to the snapover process is responsible for the scatter.

Figures 6-32 and 6-33 show a three day portion of the Module 4 dataset. Measurements were made on days 95120, 95121, and 95129. Figure 6-32 shows data for four specific bias values, and Figure 6-33 shows data for all density and bias values. There is less scatter during this short period. Again, no trends are clear.

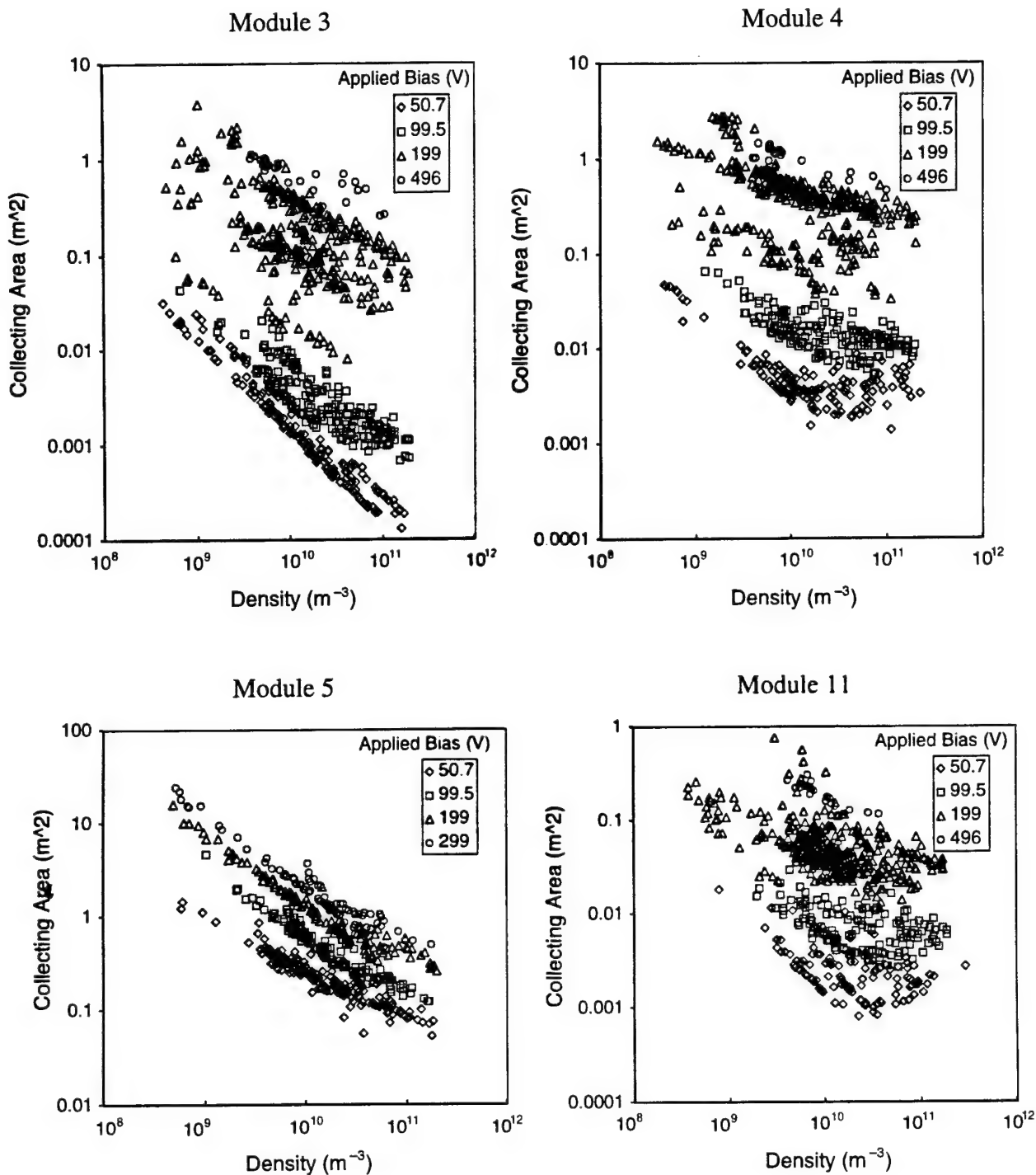


Figure 6-30. Collecting area as a function of density for 4 specific applied bias values for Modules 3, 4, 5, and 11.

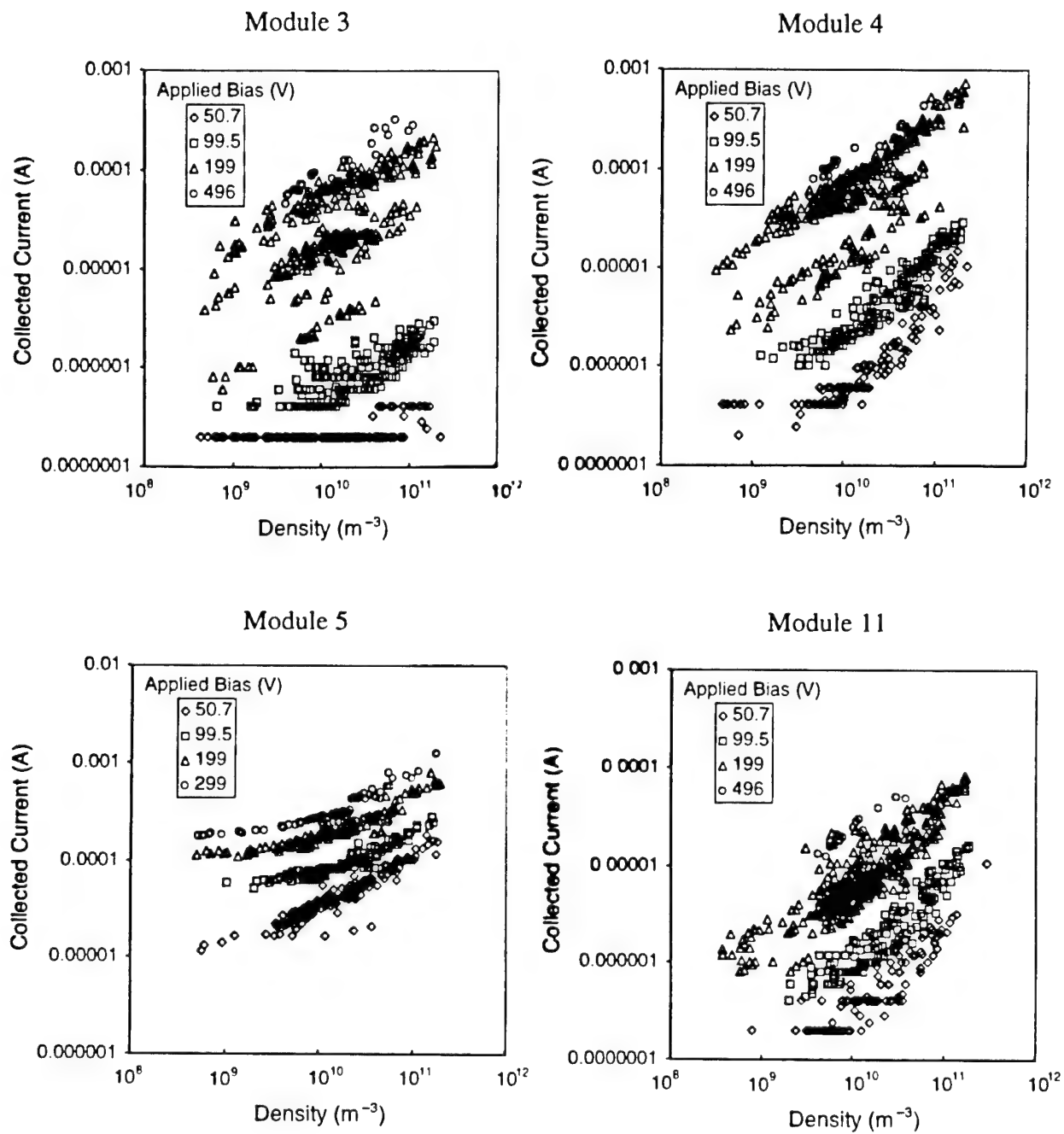


Figure 6-31. Collected current as a function of density for 4 specific applied bias values for Modules 3, 4, 5, and 11.

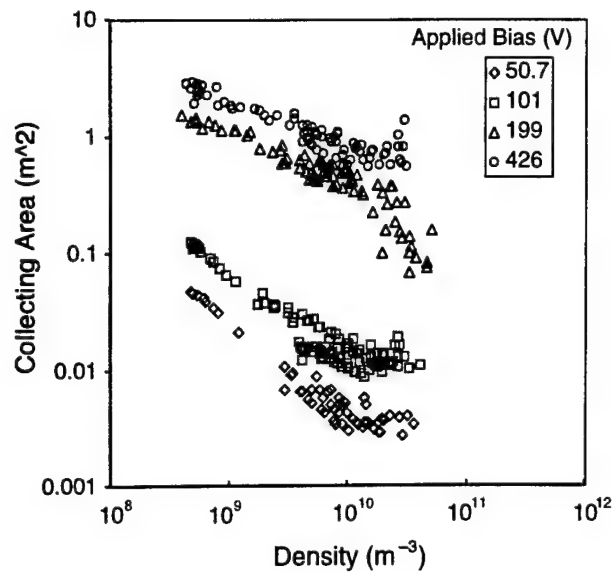


Figure 6-32. Collecting area as a function of density for 4 specific applied bias values for Module 4 from day 120 to day 129 of 1995.

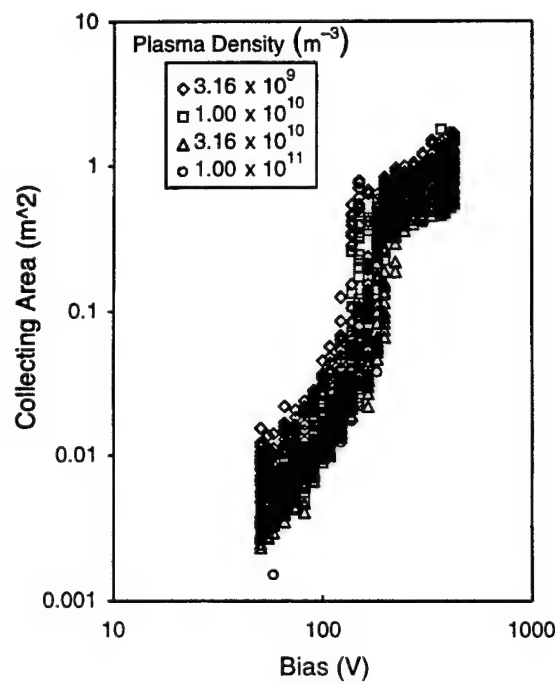


Figure 6-33. Collecting area as a function of applied bias for Module 4 from day 120 to day 129 of 1995.

We examined two specific cases for correlations between any of the measured parameters and the collected current. Case 1 is a bias value of 148 V and a density between 8×10^9 and $9.9 \times 10^9 \text{ m}^{-3}$. Case 2 is a bias value of 238 V and a density between 1.6×10^{10} and $1.99 \times 10^{10} \text{ m}^{-3}$. Tables 6-3 and 6-4 show all the examples of these two cases within the entire Module 4 dataset. The examples are ordered by the collecting area. In both cases the collecting area varies by a factor of 10. Case 1 has examples from three different data collecting periods, and all the Case 2 examples are in 1994. The ram angle values are from 70 to 90 degrees, which is where most of the data falls. The current values are ordered approximately the same as the area values as the range is small. By coincidence all the points are during periods while the spacecraft is in the sun. There is no consistent pattern to the altitude or direction (increasing or decreasing altitude) or the point in orbit (for increasing altitude = altitude and for decreasing altitude = $2500 + \text{altitude}$.) The magnetic time is the magnetic longitude expressed as a time. (360 degrees is 24 hours.) Effects associated with auroral charging might show up as a correlation with magnetic latitude. Effects associated with the south Atlantic anomaly might show up as a correlation with magnetic longitude and latitude. Twist is the orientation of APEX about its long axis. The magnetic field components in spacecraft coordinates, the magnetic field magnitude, and the angle between the magnetic field and the long axis show no ordering. The bias values of 148 V and 238 V are low enough that the charging of APEX is under the 30 V threshold of the ESAs. The panel temperature varies from 70 to 78 with no correlation for these examples. The time since the last arcing experiment and the time since the last emitter operation are an indication of the amount of contamination that might be present.

In order to examine how the floating potential might influence the scatter, we plotted the collecting area as a function of density for specific values of the potential difference between the module and the plasma. Figures 6-34 and 6-35 show the same amount of scatter as the plots that ignore the APEX floating potential.

**Table 6-3. Details of parameters for a bias value of 148 V and
a density between 8×10^9 and 9.9×10^9 , part 1 (of 3)**

| Day | Time | Bias (V) | Density (m^{-3}) | Temp (eV) | Ram Angle (degrees) | Current (μA) | Area (m^2) | Sun |
|-------|-------|-------------|-------------------------|--------------|------------------------|------------------------|-------------------|-----|
| 95129 | 44596 | 148 | 9.80E+09 | 0.297 | 88.1 | 6.76 | 0.0472 | 0 |
| 95129 | 37636 | 148 | 9.50E+09 | 0.299 | 87.4 | 7.28 | 0.0523 | 0 |
| 95129 | 44476 | 148 | 8.37E+09 | 0.307 | 86.8 | 6.60 | 0.0531 | 0 |
| 95129 | 35956 | 148 | 9.75E+09 | 0.220 | 76.9 | 6.96 | 0.0568 | 0 |
| 94221 | 18286 | 148 | 9.56E+09 | 0.259 | 88.3 | 8.00 | 0.0614 | 0 |
| 94221 | 11384 | 148 | 9.51E+09 | 0.247 | 88.3 | 8.00 | 0.0632 | 0 |
| 95129 | 43036 | 148 | 9.10E+09 | 0.217 | 76.3 | 7.36 | 0.0647 | 0 |
| 95129 | 36196 | 148 | 8.95E+09 | 0.220 | 76.5 | 9.00 | 0.0800 | 0 |
| 94298 | 45924 | 148 | 9.10E+09 | 0.095 | 79.8 | 6.28 | 0.0835 | 0 |
| 94299 | 63124 | 148 | 8.86E+09 | 0.091 | 77.1 | 7.32 | 0.1020 | 0 |
| 94300 | 31447 | 148 | 8.95E+09 | 0.119 | 86.4 | 12.8 | 0.1540 | 0 |
| 94299 | 69844 | 148 | 8.84E+09 | 0.106 | 80.6 | 12.4 | 0.1610 | 0 |
| 95120 | 75450 | 148 | 9.33E+09 | 0.265 | 85.7 | 32.0 | 0.2480 | 0 |
| 95043 | 38162 | 148 | 9.27E+09 | 0.178 | 87.1 | 30.3 | 0.2890 | 0 |
| 95060 | 19508 | 148 | 9.70E+09 | 0.235 | 77.7 | 38.9 | 0.3090 | 0 |
| 95043 | 38282 | 148 | 8.99E+09 | 0.156 | 83.9 | 34.1 | 0.3590 | 0 |
| 95060 | 19868 | 148 | 8.59E+09 | 0.295 | 75.2 | 51.6 | 0.4130 | 0 |
| 95060 | 19388 | 148 | 8.03E+09 | 0.171 | 79.0 | 37.4 | 0.4210 | 0 |
| 95052 | 49561 | 148 | 9.32E+09 | 0.274 | 85.5 | 55.2 | 0.4220 | 0 |
| 95043 | 38522 | 148 | 8.33E+09 | 0.148 | 77.4 | 36.6 | 0.4260 | 0 |
| 95043 | 38642 | 148 | 8.68E+09 | 0.143 | 74.3 | 38.1 | 0.4330 | 0 |
| 95053 | 18390 | 148 | 8.46E+09 | 0.288 | 85.8 | 57.0 | 0.4680 | 0 |

Sources of Scatter

There are a multitude of sources of scatter and no single one appears to be large enough to explain the factor of 10 scatter seen. The following sections discuss the possible sources of scatter.

Measurement of Collected Current

The measurement of the collected current is only made with a finite precision. This measurement is then telemetered back to earth introducing another possible source of precision reduction. The applied bias is different from the actual bias and varies slightly from measurement to measurement. While no experimental apparatus is perfect, the measurement of current is routine.

**Table 6-3. Details of parameters for a bias value of 148 V and
a density between 8×10^9 and 9.9×10^9 , part 2 (of 3)**

| Altitude (km) | Direction | Point in Orbit (km) | Velocity (m/s) | Mag. time (hours) | Mag. lat. (degrees) | Mag. lon. (degrees) | Scat. pos. (km) |
|------------------|-----------|------------------------|-------------------|----------------------|------------------------|------------------------|--------------------|
| 1970 | up | 1970 | 6670 | 16.5 | -16.7 | -52.1 | 1.21 |
| 1910 | up | 1910 | 6730 | 16.5 | -22.3 | -49.3 | 1.21 |
| 1870 | up | 1870 | 6760 | 16.3 | -21.6 | -46.4 | 1.21 |
| 472 | up | 472 | 8100 | 7.23 | -54.7 | 42.8 | 1.61 |
| 741 | | 741 | 7820 | 6.7 | -26.8 | 49.9 | 0.818 |
| 737 | | 737 | 7820 | 6.82 | -31.5 | 50 | 0.62 |
| 579 | up | 579 | 7990 | 8.92 | -60.5 | 31.1 | 1.62 |
| 610 | up | 610 | 7960 | 8.82 | -65.6 | 27.3 | 1.61 |
| 909 | | 909 | 7650 | 4.87 | 9.55 | -107 | 1.41 |
| 748 | up | 748 | 7810 | 4.73 | 6.37 | -98.9 | 1.61 |
| 1150 | down | 3700 | 7420 | 4.31 | -1.75 | -123 | 2.01 |
| 901 | down | 3451 | 7660 | 4.53 | -7.42 | -109 | 1.69 |
| 733 | down | 3283 | 7820 | 6.8 | -7.67 | 100 | 0.818 |
| 2080 | down | 4630 | 6580 | 20.7 | -11.1 | 129 | 1.61 |
| 967 | up | 967 | 7590 | 5.67 | 10.4 | -69.7 | 1.41 |
| 1990 | down | 4540 | 6660 | 20.8 | -15.9 | 133 | 1.81 |
| 1320 | up | 1320 | 7260 | 6.44 | 27.8 | -50.1 | 1.41 |
| 856 | up | 856 | 7700 | 5.42 | 4.18 | -76.5 | 1.41 |
| 1190 | up | 1190 | 7380 | 7.34 | 37.6 | -41.5 | 1.63 |
| 1790 | down | 4340 | 6840 | 21.2 | -25.8 | 144 | 1.81 |
| 1680 | down | 4230 | 6930 | 21.4 | -30.8 | 150 | 1.81 |
| 1310 | up | 1310 | 7270 | 7.9 | 28.6 | -38.5 | 1.63 |

This experiment is a part of the primary mission of this spacecraft. For these reasons, we believe that this provides a negligible contribution to the scatter in the data.

Measurement of Plasma Density and Temperature

The ability of the Langmuir probe to accurately measure plasma density and temperature is addressed in Section 6-1. We estimate that the plasma density and temperature assigned to a specific collected current measurement are accurate to 20 percent.

Table 6-3. Details of parameters for a bias value of 148 V and a density between 8×10^9 and 9.9×10^9 , part 3 (of 3)

| MagFld-x (Gauss) | MagFld-y (Gauss) | MagFld-z (Gauss) | MagFld-v (Gauss) | Mag Angle (degrees) | ESA (V) | Panel Temperature (°C) | Days Since Emitter | Days since Arcing |
|---------------------|---------------------|---------------------|---------------------|------------------------|------------|------------------------------|--------------------------|-------------------------|
| 0.0853 | 0.1290 | 0.0571 | 0.1649 | 81.6 | 0 | 74 | long | 21 |
| 0.0945 | 0.1680 | 0.0393 | 0.1967 | 86.4 | 0 | 74 | long | 21 |
| 0.0960 | 0.1450 | 0.0208 | 0.1751 | 91.3 | 0 | 73 | long | 21 |
| 0.0624 | -0.2530 | -0.1180 | 0.2861 | 134 | 0 | 74 | long | 21 |
| 0.0358 | -0.2090 | -0.0507 | 0.2180 | 76.8 | 0 | 71 | recent | none |
| 0.0305 | -0.2680 | -0.0560 | 0.2755 | 76.9 | 0 | 72 | recent | none |
| 0.1250 | -0.1870 | -0.2100 | 0.3077 | 127 | 0 | 74 | long | 21 |
| 0.1000 | -0.1920 | -0.2250 | 0.3122 | 127 | 0 | 74 | long | 21 |
| -0.0014 | 0.2423 | 0.214 | 0.2152 | 18.7 | 0 | 75 | 8 | 3 |
| -0.0024 | -0.0011 | 0.2440 | 0.2440 | 27 | 0 | 76 | 9 | 4 |
| -0.0628 | -0.0787 | 0.1290 | 0.1636 | 31.9 | 0 | 76 | 10 | 5 |
| -0.0757 | -0.1400 | 0.2060 | 0.2603 | 20.4 | 0 | 76 | 9 | 4 |
| 0.0936 | 0.0267 | 0.2540 | 0.2720 | 142 | 0 | 73 | long | 12 |
| -0.0880 | 0.0910 | 0.0939 | 0.1576 | 118 | 0 | 75 | long | 1 |
| -0.0509 | 0.0939 | 0.1680 | 0.1991 | 49.7 | 0 | 77 | long | 18 |
| -0.1130 | 0.1120 | 0.0681 | 0.1731 | 109 | 0 | 75 | long | 1 |
| -0.0250 | 0.2090 | 0.0062 | 0.2106 | 82.3 | 0 | 76 | long | 18 |
| -0.0684 | 0.0208 | 0.1910 | 0.2039 | 40.1 | 0 | 76 | long | 18 |
| -0.0978 | 0.2360 | -0.1080 | 0.2774 | 104 | 0 | 76 | long | 10 |
| -0.1640 | 0.1380 | -0.0085 | 0.2145 | 92.3 | 0 | 75 | long | 1 |
| -0.1870 | 0.1380 | -0.0567 | 0.2392 | 85.3 | 0 | 75 | long | 1 |
| -0.0956 | 0.2130 | -0.0649 | 0.2423 | 94.2 | 0 | 77 | long | 11 |

Variation of APEX Floating Potential

Many factors can influence the APEX floating potential. Primary among them are array module bias and plasma density. Since the scatter is between measurements with the same bias and density, the contribution of these factors can be ignored.

Photoemission influences the floating potential of spacecraft by providing an additional source of current. If the spacecraft is negative, the photoelectrons leave, reducing the potential. At altitudes above geosynchronous, photoemission is often the dominant current and charges spacecraft slightly positive. However, photoemission only provides a significant current below plasma densities of $3 \times 10^9 \text{ m}^{-3}$. We know this because the photoelectrons are seen by the Langmuir

Table 6-4. Details of parameters for a bias value of 238 V and a density between 1.6×10^{10} and 1.99×10^{10} , part 1 (of 3)

| PAY | Time | Bias (V) | Density (m^{-2}) | Temp (eV) | Ram Angle (degrees) | Current (fA) | Area (m^{-2}) | Sum |
|-------|-------|----------|----------------------|-----------|---------------------|--------------|-------------------|-----|
| 94284 | 76562 | 238 | 1.82E+10 | 0.302 | 87.4 | 18.6 | 0.0694 | 0 |
| 94285 | 59114 | 238 | 1.84E+10 | 0.281 | 86.3 | 18.6 | 0.0712 | 0 |
| 94223 | 45423 | 238 | 1.94E+10 | 0.287 | 85.3 | 20.0 | 0.0721 | 0 |
| 94284 | 83282 | 238 | 1.76E+10 | 0.290 | 83.8 | 20.4 | 0.0804 | 0 |
| 94223 | 73019 | 238 | 1.75E+10 | 0.284 | 85.0 | 22.2 | 0.0890 | 0 |
| 94222 | 69750 | 238 | 1.83E+10 | 0.281 | 86.0 | 29.7 | 0.1150 | 0 |
| 94222 | 48685 | 238 | 1.90E+10 | 0.284 | 85.3 | 41.7 | 0.1540 | 0 |
| 94302 | 3427 | 238 | 1.75E+10 | 0.132 | 88.9 | 63.8 | 0.3740 | 0 |
| 94301 | 14479 | 238 | 1.84E+10 | 0.101 | 76.4 | 64.7 | 0.4140 | 0 |
| 94301 | 21199 | 238 | 1.86E+10 | 0.094 | 80.4 | 68.9 | 0.4510 | 0 |
| 94301 | 7759 | 238 | 1.78E+10 | 0.110 | 72.8 | 71.4 | 0.4520 | 0 |
| 94301 | 71586 | 238 | 1.63E+10 | 0.287 | 75.3 | 112 | 0.4780 | 0 |
| 94301 | 23719 | 238 | 1.78E+10 | 0.284 | 85.3 | 125 | 0.4910 | 0 |
| 94301 | 62932 | 238 | 1.68E+10 | 0.094 | 72.3 | 67.3 | 0.4910 | 0 |
| 94302 | 13027 | 238 | 1.61E+10 | 0.299 | 80.4 | 122 | 0.5180 | 0 |
| 94301 | 30439 | 238 | 1.68E+10 | 0.261 | 81.3 | 122 | 0.5310 | 0 |
| 94302 | 19747 | 238 | 1.61E+10 | 0.274 | 76.2 | 121 | 0.5360 | 0 |
| 94301 | 69666 | 238 | 1.65E+10 | 0.077 | 75.8 | 69.1 | 0.5620 | 0 |
| 94300 | 59709 | 238 | 1.64E+10 | 0.107 | 72.6 | 84.9 | 0.5890 | 0 |
| 94301 | 42201 | 238 | 1.99E+10 | 0.095 | 73.4 | 103 | 0.6240 | 0 |

probe at the lower densities and because typical published values give current densities on the order of a few times 10^{-5} A m^{-2} .

The power solar arrays operate at different biases at different times. Generally, the arrays operate at 36 V and provide trickle charging to the battery. After leaving a long duration eclipse, the arrays are cold and the battery has been partially discharged. Under these conditions the array bias can reach 72 V. However, these conditions occur rarely.

At different orientations with respect to the ram, APEX collects different amounts of ion current. Calculations suggest that the ion current variation is under 30 percent. Sorting the data by ram angle does not appear to reduce the scatter. Variation for this reason would be reduced if the flight data were sorted by ram angle.

Table 6-4. Details of parameters for a bias value of 238 V and a density between 1.6×10^{10} and 1.99×10^{10} , part 2 (of 3)

| Altitude (km) | Direction | Point in Orbit (km) | Velocity (m/s) | Mag Time (hours) | Mag Lat (degrees) | Twist (degrees) | Sensit (V) |
|------------------|-----------|------------------------|-------------------|---------------------|----------------------|--------------------|---------------|
| 873 | down | 3423 | 7690 | 7.47 | 10.9 | -80.8 | 0.818 |
| 871 | down | 3421 | 7690 | 7.27 | 22 | -81.8 | 0.818 |
| 676 | up | 676 | 7890 | 6.3 | -8.06 | 58.1 | 1.02 |
| 1040 | down | 3590 | 7530 | 7.29 | -1.48 | -90.1 | 0.818 |
| 682 | up | 682 | 7880 | 6.78 | -25.7 | 58.4 | 1.42 |
| 676 | up | 676 | 7890 | 7 | -23.7 | 57.2 | 1.61 |
| 444 | up | 444 | 8130 | 5.8 | 12.3 | 78.8 | 1.41 |
| 1160 | down | 3710 | 7410 | 3.42 | -17.5 | -125 | 2.6 |
| 703 | down | 3253 | 7860 | 4.8 | 16.4 | -98.7 | 2.4 |
| 851 | down | 3401 | 7710 | 4.53 | 11.5 | -108 | 2.6 |
| 576 | down | 3126 | 7990 | 5.1 | 20.9 | -88.4 | 2.6 |
| 1060 | up | 1060 | 7510 | 15.1 | 44.7 | 21.5 | 2.69 |
| 1450 | up | 1450 | 7140 | 16 | 4.21 | 41.2 | 3 |
| 565 | down | 3115 | 8000 | 4.58 | 19.1 | -88.8 | 1.93 |
| 1320 | up | 1320 | 7260 | 15.3 | 16.4 | 34 | 2.11 |
| 1270 | up | 1270 | 7300 | 15.9 | 11.8 | 32.6 | 2.01 |
| 1150 | up | 1150 | 7430 | 15.2 | 20.9 | 25.1 | 2.35 |
| 678 | | 678 | 7880 | 4.43 | 5.73 | -98.5 | 2.61 |
| 562 | down | 3112 | 8000 | 4.76 | 23.1 | -86.2 | 3.19 |
| 596 | | 596 | 7970 | 4.73 | 30.8 | -91.2 | 3.05 |

The spacecraft velocity also influences the ion current collected. APEX velocity varies from 6000 to 8000 km s⁻¹.

The dominant ion species has an important influence on the ion current collected. As hydrogen is much lighter than oxygen, the thermal velocity of hydrogen is higher than the thermal velocity of oxygen. Hydrogen is not excluded from the wake region and has a higher thermal current. Therefore, when everything else is the same, a hydrogen plasma provides a higher ion current than an oxygen plasma. Therefore, the APEX floating potential is less negative in a hydrogen plasma.

Table 6-4. Details of parameters for a bias value of 238 V and a density between 1.6×10^{10} and 1.99×10^{10} , part 3 (of 3)

| MagFld1 (Gauss) | MagFld1 (Gauss) | MagFld2 (Gauss) | MagFld (Gauss) | Mag Angl (degrees) | ESA (%) | Panel Temperature (°C) | Day Since Emitter | Fly since Arrive |
|--------------------|--------------------|--------------------|-------------------|-----------------------|------------|------------------------------|-------------------------|------------------------|
| -0.0783 | 0.0646 | 0.2300 | 0.2514 | 51.2 | 0 | 74 | recent | 38 |
| -0.0653 | 0.1390 | 0.1950 | 0.2482 | 68.6 | 0 | 75 | recent | 39 |
| 0.0851 | -0.1580 | 0.1220 | 0.2170 | 134 | 0 | 71 | recent | none |
| -0.0451 | -0.0572 | 0.2410 | 0.2518 | 12.7 | 0 | 74 | recent | 38 |
| 0.0994 | -0.3350 | 0.0263 | 0.3504 | 102 | 0 | 71 | recent | none |
| 0.1260 | -0.3060 | 0.0275 | 0.3321 | 104 | 0 | 72 | none | none |
| 0.1060 | 0.0771 | 0.1410 | 0.1925 | 132 | 0 | 70 | none | none |
| -0.1350 | -0.1410 | 0.0180 | 0.1960 | 75.1 | 0 | 75 | 13 | 7 |
| -0.0436 | 0.0236 | 0.2330 | 0.2382 | 29.5 | 0 | 76 | 12 | 6 |
| -0.0956 | -0.0150 | 0.1700 | 0.1956 | 13.6 | 0 | 76 | 12 | 6 |
| 0.0300 | 0.1840 | 0.2390 | 0.3031 | 73.7 | 0 | 76 | 12 | 6 |
| -0.1780 | -0.1870 | -0.1720 | 0.3102 | 53.2 | 0 | 78 | 12 | 6 |
| -0.0959 | -0.1230 | 0.1300 | 0.2030 | 121 | 0 | 76 | 12 | 6 |
| 0.0461 | 0.1630 | 0.2230 | 0.2800 | 73.7 | 0 | 76 | 12 | 6 |
| -0.1450 | -0.1320 | 0.0415 | 0.2004 | 95.6 | 0 | 75 | 13 | 7 |
| -0.1470 | -0.1900 | 0.0532 | 0.2460 | 90 | 0 | 77 | 12 | 6 |
| -0.1740 | -0.1840 | -0.0245 | 0.2544 | 72.7 | 0 | 74 | 13 | 7 |
| -0.0180 | 0.0378 | 0.2780 | 0.2811 | 34.5 | 0 | 76 | 12 | 6 |
| 0.0574 | 0.1860 | 0.2020 | 0.2805 | 81.9 | 0 | 76 | 11 | 5 |
| 0.0883 | 0.2270 | 0.2080 | 0.3203 | 84.1 | 0 | 77 | 12 | 6 |

The best argument against the floating potential being a dominate source of scatter is the fact that when an estimated floating potential is used to adjust the applied bias values, the amount of scatter is not reduced.

Variation of Insulator Potentials

The current collected by the array modules varies as the insulator potentials vary. The insulator potentials can vary from near zero to negative five times the electron temperature.

Photoemission, dominant ion species, orientation with respect to the ram, and spacecraft velocity all influence the insulator potentials. At small potentials this is a major effect. A barrier to electron collection exists whenever the average surface potential on the module is negative. A

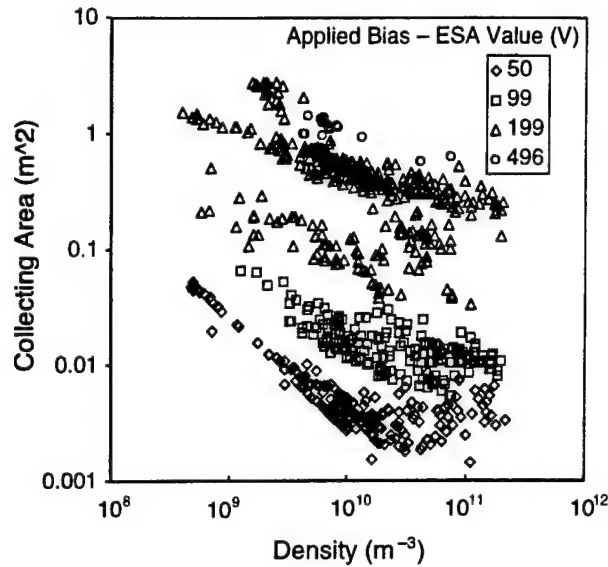


Figure 6-34. Collecting area as a function of density for specific values of bias minus the value of the floating potential as determined from the ESA measurement for Module 4.

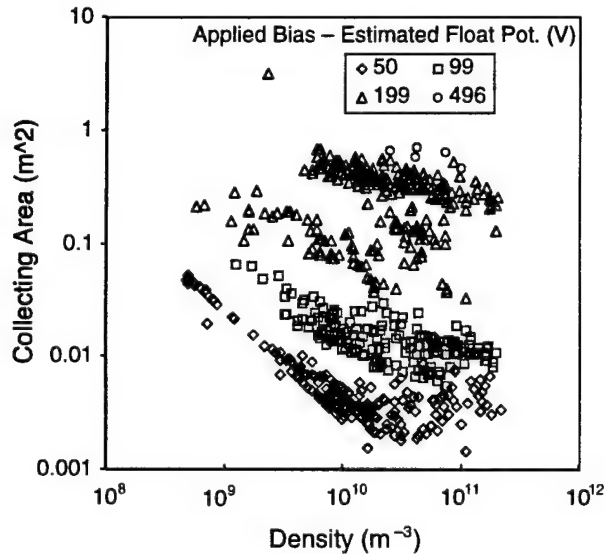


Figure 6-35. Collecting area as a function of density for specific values of bias minus the value of the floating potential as determined from the current, density, and temperature measurements and spherical current collection for Module 4.

barrier to collection can also exist whenever the average potential on the entire spacecraft panel is negative. By 50 V, this effect is negligible.

Variation of Surface Properties with Time on Orbit

Outgassing, ultra-violet exposure, debris and meteoroid impact and other processes can change the properties of surfaces exposed to the space environment. Changes in the secondary electron properties or the conductivity of the surfaces of the modules affect the parasitic current collection. Such changes in the modules are of scientific interest. The full data set shown in Section 6-2 is expected to show such changes. If the variation in surface properties over time were the cause of the scatter in the data, the results would show a systematic variation with time. This does not appear to be the case.

Attitude

We do not expect the attitude to be important as all of the measurements analyzed are for the modules facing the ram direction. Sorting the data by ram angle does not reduce the scatter.

Contamination

The sources of contamination are arc discharges, emitter operation, and being charged. There is no correlation with recent discharges or emitter operation. Spacecraft charging related contamination would show up as a correlation with longitude and latitude, present ESA measured ground potential, and recent high levels of ESA activity. None of these are seen in the data.

Charging and Discharging Related Effects

We examined the ESA activity level for a 1 hour period prior to each of the examples shown in the tables. There was a wide range of activity levels, both localized to a few energy channels and across the spectrum. There is no correlation that we could discern.

We also examined the current sweeps. Figure 6-36 shows the sweeps for Case 1. The legend indicates the order of the lines in Table 6-3. Some of the most extreme lines are in the middle of the ordering.

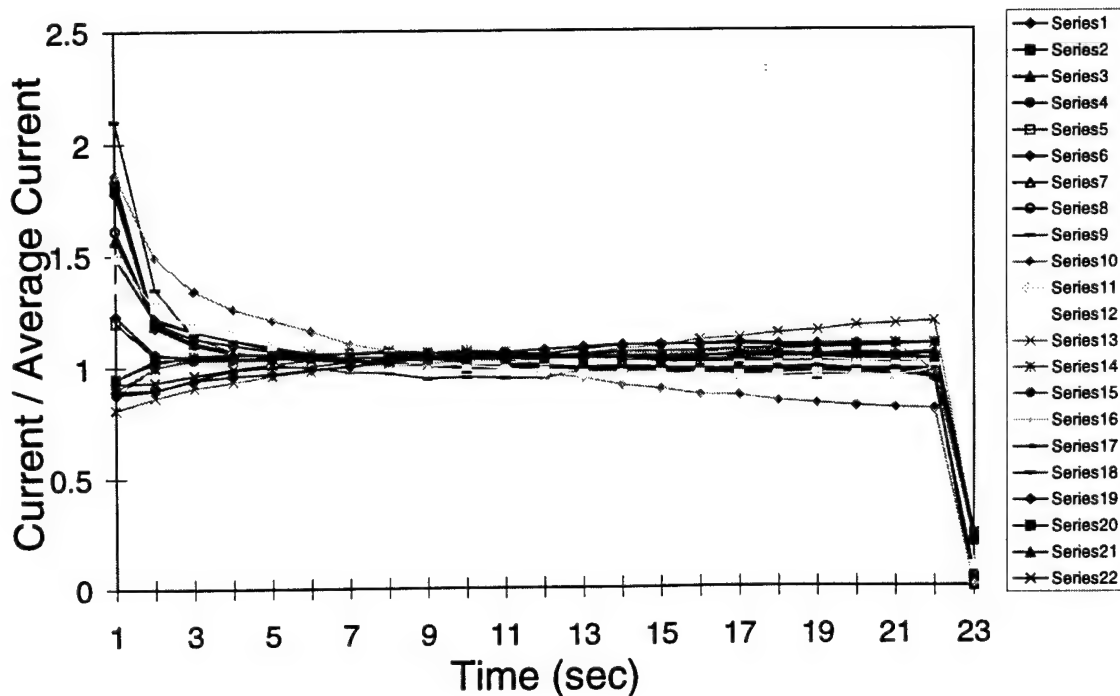


Figure 6-36. Current sweeps for Case 1. The legend indicates the order of the lines in Table 6-3.

Magnetic Field

Magnetic field effects on current collection would be expected to influence the results for large sheaths. However no correlation can be seen either in the magnitude or direction of the magnetic field.

Unstable/Bistable Nature of Snapover

The current collected depends on the amount of the surface that is snapped over. As the conditions of snapped over and not snapped over are both stable, each portion of the module may be snapped over or not. In the laboratory, under apparently non-varying conditions, the current has been seen to jump suddenly at the same time as a visual glow assumed to be associated with snapover moves on the surface. (Ref. 6-1) One argument against this being a significant contribution to the scatter seen in the flight data is that the current is usually stable for the 23 second period during which a measurement is made.

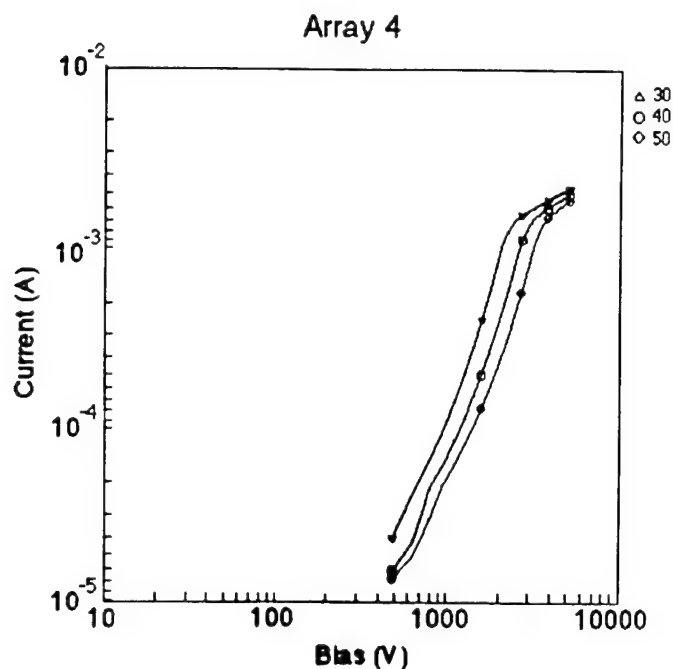


Figure 6-37. Calculated current as a function of applied bias for three different first crossover values.

Surface Temperature

The first crossover of the secondary yield curve, and therefore the amount of snapover, would be expected to vary with surface temperature. During the mission, the panel temperature varies a great deal. However, during the current collection experiments the panel temperature only varies from 71°C to 77°C and the variation is not correlated with the variation in collecting area.

Summary

A final item to consider here is how much scatter in the value of the first crossover potential it would take to create the observed scatter in collecting area. Figure 6-37 shows the calculated current as a function of applied bias for three different first crossover values. The difference between the top and bottom curves is approximately the width of the measured curves. A 20 V scatter in first crossover values would explain the scatter in the flight data.

The reason for the wide variation in the flight data remains unexplained at present. It is possible that the variation in ion species is creating an important variation in collected current due to its influence on the APEX floating potential. It is possible that there are many different widely

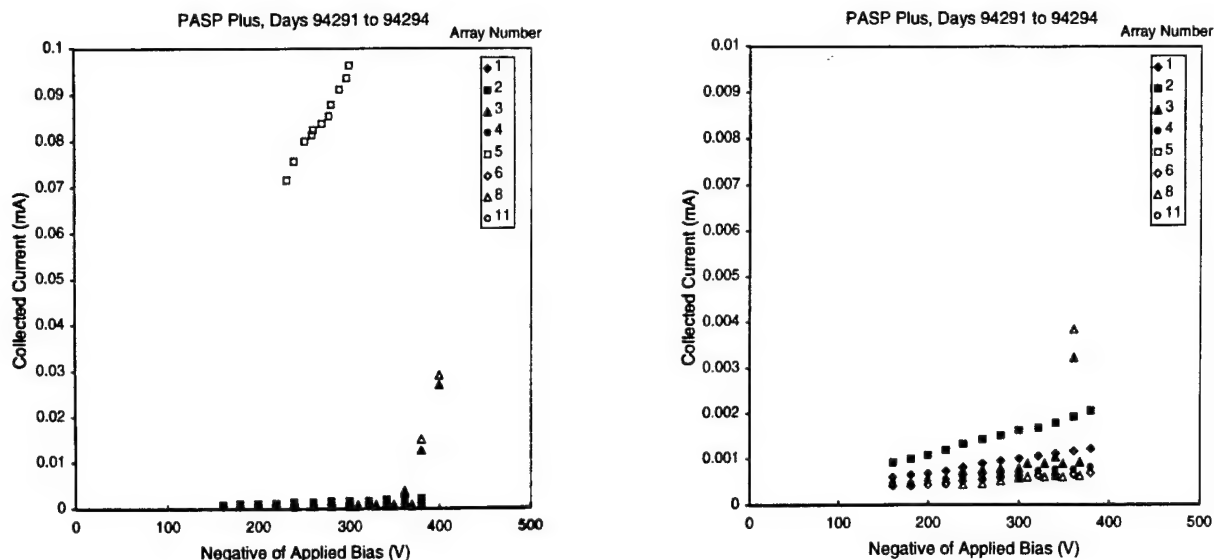


Figure 6-38. Collected current as a function of applied bias for negative bias for days 94291 to 94294. The same data is shown twice at different scales.

varying currents that are physically consistent with each bias potential and plasma condition. It is possible that a number of effects are affecting the first crossover and surface conditions and therefore the current collected. It is most likely that another parameter that is presently not being held constant accounts for the variation.

6.6 Current Collection Under Negative Bias

We examined the current collection characteristics of the modules when they were biased negatively. This work was primarily motivated by a desire to learn the surface conductivity of the Germanium on the surface of Module 5 so that this conductivity could be subtracted from the apparent current collected to obtain the current collected from the surrounding plasma.

We examined the leakage current for three time periods: days 291 to 294 of 1994, days 80 to 89 of 1995, and days 190 to 196 of 1995. On these days, the modules were biased negatively and any arcing was examined. Here we are concerned with the leakage current measurements. We averaged all the measurements taken at a given applied bias during each of these periods. Figures 6-38 to 6-40 shows the collected current as a function of applied bias for all the modules for the three periods.

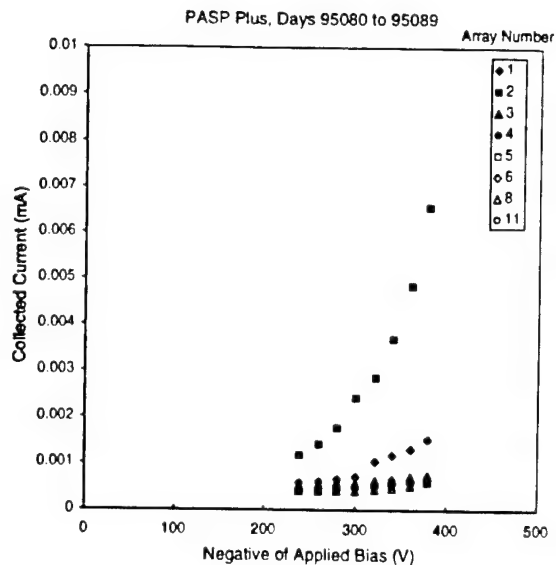
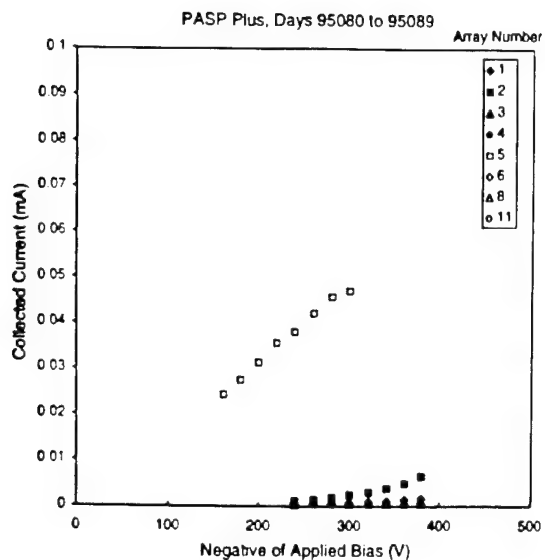


Figure 6-39. Collected current as a function of applied bias for negative bias for days 95080 to 95089.

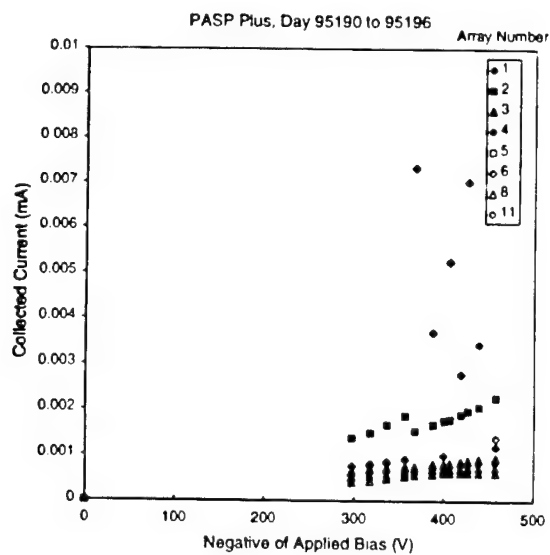


Figure 6-40. Collected current as a function of applied bias for negative bias for days 95190 to 95196.

Table 6-5. Current Voltage Linear Characteristic Days 94291 to 94294

| Module # | Slope (1/M Ω) | Resistance (M Ω) | Intercept (μ A) | Quality of Fit |
|----------|-----------------------|--------------------------|----------------------|----------------|
| 1 | 0.0029 | 351 | 0.13 | 1.00 |
| 2 | 0.0051 | 197 | 0.09 | 1.00 |
| 3 | 0.0020 | 508 | 0.25 | 0.77 |
| 4 | 0.0017 | 603 | 0.19 | 0.99 |
| 5 | 0.3223 | 3 | -2.20 | 0.98 |
| 6 | 0.0013 | 745 | 0.18 | 0.96 |
| 8 | 0.0015 | 648 | 0.08 | 0.89 |
| 11 | 0.0014 | 736 | 0.17 | 0.94 |

Table 6-6. Current Voltage Linear Characteristic Days 95080 to 95089

| Module # | Slope (1/M Ω) | Resistance (M Ω) | Intercept (μ A) | Quality of Fit |
|----------|-----------------------|--------------------------|----------------------|----------------|
| 1 | 0.0070 | 143 | -1.24 | 0.94 |
| 2 | 0.0360 | 28 | -8.10 | 0.91 |
| 3 | 0.0016 | 625 | 0.11 | 0.97 |
| 4 | 0.0020 | 502 | -0.06 | 0.98 |
| 5 | 0.1706 | 6 | -2.74 | 0.99 |
| 6 | 0.0015 | 654 | 0.01 | 0.91 |
| 8 | 0.0012 | 828 | 0.08 | 0.78 |
| 11 | 0.0014 | 690 | 0.03 | 0.95 |

Table 6-7. Current Voltage Linear Characteristic Days 95290 to 95296

| Module # | Slope (1/M Ω) | Resistance (M Ω) | Intercept (μ A) | Quality of Fit |
|----------|-----------------------|--------------------------|----------------------|----------------|
| 1 | 0.0026 | 382 | -0.02 | 0.99 |
| 2 | 0.0045 | 223 | 0.05 | 0.80 |
| 3 | 0.0018 | 559 | 0.12 | 0.99 |
| 4 | 0.0016 | 619 | 0.09 | 0.99 |
| 6 | 0.0021 | 483 | -0.08 | 0.21 |
| 8 | 0.0015 | 686 | 0.00 | 0.89 |
| 11 | 0.0015 | 677 | 0.02 | 0.95 |

Most of the modules show a predominately straight line current-voltage characteristic. Tables 6-5 through 6-7 show the slope and intercept for a least square fit line to each module for each time period, ignoring dramatic excursions. Excepting Module 5 and Modules 1 and 2 at the middle time, the resistance varies by a factor of four from 200 to 850 M Ω . Excepting Module 5 and Modules 1 and 2 at the middle time, the intercept is always under 0.3 μ A.

As many of these measurements were made in the wake or under low plasma density conditions, we can initially postulate that these measurements are of surface currents and internal resistances. The higher current measurements, except Module 5, are presumed to be when the modules are in the ram and at higher plasma densities.

We can compare these measurements with those made on array modules similar to the APSA array module at NASA/LeRC. (Ref. 6-2) For the APSA module without the carbon loaded Kapton blanket, the resistance was over 600 M Ω . For the APSA module with the carbon loaded Kapton blanket, the resistance was approximately 1 M Ω . For the APSA module without the carbon loaded Kapton blanket and with a Germanium coating, the resistance was approximately 150 M Ω . This last design is that flown on PASP Plus.

6.7 The APSA Array Module

Module 5 (sometimes known as Module 36) shows a different collected current-applied bias relation than the rest of the modules. This is because it is coated with a layer of Germanium, which is a semi-conductor. The measured current is enhanced due to the fact that current is conducted through the Germanium coating even in the absence of plasma. This parasitic current is linear with the applied bias with a resistance of 3 M Ω as described in Section 6-6. Current is also collected from the plasma. This current is comparable to the current collected by an module with a low first crossover potential. Figure 6-41 shows the effective circuit. Current is collected across the entire surface of the module.

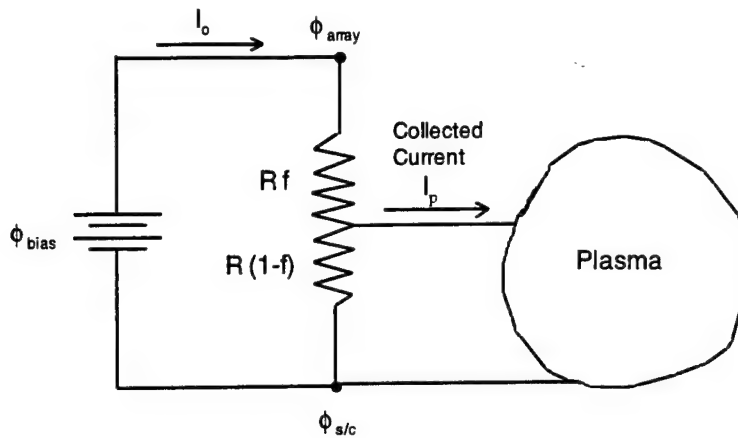


Figure 6-41. Effective circuit for collection of current by Module 5.

The measured current I_o is given by the following:

$$I_o = (1 - f) I_p + \frac{\phi_{bias}}{R} \quad (6-14)$$

The fraction f is used to account for the fact that electrons are collected by the entire surface and not just at the module potential.

In Section 6-6, we determined that the resistance varied between the values of $3 \text{ M}\Omega$ and $5 \text{ M}\Omega$ over a four month period. In order to get a better handle on the value of resistance we need another technique. We examined the measured current during positive biasing as a function of applied bias for Module 5 when the measured plasma density was below $2 \times 10^9 \text{ m}^{-3}$ and the modules were in the wake. These are the conditions under which the ambient plasma contributed least. Figure 6-42 shows the current divided by the bias for these conditions over the entire mission. If the resistance was $3 \text{ M}\Omega$ and the plasma did not contribute at all, the points would form a horizontal line at 0.33 on the graph. Extra current appears to be present. If we assume that the minimum value of the current divided by the bias is constant over the mission, we can estimate the variation of the resistance.

When we subtract the internal current from the measured current we get the collecting area curves shown in Figure 6-43. These curves can be compared with similar curves in Figure 6-13.

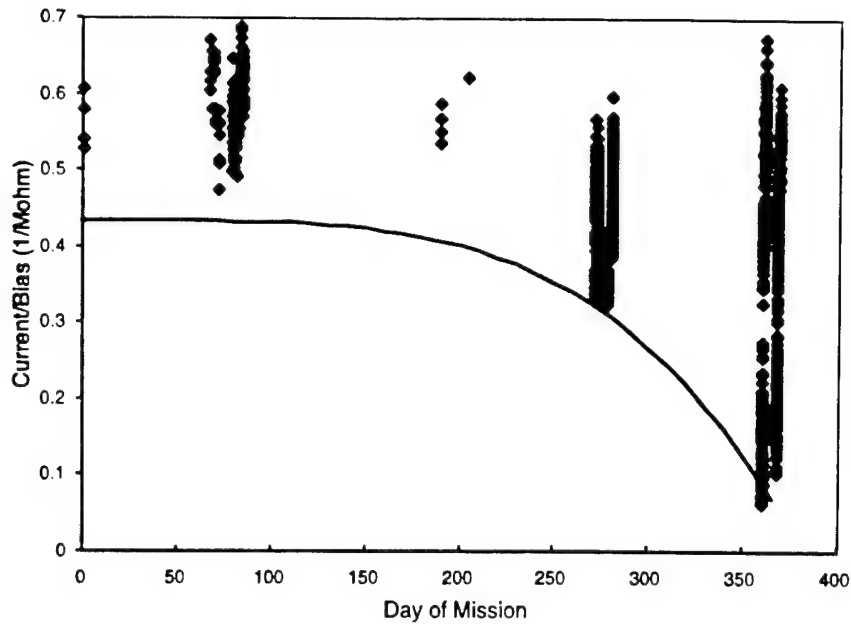


Figure 6-42. Current divided by applied bias for Module 5 during positive biasing when the measured plasma density is under 2×10^9 and the array modules are in the wake for the entire mission. The line is

$$\frac{I}{\phi} = 0.1 + 0.33 \left(1 - (0.0028 \text{ day})^4 \right).$$

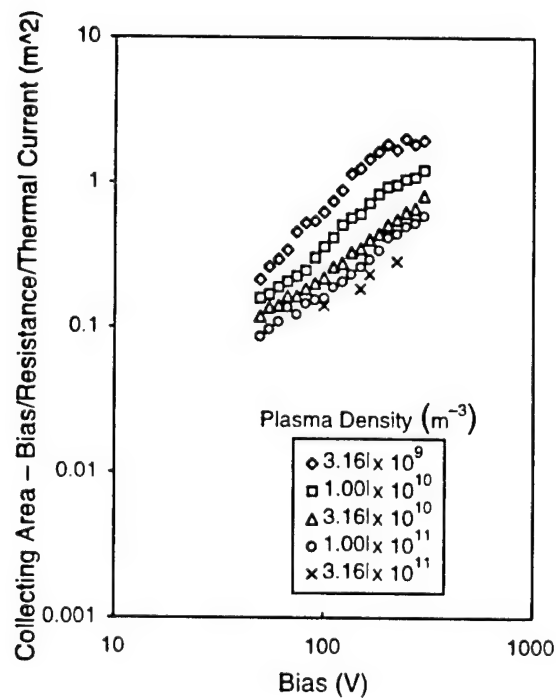


Figure 6-43. Collecting area as a function of bias for Module 5, accounting for internal resistance.

References for Chapter 6

- 6-1. Personal Communication, Dale Ferguson, NASA Lewis Research Center.
- 6-2. G. B. Hillard, "Plasma Chamber Testing of APSA coupons for the SAMPIE Flight Experiment," AIAA Paper, AIAA-93-0568, 1993.

Chapter 7

Comparison of Electron Current Collection by Space Station Solar Arrays as Measured by SAMPIE and PASP Plus

D.C. Ferguson, NASA/Lewis Research Center

SAMPIE, the Solar Array Module Plasma Interactions Experiment, flew in the payload bay of STS-62 in March 1994. As part of an extensive set of samples flown, a four-cell coupon of the solar array to be used on the International Space Station was included, and the electron currents it collected from the ambient plasma were measured at various bias levels. Here these measurements are compared with those from the nearly identical PASP Plus array Module 3. The data are analyzed in the light of Langmuir probe measurements of the payload bay plasma densities and temperatures. The appropriate conclusions are drawn regarding the International Space Station (ISS).

7.1 Background

The current collected from space plasmas by spacecraft solar arrays determines not only the parasitic current power drain on the electrical system, but also helps determine the potential at which the spacecraft floats relative to the surrounding plasma. As a general rule, spacecraft with negative power system grounds and solar arrays with exposed cell interconnects may float up to 90 percent of the solar array string voltage negative of the plasma they are immersed in. This is because the net current to the spacecraft from the plasma must be zero, and the low mass electrons are easily collected at low positive potentials to balance the (comparatively heavy) ion current collected at high negative potentials (Ref. 7-1). It was determined during the Space Station Freedom Electrical Grounding Tiger Team activity that the Space Station would float up to 140 V negative of the plasma surrounding it, because of its 160 V solar array string voltage (Ref. 7-2). Laboratory tests showed that typical Space Station surface dielectrics would break down at such high negative potentials, leading to high current arcs, surface disruption, and thermal control problems (Ref. 7-3).

As a result of the Tiger Team recommendations, a plasma contactor was added to the ISS baseline design. The plasma contactor, by creating a low resistance plasma contact with the surrounding plasma, acts as a potential control device, effectively pegging the ISS structure to the space plasma potential. However, it does so by emitting electrons to balance the electrons collected from the space plasma by ISS solar arrays.

One critical parameter of the plasma contactor is the current of electrons it must emit to balance that collected by the solar arrays. Failing to emit enough electrons, the plasma contactor would allow the ISS floating potential to become highly negative of the space plasma, negating its usefulness. If correctly designed, so that it emits enough electrons to balance those collected by the arrays under all plasma conditions, the plasma contactor would always prevent arcing and its deleterious effects. Thus, the current collected by the ISS solar arrays under worst case conditions must be known, to allow correct plasma contactor design and operation.

In addition to having the largest string voltage of any array used in space, the ISS array also has a new design, with no cell interconnects exposed to the plasma. It is mounted on a flexible substrate, and the inter-cell connections are made through copper traces imbedded in the substrate and welded to the backs of the solar cells. Thus, the only exposed electrical conductor on the solar cells is at the cell edges. The cells are covered with coverglasses, to protect against radiation damage, and the coverglasses extend an average of 0.0089 cm (0.0035 inch) beyond the cell edges (Ref. 7-4). We call this the coverglass overhang. The cells are closely spaced on the flexible Kapton substrate, with only about 0.081 cm (0.032 inch) separation between adjacent cells (on average), a quantity we call the cell gap (Ref. 7-4).

Initial laboratory testing of the ISS solar arrays in ground test plasma facilities seemed to show that the cells would collect very little current from a simulated space plasma (Ref. 7-5). It was determined through computer modeling that this initial testing was adversely affected by abnormally high electron temperatures, compared to those expected in the low Earth environment (LEO) through which ISS must fly (Ref. 7-6). Entry of the plasma electrons to the cell edges was effectively choked off in those tests by potential barriers that formed over the cell gaps. The same computer models predicted that the electron current would dramatically increase if a more representative electron temperature (0.2 eV, instead of about 1 eV) could be obtained in ground

tests. Further ground tests, performed by the Tiger Team, showed that in 0.2 eV electron plasmas, the cells collected much more current, verifying the validity of the Tiger Team concerns (Ref. 7-7). However, the computer models were uncertain about the dependence of the currents on the plasma temperatures and cell parameters. The ground tests, while convincingly showing that the currents collected could be quite high, were not performed in a flowing plasma such as one obtains in LEO, and the ion species was xenon, rather than the oxygen ions that dominate in LEO. A space test was deemed necessary.

7.2 SAMPIE

Samples of ISS-type cells were flown in space on the Solar Array Module Plasma Interactions Experiment (SAMPIE). Details about SAMPIE may be obtained from the Technical Requirements Document (Ref. 7-8) and other summaries. SAMPIE was a Hitchhiker-M experiment in the payload bay of the Space Shuttle Columbia. It was launched on March 4, 1994, into a 39 degree inclination orbit, which, during the SAMPIE experiment operation reported here, had an apogee of 310 km and a perigee of 300 km. Many hours of current collection and arcing data were obtained during the two week flight of STS-62. Plasma conditions were monitored by a Langmuir probe and a V-body (vehicle potential monitor) probe mounted an appropriate distance from the samples being biased.

The main emphasis of this chapter is data collected by a four cell array coupon of ISS design nearly identical to PASP Plus Module 3. As may be seen in Figure 7-1, the coupon was attached to an experiment plate, mounted near the center of the MPSS and facing upward, out of the Shuttle payload bay. The four cell coupon (Figure 7-2) was loaded with a 1 Ω resistor, and the entire circuit was biased to varying voltages with respect to the Shuttle Orbiter (Ref. 7-9).

Currents collected were measured with a variable range electrometer, sampled at narrowly spaced intervals, digitized and recorded on solid state memory. After the flight, the memory was read out into computer files, which were used for analysis.

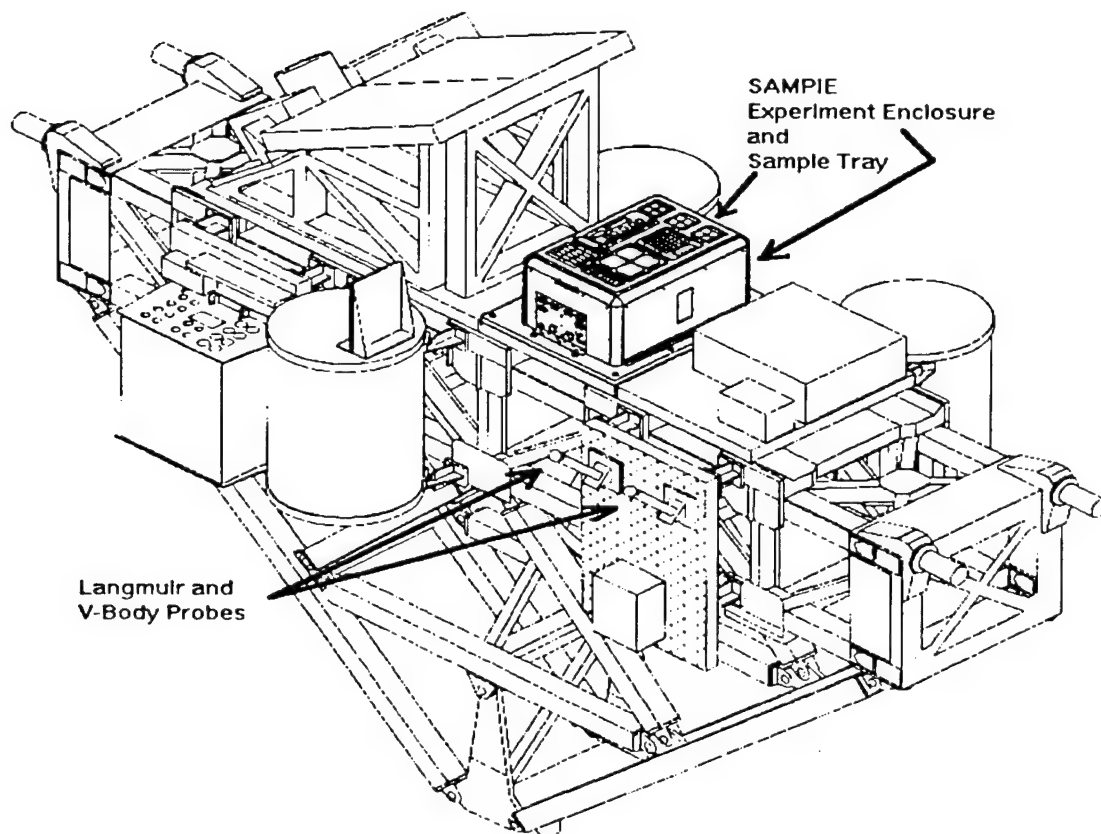


Figure 7-1. SAMPIE's position on Shuttle Columbia's MPRESS carrier.

Another set of experimental samples of ISS interest was flown. It consisted of coupons of quartered ISS cells, modified to collect different amounts of current, and butted against each other to simulate adjacent solar cells. One parameter varied on these cells was the coverglass overhang, and another parameter was the amount of cell edge exposed to the plasma. Overhangs of 0, 4, 7, and 11 mils (all ± 3 mils) were tested on one coupon. On another coupon, cell edge adhesive was removed to leave 0, 8, 16, and 32 mils of cell edge exposed to the plasma, respectively. It was expected that the cells with less overhang or more adhesive removed would collect more current from the plasma at identical bias voltages, because the electron paths from plasma to cell edge would be more easily negotiated. Results from these samples are intended to verify predictions of in-house computer models for current collection.

SAMPIE obtained data in three different Shuttle orientations, bay-to-earth, bay-to-ram, and bay-to-wake. The ISS samples were not tested in the bay-to-wake orientation, since it was expected that the very low plasma densities in the Shuttle wake would lead to very low current collection,

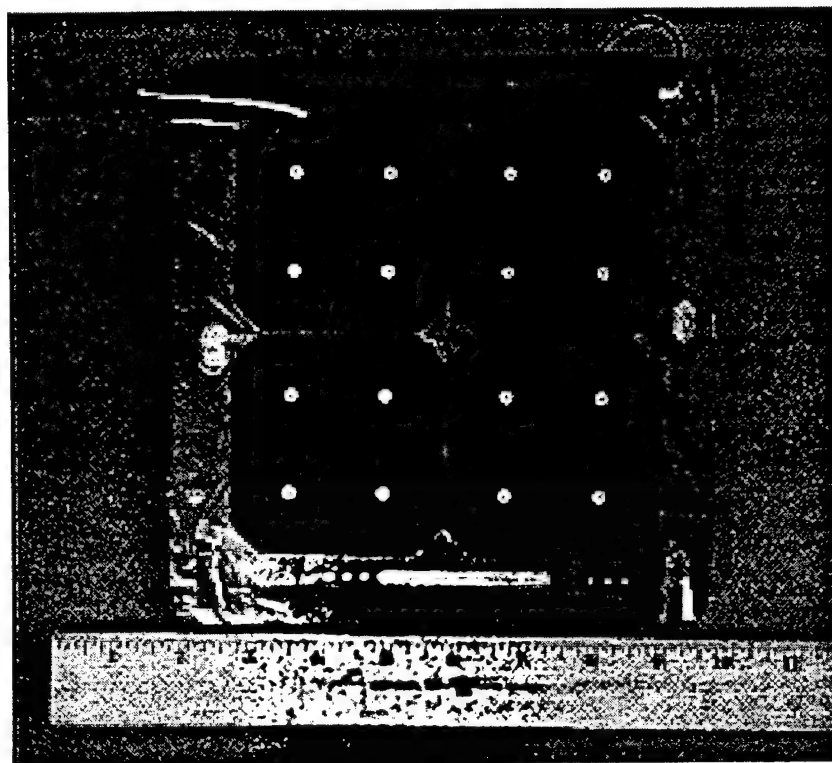


Figure 7-2. SAMPIE 4-cell Space Station solar array.

and would shed no additional light on the worst-case current collection conditions. Of the remaining orientations, the bay-to-ram was clearly the most severe, and only the bay-to-ram results are presented here.

In Figure 7-3 are shown the raw currents collected, versus bias voltage, by the 4-cell ISS coupon. Since the plasma thermal current density varies directly as the plasma density and as the half power of the electron temperature, these raw currents were divided by the electron thermal current density to produce Figure 7-4. In this figure, the currents are represented as effective areas from which thermal current was collected. Noteworthy here is the fact that at bias voltages greater than about 200 V, the effective collecting area is greater than the physical area of the array of cells (256 cm^2), indicating that at these high potentials, the cells collect large amounts of current, indeed. At bias voltages less than the string voltage of the entire Space Station (160 V) however, the effective area is well less than the array area, indicating that the cell edges are acting as independent plasma current collectors, and giving us some hope of extrapolating the SAMPIE results to the larger problem of the $>1000 \text{ m}^2$ ISS solar arrays.

Space Station Currents, Bay-to-Ram

Experiments 20 and 1

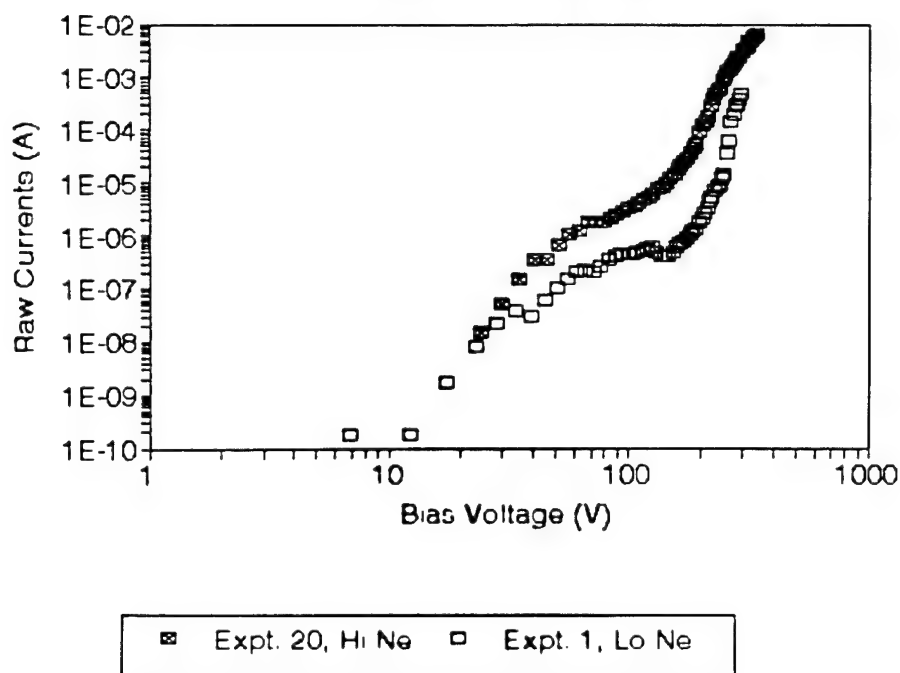


Figure 7-3. Plasma electron currents collected by Space Station 4 cell array.
Raw data, uncorrected for plasma density and temperature.

The plasma density when experiment 20-2 was done was about a factor of ten higher than when Experiment 1-4 was done. Since it is the electron collection of ISS arrays under high plasma densities that are of concern for the ISS plasma contactor maximum current output, we will hereafter concentrate on Experiment 20-2.

In Figure 7-5 are shown predictions of models and ground tests to compare with the SAMPIE data. Here are shown the results of models incorporated into EWB (Environment Workbench) (at ram and 90 degree plasma incidence) and the results of the Tiger Team Tank Test (T^4) under a simulated space plasma (Ref. 7-10). It is not surprising that the EWB model at 90 degrees incidence (thermal) agree well with the T^4 results, because the T^4 results served as the validation basis for the EWB models. What is surprising is that the ram EWB predictions overestimate the SAMPIE results to the degree shown. Furthermore, the EWB predictions underestimate the space collection at very high bias voltages, because they underestimate the importance of "snapover,"

Space Station Currents, Bay-to-Ram

Experiments 20 and 1

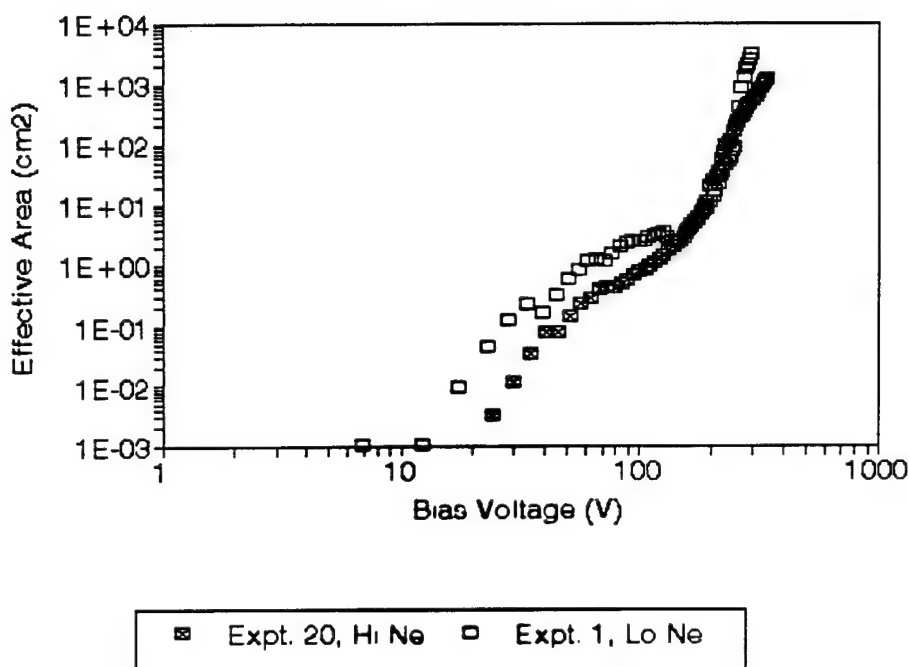


Figure 7-4. Effective electron current collection areas (cm²) for Space Station 4-cell array, corrected for plasma densities and temperatures.

abnormally high current collection caused by the collapse of surface charge on surrounding insulators.

7.3 Comparison with PASP Plus Results

The four cell coupon of ISS array flown on SAMPIE and PASP Plus Module 3 are identical insofar as the cell parameters are concerned. The PASP Plus coupon was, however, not mounted flat on an experiment plate. Rather, it was mounted with both sides exposed to the plasma and a spring-loaded mechanism holding the flexible substrate reasonably taut.

In Figure 7-6 are shown one day's results on current collection by the PASP Plus Module 3 (Ref. 7-11). These currents are similar to those measured on SAMPIE, except that the measured plasma densities on PASP Plus were an order of magnitude or more lower than the SAMPIE plasma densities. When converted to effective areas, the PASP Plus data show much greater effective collecting areas than do the SAMPIE data, and even higher areas than the EWB ram

Predicted SAMPIE Collection Area

$$T_e = 0.15 \text{ eV}$$

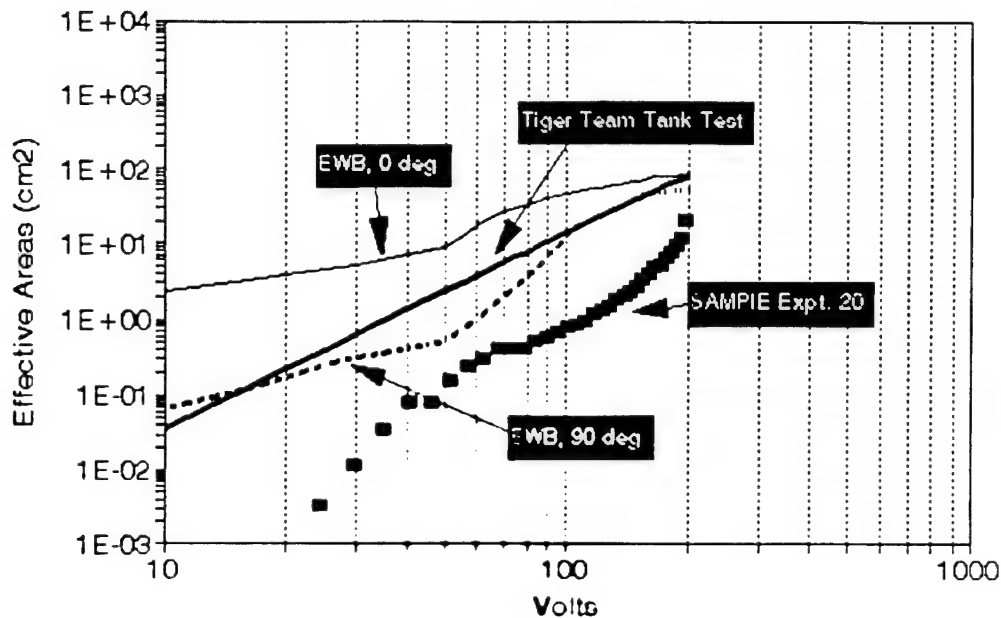


Figure 7-5. Predictions of electron collection area (cm^2) of SAMPIE experiment 20 array, from EWB and the Tiger Team.

predictions. It is highly unusual for two such similar coupons as those on SAMPIE and PASP Plus to give such different results for electron current collection.

7.4 Comparisons with SAMPIE Modified ISS Cells

Some light may be shed on ISS current collection by analysis of the currents collected by the modified ISS coupons on SAMPIE. Here, we only treat currents measured at a bias voltage of +100 V, but results at other voltages are similar. In Figure 7-7 are shown currents collected at 100 V with varied cell coverglass overhang (Ref. 7-12). Because the errors on production of different overhangs were ± 3 mils, only the general trend is significant. Here it can be seen that for very low values of the overhang, the current (normalized to four cells) is similar to that found by PASP Plus, showing that if the SAMPIE 4-cell coupon had had no coverglass overhang, the difference with PASP Plus would be minimized. However, it is known that there were no significant differences between overhangs on SAMPIE and PASP Plus 4-cell coupons.

PASP+ Collection Area (daytime)

08/18/94-08/19/94

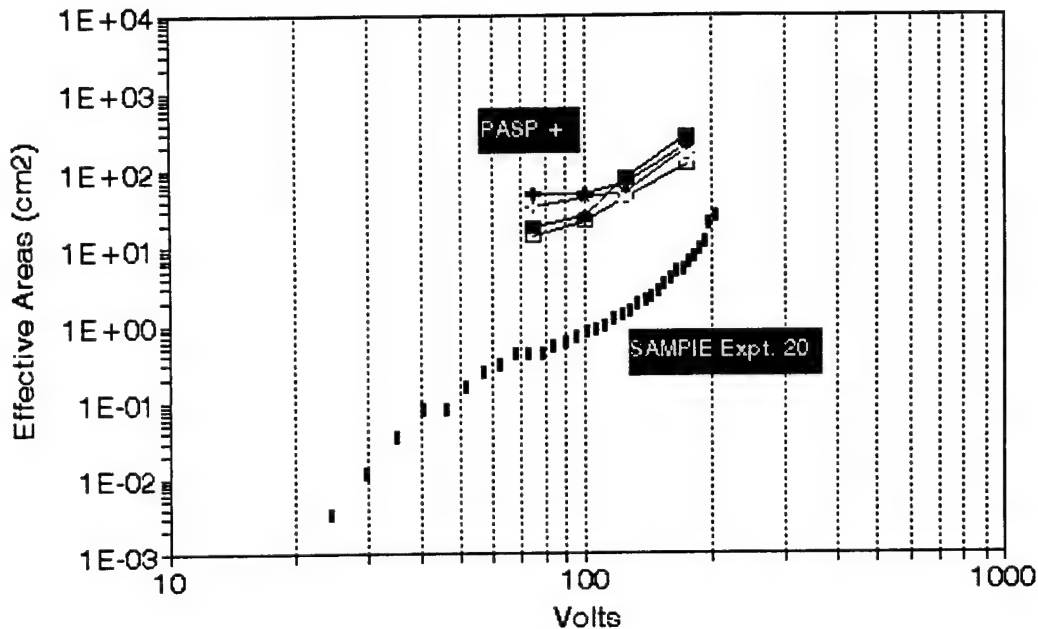


Figure 7-6. Effective collection area (cm^2) of the PASP Plus Space Station 4-cell array, compared to that of SAMPIE experiment 20.

In Figure 7-8 is shown the SAMPIE results on cells modified to have varying amounts of cell edge adhesive removed (Ref. 7-13). Again, with large amounts of exposed cell edge, the SAMPIE results approach the effective areas of PASP Plus. Again, however, there is no reason to believe the SAMPIE cells had a different cell edge adhesive coverage than those on PASP Plus. However, what both of the modified cell experiments are saying is that the more the cell edges see an unimpeded electron flow from the surrounding plasma, the larger are the collected currents. It is a fair hypothesis to ascribe the differences between SAMPIE and PASP Plus to the flexible array backing on PASP Plus. If the PASP Plus cell edges have pulled away from the flexible substrate at the coupon perimeter, they would collect much more current than if flattened down to a plate as on SAMPIE. Furthermore, during PASP Plus vibration testing, it was remarked that one edge of the flexible backing had pulled out of its guide slot, and there was a noticeable gap between the Kapton and the cell edges for at least two of the cells (Ref. 7-14).

SAMPIE - Modified Overhangs

100 V Currents Normalized to 4 Cells

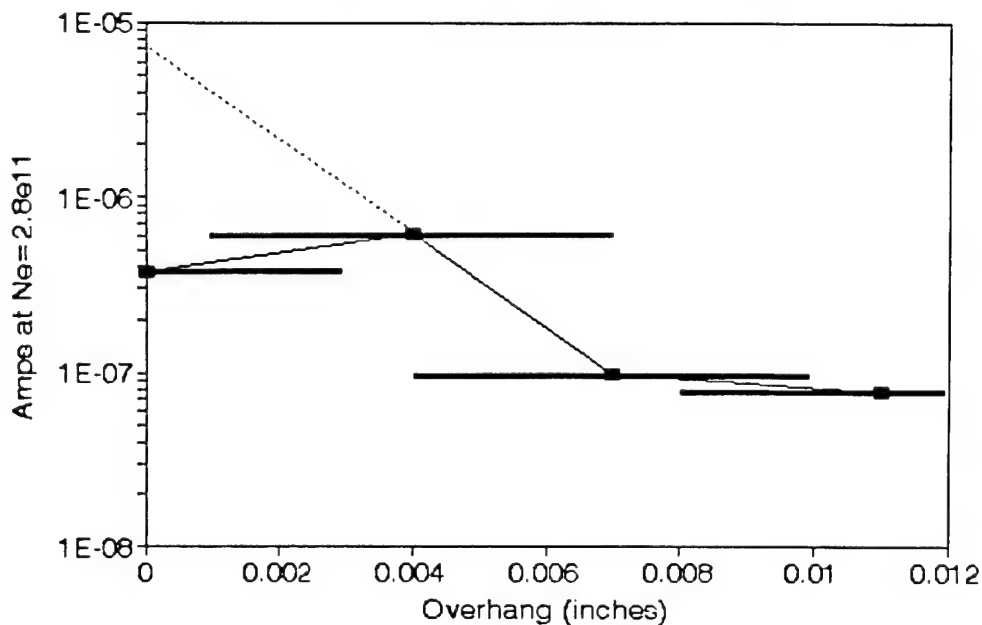


Figure 7-7. Electron currents at 100 V by the SAMPIE modified Space Station cells, normalized to a 4-cell edge length and a plasma density of $2.8 \times 10^{11} \text{ cm}^{-3}$, vs. coverglass overhangs.

7.5 Conclusions

What, then, can one conclude about the current collection of the solar arrays on ISS? It will be intermediate between those extrapolated from SAMPIE and PASP Plus. The extra current collection from outside cell edges on a flexible substrate depends on the number of outside edges. On PASP Plus, fully half of the cell edges were on the outside, and could collect extra current. On the large arrays of ISS, a 40×10 array panel pair of 400 cells has about 100 outside cell edges and 1500 inside cell edges, so only 1/16 of the edges are on the outside. Thus, proportionately, the extra outside edge cell collection, which dominates the PASP Plus results, will only be 1/8 as great on ISS. This will lower ISS collection from that extrapolated by PASP Plus to about 1/8 its value, or about three times the value extrapolated from the SAMPIE results. This is shown in Figure 7-9. Without the PASP Plus results, the current required by the ISS plasma contactor would be underestimated.

SAMPIE - Adhesive Removed

100 V Currents Normalized to 4 Cells

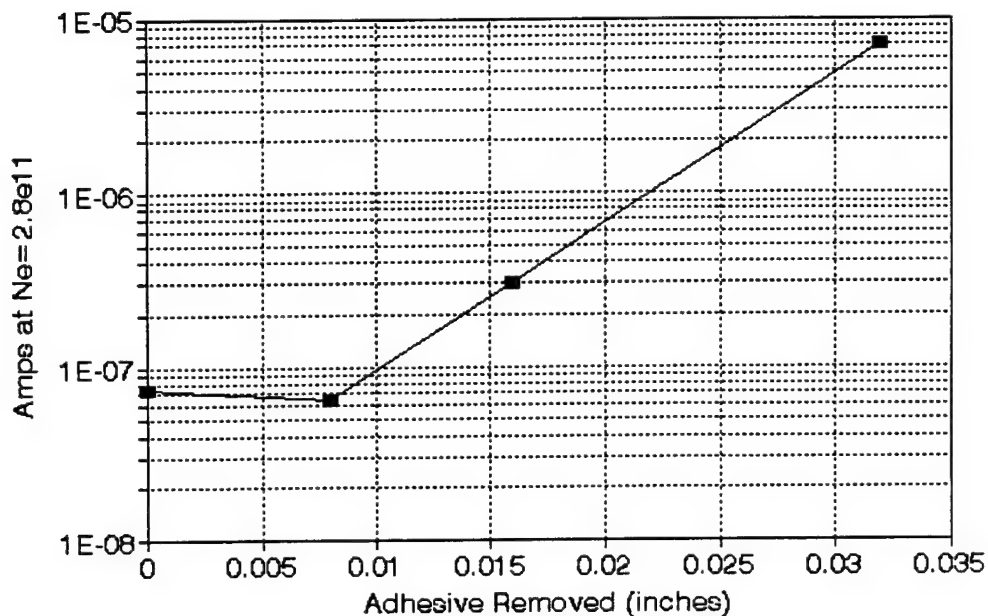


Figure 7-8. Electron currents collected at 100 V by modified Space Station cells, Figure 7-8 normalized to 4-cell edge length and a plasma density of $2.8 \times 10^{11} \text{ cm}^{-3}$, for different values of the length of cell edge adhesive removed.

Of course, the hypothesis that PASP Plus collected more current than SAMPIE because of outside cell edge effects is just that, a hypothesis, made plausible by the SAMPIE modified cell edge results. It is being tested in ground test plasma chambers at the NASA Lewis Research Center. However, new physical and numerical models of current collection at ISS cell edges have shown some success with the flat SAMPIE cells (Ref. 7-15) and with the pulled-away PASP Plus cells (Ref. 7-16), lending further credence to the zeroth order hypothesis.

4 Cell Space Station Collection

Expected From SAMPIE and PASP +

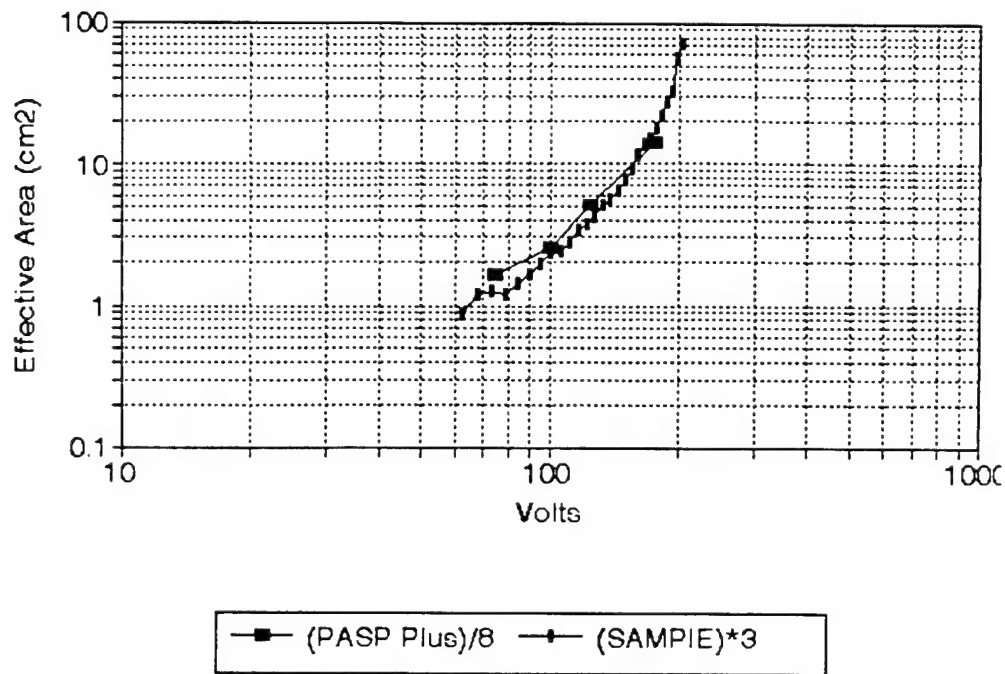


Figure 7-9. Expected 4-cell effective electron collection area for Space Station cells, based on a hypothesis for enhanced edge collection. This may be extrapolated to the 196,800 cells on the International Space Station.

References for Chapter 7

- 7-1. Ferguson, D.C., "Interactions Between Spacecraft and Their Environments," AIAA Paper 93-0705, 1993.
- 7-2. Ferguson, D.C., Snyder, D.B., and Carruth, R., "Findings of the Joint Workshop on Evaluation of Impacts of Space Station Freedom Grounding Configurations," NASA TM-103717, 1990.
- 7-3. Snyder, D.B., Minutes of the Space Station Freedom Electrical Grounding Tiger Team Meeting, Memphis, Tennessee, January 29-31, 1992.
- 7-4. Ferguson, D.C. and Chock, R., "Floating Potentials of Space Station Freedom with Present and Modified Solar Cell Designs: Analysis of Current Collection by SSF Solar Cells," 1991, unpublished.

- 7-5. Felder, M.C., "PV Plasma Interaction Test: Preliminary Results and Status," *Final Report of the Joint Workshop on Evaluation of Impacts of Space Station Freedom Grounding Configurations*, Ferguson, Snyder, and Carruth, eds., NASA LeRC, August 21, 1990.
- 7-6. Chock, R.C., "NASCAP/LEO Simulations, SSF Solar Cell Geometries," *Minutes of the Electrical Grounding Tiger Team Meeting*, May 14-17, 1991, Boeing Trade Zone, Huntsville, Alabama, 1991.
- 7-7. Felder, M.C., Sater, B.L., Paulsen, P.E., Thompson, D., and Olsafsky, R., "Results of Testing Conducted in Tank 5 for Interactions Between Space Station Freedom and Plasma," PIR#268, NASA LeRC, January 22, 1993.
- 7-8. Hillard, G.B. and Ferguson, D.C., "The SAMPIE Flight Experiment Final Technical Requirements Document," NASA TM-106224, 1993.
- 7-9. Bozich, R.C., "Characterization of Solar Cells and Metal Samples in a Plasma Atmosphere Using the SAMPIE Proto-type Model System," M.S. Thesis, Cleveland State University, March 1994.
- 7-10. Environments WorkBench version 3.0, S-Cubed Division of Maxwell Labs, 1994.
- 7-11. PASP Plus August 1994 GSE data, courtesy of D. Guidice, Phillips Laboratory, Hanscom AFB, Massachusetts, 1994.
- 7-13. SAMPIE data, to be published.
- 7-14. Personal Communication, M. Piszczor, NASA Lewis Research Center.
- 7-15. Morton, T.L., "Models of Plasma Sheath Formation Near Surfaces in Space," *Bulletin of the American Physical Society*, Vol. 39, No. 7, page 1530, November 1994.
- 7-16. Davis, V. and Gardner, B., *Parasitic Current Collection by Solar Cells in LEO*, AIAA Paper 95-0594, 1995.

Chapter 8

Dosimeter Results

Capt. K. P. Ray, Phillips Laboratory, Hanscom AFB

Radiation belt models are used extensively in satellite mission planning. The NASA AP8 and AE8 models are commonly used to predict proton and electron fluences respectively, for a given orbit. The Combined Release and Radiation Effects Satellite (CRRES), flying recently in solar maximum, provided data to update the NASA models. However, both the NASA models and the CRRES models have inadequate spatial and temporal resolution at altitudes less than 1000 km, where missions such as the space station take place. One goal of the PASP Plus space radiation dosimeter on the APEX satellite was to improve models of the inner edge of the radiation belt.

The PASP Plus space radiation dosimeter on the APEX satellite has nearly identical characteristics to those on DMSP F7 (Ref. 8-1) and CRRES (Ref. 8-2). Modifications were made to the PASP Plus dosimeter to account for the harsher radiation environment on APEX and to better separate contributions from electrons and protons. On APEX, the thickest dome was replaced with a thin plate for detector 1 to measure dose from the lower energy proton populations (> 5 MeV) that degrades solar cells. A summary of the PASP Plus dosimeter characteristics used in this paper is given in Table 8-1.

For each shielding thickness the energy deposited is measured over two energy ranges: 50 keV to 1 MeV called low linear energy transfer (LOLET) and 1 MeV to 10 MeV called high linear energy transfer (HILET). In addition, the HILET detector threshold is separated into HILET A, 1 MeV to 3 MeV, and HILET B, 3 MeV to 10 MeV. Two of the channels, 1 and 2, have two detectors each, designated as A and B. Detectors 1A and 1B are shielded by a 4.3 mils flat aluminum plate while detectors 2A and 2B, 3, and 4 are shielded by aluminum hemispheres that are 82.5, 232.5 and 457.5 mils thick respectively. Contributors to the LOLET dose for the four detectors are $>.15$, >1 , >2.5 , and >5 MeV electrons respectively. Contributors to the HILET dose for the four detectors are from protons with energies 5 to 80, 20 to 115, 35 to 120, and 52 to 125 MeV respectively. Finally, each of the detectors has a very high linear energy transfer

Table 8-1. APEX Dosimeter Characteristics

| Detector | | Aluminum Shields | | External Energy Thresholds | | | |
|----------|-------------------------|---|------------|----------------------------|--------------------|--------------------|---------------------|
| Number | Area (cm ²) | Density (gm/cm ³) (mils AL) | Shape | Electron LOLET (MeV) | Proton HILET (MeV) | Proton VHLET (MeV) | Proton HILETB (MeV) |
| 1A | 0.008 | 0.0294 (4.3) | Flat | 0.150 | 5-80 | 40 | 6-22 |
| 1B | 0.051 | 0.0294 (4.3) | Flat | 0.150 | 5-80 | 40 | 6-22 |
| 2A | 0.008 | 0.57 (82.5) | Hemisphere | 1.0 | 20-115 | 46 | 20-35 |
| 2B | 0.051 | 0.57 (82.5) | Hemisphere | 1.0 | 20-115 | 46 | 20-35 |
| 3 | 0.051 | 1.59 (232.5) | Hemisphere | 2.5 | 35-120 | 56 | 35-47 |
| 4 | 1.00 | 3.14 (457.5) | Hemisphere | 5.0 | 52-125 | 96 | 52-60 |

All detectors approximately 400 microns thick

LOLET detector thresholds 0.05 to 1.0 MeV

HILET detector thresholds 1.0 to 10.0 MeV

HILET-B detector thresholds 3.0 to 10.0 MeV

(VHLET) channel. Counts in the VHLET channels are caused by nuclear interactions. VHLET counts have been correlated with Single Event Upset (SEU) rates seen on CRRES (Ref. 8-3).

Figure 8-1 is a plot of successive APEX orbits taken over a 12 hour period in B and L space. The orbits are superimposed on the CRRES total dose map for a hemispherical aluminum dome shield of thickness 232.5 mils. The plot was made using the CRRESRAD utility (Ref. 8-4).

Figure 8-1 illustrates two points. First, the bin sizes used for the CRRES model, while decreasing in size as one moves in to low altitudes, are crude for orbits that skim the inner edges of the radiation belts. Second, the APEX orbit gives excellent coverage of the inner edge of the inner radiation belt. Thus dose models for the inner belt can be improved using the PASP Plus dosimeter data.

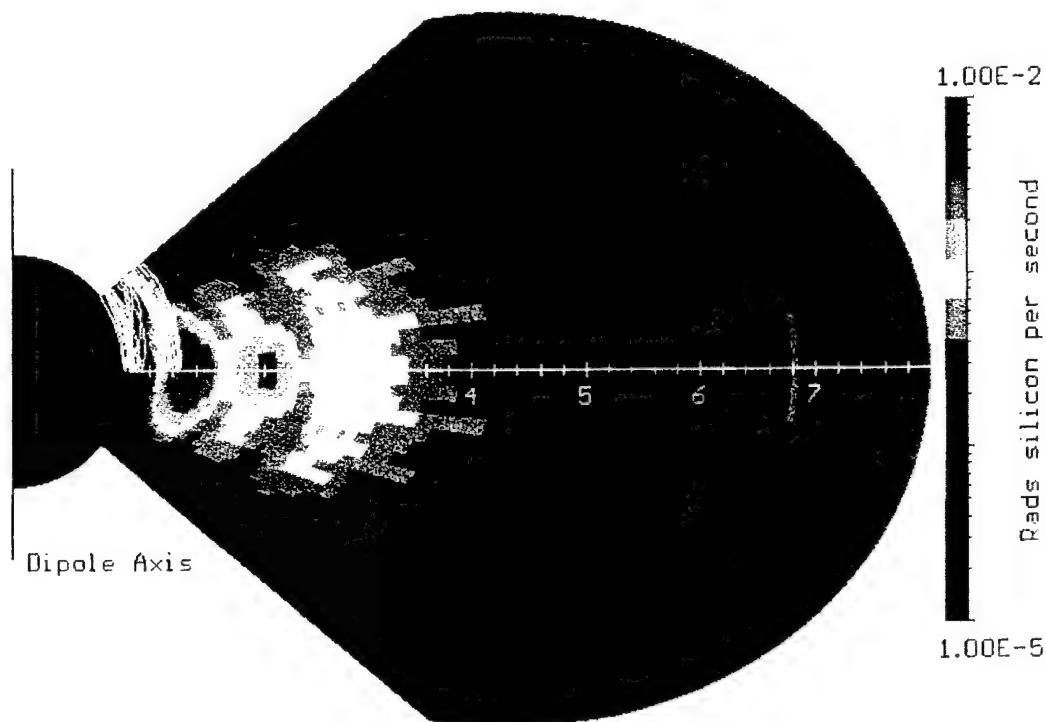


Figure 8-1. APEX orbits superimposed on results from CRRES dosimeter combined HILET and LOLET dome 2 (232.5 mils Al) binned from CRRES orbits 4 to 1067 (27 July 1990 to 12 October 1991).

Figure 8-2 shows a comparison of the inner proton belt between APEX, CRRES, and DMSP. The data sets for the three satellites were binned and averaged. The most restricted data set is that of DMSP since it flies at a near-constant altitude. It provides just a thin shell on the inner edge of the radiation belt. However, the number of data points over the restricted altitude is very large, so the statistics in this confined region are very good. The CRRES data set has the greatest coverage in B/B_0 and L space but it passes through perigee so quickly that the total amount of time spent at low altitudes is too small to give good statistics. The scatter on the inner edge of the CRRES model in Figure 8-2 attests to this. Finally, the APEX data provides both good coverage and good statistics.

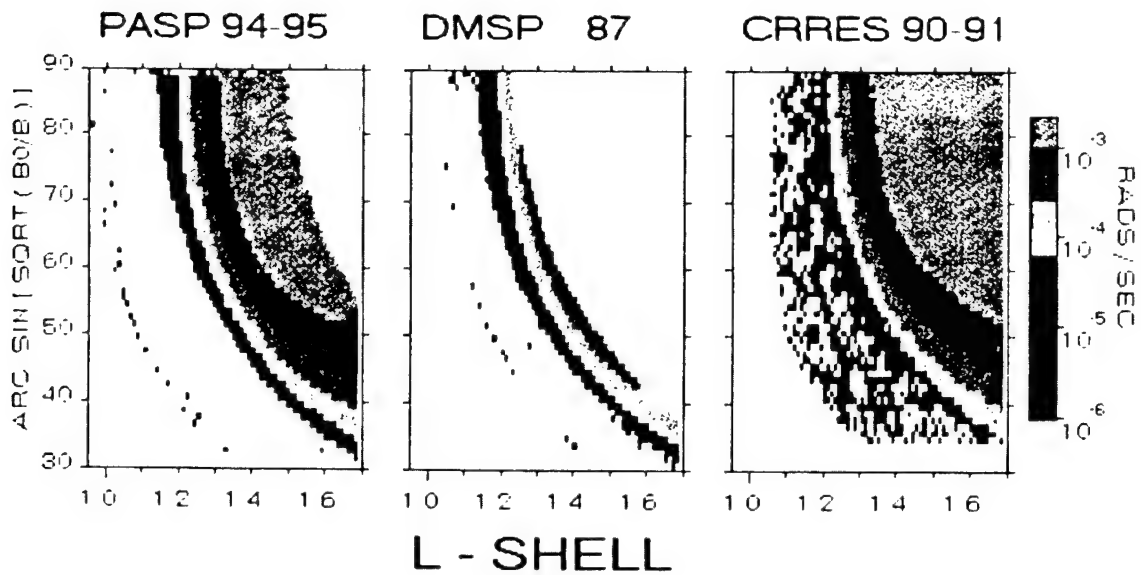


Figure 8-2. HILET delta dose (protons > 35 MeV).

Figure 8-3 shows the LOLET measured dose for all four channels from 3 August 94 to 10 September 95. The total LOLET dose for the period for channels L1, L2, L3, and L4 was 2 Mrad(Si), 7.2 krad(Si), 2.5 krad(Si), and 1.9 krad(Si) respectively. Figure 8-4 shows the HILET measured dose for all four channels over the same time period. The HILET dose for channels H1, H2, H3, and H4 was 48 krad(Si), 13 krad(Si), 6.5 krad(Si), and 4 krad(Si) respectively.

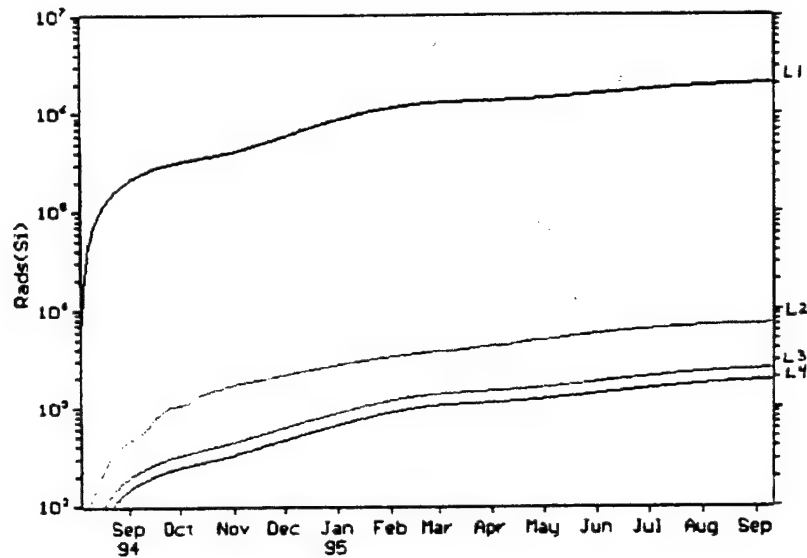


Figure 8-3. LOLET total dose.

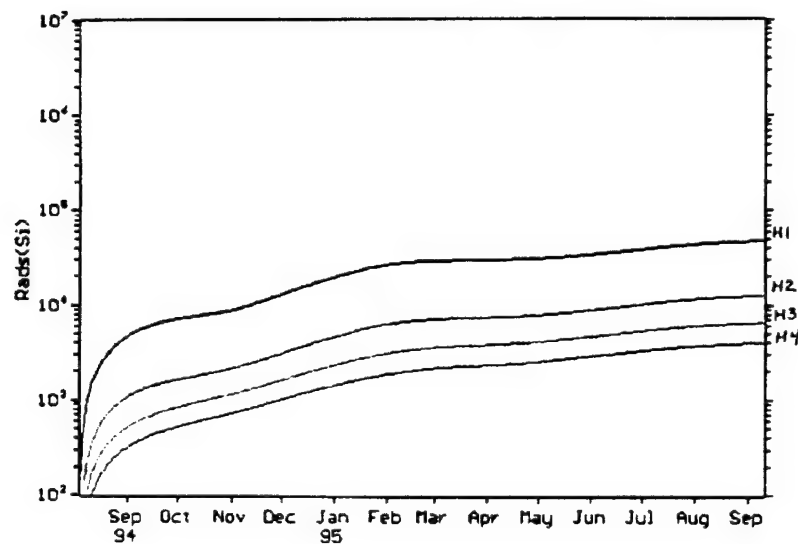


Figure 8-4. HILET total dose.

The data from the APEX space dosimeter was compared with the CRRESRAD model for channels 2, 3, and 4 for the entire mission. Figure 8-5 shows the predictive HILET dose per day (green) in rad(Si) per day over the entire mission and the measured HILET dose per day (black) by the APEX dosimeter for channels 2B, 3, and 4. The correlation is quite good for all three channels. Figure 8-6 is a similar plot on a much smaller time scale (October 1994). The correlation between predictive and measured is clearly evident. Finally, Figure 8-7 shows the predictive LOLET dose per day (green) in rad(Si) per day over the entire mission and the

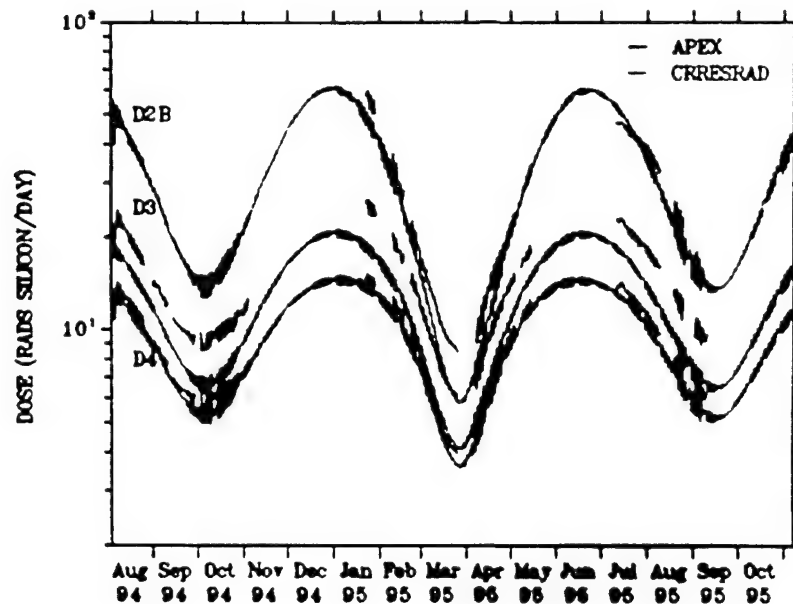


Figure 8-5. HILET dose per day.

measured LOLET dose per day (black) by the APEX dosimeter for channels 2B, 3, and 4. The correlation between predicted and measured for channels 3 and 4 is quite good. However, the correlation for predictive and measured for channel 2 is not close because the CRRESRAD model does not include outer zone electrons at low altitudes.

Earlier work (Ref. 8-3) has shown that VHLET counts (which can only be produced from protons by nuclear interactions in this dosimeter) can be directly related to SEUs. SEU data taken from the on-board solid state data recorder (SSDR), which contained 220 4Mbit X 1 Hitachi DRAMs, was compared to insitu particle measurements made by the dosimeter. Figure 8-8 shows the SEU data in color scale in SEUs per minute for three altitudes (800 to 900 km, 1500 to 1600 km, and 2300-2400 km). The data were binned in 2° latitude and 3° longitude. Going from near the heart of the inner belt down to lower altitudes, the effect of the offset dipole reducing the area of the inner belt encountered by the satellite can readily be seen. At lowest altitudes shown, the inner belt projection is confined to a very small region and the relative number of SEUs (color scale) is down significantly from the highest altitude. This small confined region is called the South Atlantic Anomaly (SAA) at low altitudes. [The greatest number of particles confined to (trapped on) any magnetic flux tube is on the magnetic equator, and the further off the equator, the fewer the particles.] The SAA is the only region where the inner belt projects down to the lowest

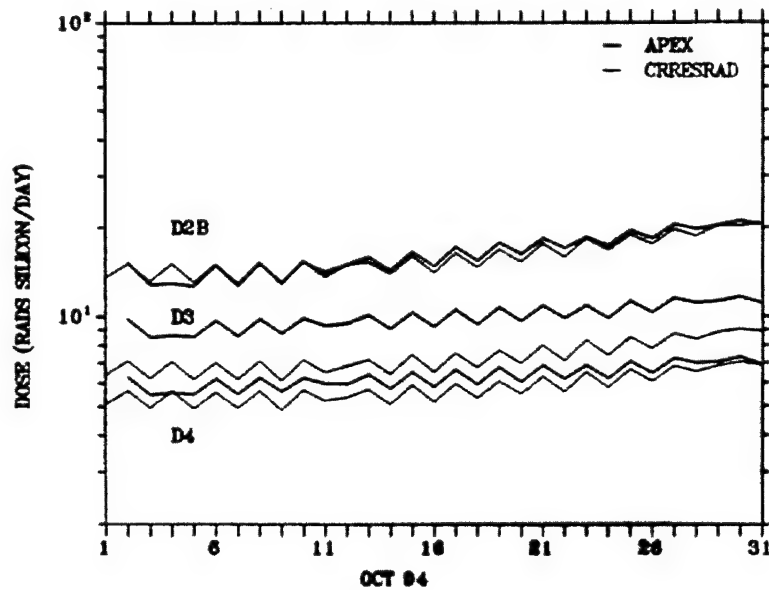


Figure 8-6. HILET dose per day (expanded scale).

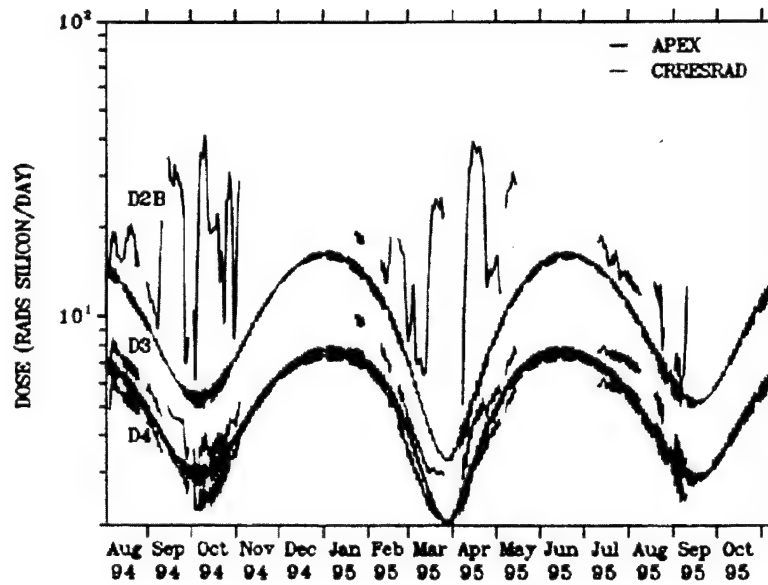


Figure 8-7. LOLET dose per day.

altitudes due to the offset dipole, and thus is the most hazardous radiation region for producing SEUs for low altitude spacecraft. However, satellites in elliptical orbits such as APEX, see much harsher radiation environments as they traverse the heart of the inner belt at the magnetic equator.

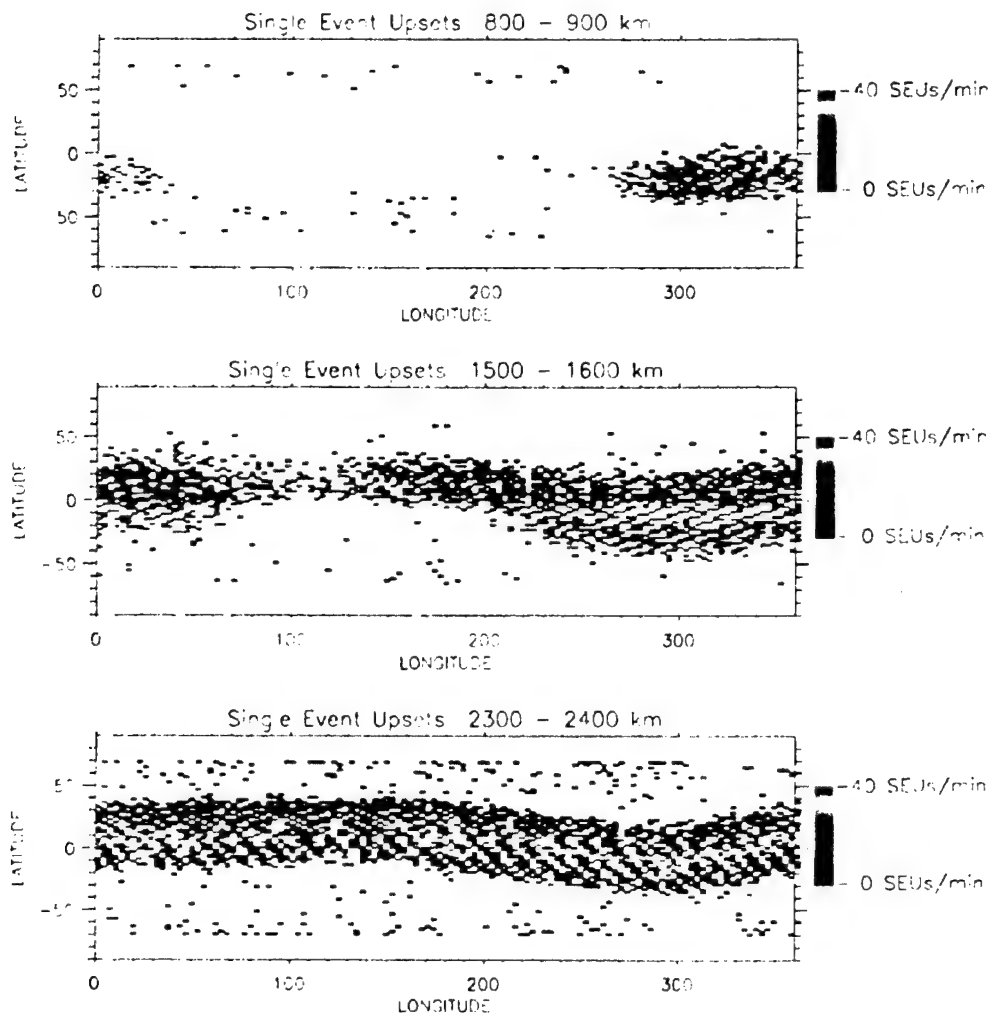


Figure 8-8. Single event upsets.

The SEUs were binned in $0.01 R_E$ and plotted as a function of L in Figure 8-9. The peak is between L -values of 1.35 and $1.40 R_E$. This is consistent with the 2300 and 2400 km data shown in Figure 8-8, which was the highest altitude SEU data available at the magnetic equator (2300 to 2400 km equals L -values of approximately 1.36 to $1.38 R_E$ on the magnetic equator.) Plots like Figure 8-9 were made for all the VHLET and HILET B channels. They all had a similar shape, but it was obvious the VHLET curves were more nearly identical to the SEU curve than the HILET B curves. SEU versus VHLET and HILET B count plots were made, and correlation coefficients were calculated for each of the 8 values against SEUs. Table 8-2 gives the resulting coefficients, and Figure 8-10 shows the best fit, VHLET for detector 1B, plotted versus SEU. These results clearly show that SEUs are clearly best related to the lowest energy particles that can create nuclear interactions in the device, approximately 40 to 50 MeV.

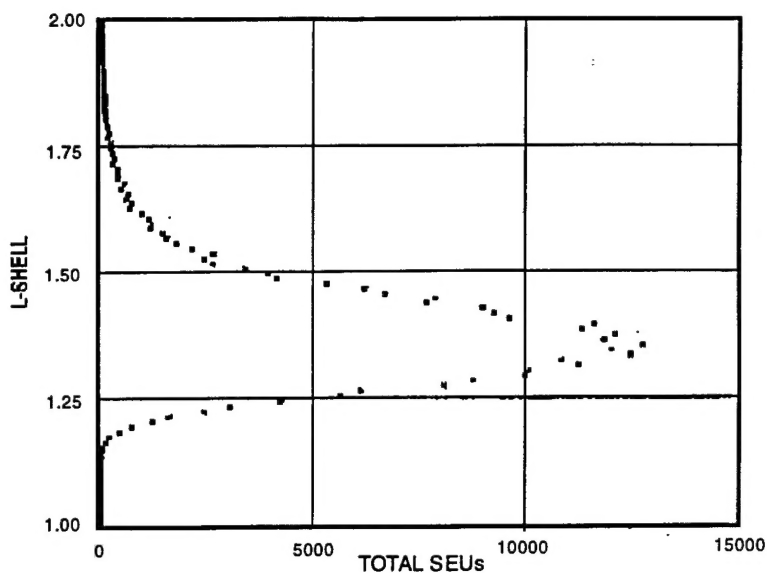


Figure 8-9. APEX SEU data.

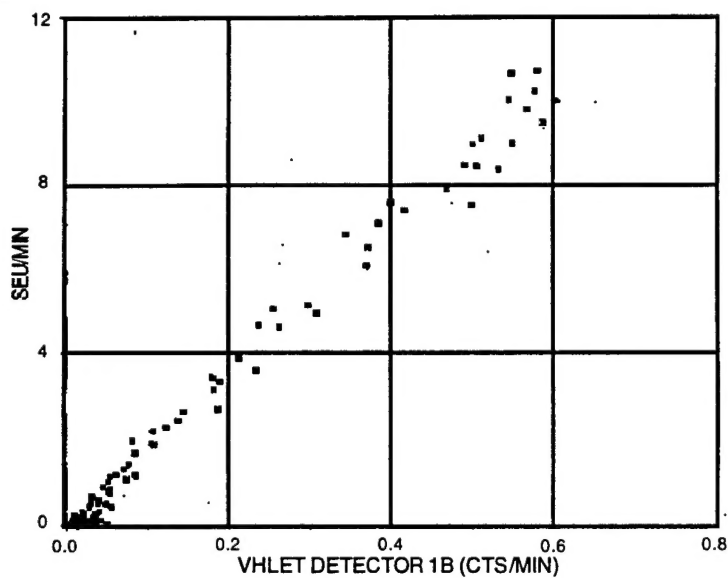


Figure 8-10. APEX SEU—dosimeter correlation.

The APEX space radiation dosimeter collected data up until 2 June 96 when the satellite failed. Two papers based on the data collected have been published in the IEEE Transactions on Nuclear Science. The first describes in more detail the measurements taken at the low altitude edge of the inner radiation belt by Gussenhoven (Ref. 8-5). The second by Mullen (Ref. 8-6) presents more SEU data from the APEX solid state tape recorder and correlates the data to VHLET measurements made by the dosimeter.

**Table 8-2. Correlation Coefficients
(Dosimeter Counts versus SEUs)**

| Detector Number | LET | Coefficient |
|-----------------|---------|-------------|
| 1B | HILET B | 0.551 |
| 2B | HILET B | 0.811 |
| 3 | HILET B | 0.940 |
| 4 | HILET B | 0.979 |
| 1B | VHLET | 0.995 |
| 2B | VHLET | 0.989 |
| 3 | VHLET | 0.987 |
| 4 | VHLET | 0.963 |

References for Chapter 8

- 8-1. Gussenhoven, M.S., *et al.*, "New Low Altitude Dose Measurements," *IEEE Transactions on Nuclear Science*, NS-34, pp. 676-683, 1987.
- 8-2. Mullen, E.G. and Gussenhoven, M.S., "Results of Space Experiments: CRRES," in *The Behavior of Systems in the Space Environment*, Dewitt, R.N., Dustor, D., Hyder, A.K., eds., Kluwer Academic, Dordrecht, pp. 605-653, 1993.
- 8-3. Mullen, E.G. and Ray, K.P., "Microelectronics Effects as Seen on CRRES," *Advances in Space Research*, 14, 10, pp. 797-807, October 1994.
- 8-4. Kerns, K.J. and Gussenhoven, M.S., *CRRESRAD Documentation*, PL-TR-92-2201, Phillips Laboratory, AFMC, Hanscom AFB, MA 01731, 1992.
- 8-5. Gussenhoven, M.S., *et al.*, "Low Altitude Edge of the Inner Radiation Belt: Dose Models from the APEX Satellite," *IEEE Transactions on Nuclear Science*, NS-42, pp. 2035-2042, 1995.
- 8-6. Mullen, E.G., *et al.*, "SEU Results from the Advanced Photovoltaic and Electronics Experiments (APEX) Satellite," *IEEE Transactions on Nuclear Science*, NS-42, pp. 1988-1994, 1995.

DISTRIBUTION LIST

| | |
|---|----------------|
| AUL/LSE Bldg 1405 - 600 Chennault Circle Maxwell AFB, AL 36112-6424 | 1 cy |
| DTIC/OCP 8725 John J. Kingman Rd, Suite 0944 Ft Belvoir, VA 22060-6218 | 2 cys |
| AFSAA/SAI 1580 Air Force Pentagon Washington, DC 20330-1580 | 1 cy |
| PL/SUL Kirtland AFB, NM 87117-5776 | 2 cys |
| PL/HO Kirtland AFB, NM 87117-5776 | 1 cy |
| Official Record Copy PL/VTV/Ralph James Kirtland AFB, NM 87117-5776 | 100 cys |
| PL/VT Dr. Barry Hogge Kirtland AFB, NM 87117-5776 | 1 cy |

